The Influence of Water on the Fracture Envelope of an Adhesive Joint

Pedro Nuno Martins Fernandes

A dissertation submitted for Master's Degree in Mechanical Engineering

Supervisor: Prof. Lucas F.M. da Silva

Co-supervisor: Mr. Guilherme Viana

U.PORTO

FEUP FACULDADE DE ENGENHARIA
UNIVERSIDADE DO PORTO

Integrated Masters in Mechanical Engineering

July 2016

To my family

Resumo

As ligações adesivas têm sido crescentemente aplicadas na indústria aeroespacial, automóvel e naval. Quando comparadas com ligações mecânicas, como rebites, as ligações adesivas apresentam um menor peso e um menor custo. Todavia, na indústria dos transportes, este tipo de ligação pode estar exposta a ambientes agressivos, tal como ambientes com elevada humidade, que comprometem o seu desempenho. Ensaios de mecânica da fratura para juntas adesivas permitem determinar propriedades mecânicas relevantes, quer para a caracterização da resistência do adesivo, quer para o processo de projeto de juntas.

Esta pesquisa tem como objetivo determinar o envelope de fratura de um adesivo em função do teor em água presente no próprio adesivo. A caracterização à fratura das juntas adesivas foi realizada quando estas estavam submetidas a cargas de modo puro (corte e abertura) e misto. A resistência à fratura em modo puro I e II foi determinada através de ensaios *Double Cantilever Beam* (DCB) e *End-Notched Flexure* (ENF), respetivamente. A caracterização da tenacidade à fratura da junta adesiva solicitada em modo misto foi realizada com auxílio de um dispositivo que permite criar solicitações que vão desde o modo puro I até perto do modo puro II. O adesivo caracterizado foi um epóxido para a indústria automóvel, SikaPower®-4720.

A influência da água no comportamento da junta adesiva foi estudada através da variação de valores da tenacidade à fratura. Dado que o processo de difusão numa junta DCB é demorado, e para conseguir obter uma concentração uniforme de água em todo o adesivo da junta, foi adotada uma modificação no provete DCB que permite acelerar a difusão. Este processo requer a produção de uma placa adesiva que possa ser degradada e ligada adesivamente aos substratos do provete DCB. Esta metodologia foi utilizada em conjunto com o provete DCB normalizado.

Foram realizados dois tipos de análises com elementos finitos. A primeira, análise de difusão, pretende determinar a variação de concentração de água no provete DCB normalizado. A segunda, análise dos ensaios de mecânica da fratura, tem dois objetivos: validar quer os resultados obtidos quer a utilização dos provetes modificados.

Constatou-se que o envelhecimento do adesivo em água salgada provoca um aumento das propriedades mecânicas, causado pela plastificação do adesivo. Já o envelhecimento em água destilada provoca a degradação do adesivo, com consequente redução das propriedades mecânicas.

Abstract

The use of adhesive joints has been increasing in the aerospace, automotive and maritime industries. When compared to mechanical joints, such as rivets, adhesive joints present a reduction in weight and cost. However, in the transport industry, this type of joint may be exposed to aggressive environments, such as high humidity, which compromise its performance. Fracture mechanics tests for adhesive joints provide relevant mechanical properties for both characterization of the adhesive's toughness and for the design of the joint.

This research aims to determine the fracture envelope of an adhesive joint as a function of the water content in the adhesive. The fracture characterization of the adhesive joints was performed when the specimens were submitted to pure modes (shear and opening) and mixed-mode loadings. The fracture toughness under mode I and II were determined using Double Cantilever Beam (DCB) and End-Notched Flexure (ENF) tests, respectively. The characterization of the fracture toughness under mixed-mode was done using an apparatus capable of applying a wide range of loadings that go from pure mode I to almost pure mode II. The adhesive used was an epoxy for the automotive industry, SikaPower®-4720.

The influence of water in the adhesive joint was verified by the changes of the fracture mechanics properties. Given that the diffusion process in a DCB joint takes a long period of time, and to obtain a uniform water concentration in the adhesive joint, a modified DCB specimen capable of accelerating the diffusion process was adopted. This modification requires the production of an adhesive plate that can be degraded in an aging environment and then bonded to the adherends on the DCB specimen. This approach was used in conjunction with the standard DCB specimen.

Two types of finite element analysis were done. The first, a diffusion analysis, intended to determine the gradient of water concentration in the standard DCB specimen. The second, a fracture mechanics analysis, had two objectives: validating the results from the standard DCB specimens and determining the influence of the adhesive plate, used to accelerate the aging process, on the mechanical properties obtain through the experimental tests.

The ageing in salt water caused an increase of mechanical properties due to the plasticization of the adhesive. The ageing in distilled water caused degradation of the adhesive, with consequent decrease of its mechanical properties

Acknowledgements

I would like to thank Prof. Lucas da Silva, for the opportunity to collaborate in this project under his supervision and for guiding me during its development.

To my co-supervisor, Mr. Guilherme Viana, for all the patience and time spent helping and guiding me.

A special thanks to Dr. Ricardo Carbas, for all the help given in the experimental part of this thesis and for the suggestions made, which lead to the successful application of the modified specimens used in this dissertation.

To FEUP's adhesive group (ADFEUP), for the help and advice while developing this thesis. A special mention to my master's degree colleagues for their friendship.

Finally, to my family, especially to my parents, who supported me during all these years.

Contents

List of figures

List of tables

List of acronyms and symbols

Acronyms

4ENF	Four-Point End Notched Flexure
ADCB	Asymmetric Double Cantilever Beam
CBBM	Compliance-Based Beam Method
CZM	Cohesive Zone Model
DCB	Double Cantilever Beam
ELS	End Loaded Split
ENF	End Notched Flexure
FEA	Finite Element Analysis
FPZ	Fracture Process Zone
MMB	Mixed Mode Bending
ODCB	Open Double Cantilever Beam
R-Curve	Resistance Curve

Symbols

a	Crack length
a_0	Initial crack growth
a_{eq}	Equivalent crack length
B	Width of the adherend
C	Compliance
C_0	Initial specimen compliance
F_1	Load applied to cantilever 1
F_2	Load applied to cantilever 2
E_f	Corrected flexural modulus
G_I	Mode I contribution of strain energy release rate
G_{II}	Mode II contribution of strain energy release rate

1 Introduction

1.1 Background and motivation

The use of adhesive joints has been increasing in the aerospace, automotive and maritime industries. When compared to mechanical joints, adhesive joints present a reduction in weight and cost, which translates in a reduction of production costs and fuel consumption for the transportation industries. However, for the joint design process to be optimized, the mechanical properties must be well known. While this is true for static conditions, the lack of design tools in terms of durability are a concern that is limiting the use of adhesive in the automotive industry [1].

This type of joint may be exposed to aggressive environments, such as high humidity, extreme temperature or radiation. While fracture mechanics characterization tests for adhesive joints may provide relevant properties to guide the design process, the information available to predict the adhesive's behaviour after being exposed to the environment is scarce. Therefore, the influence of environmental agents on the mechanical properties of the adhesive should be studied [1].

1.2 Objectives

The objective of this thesis was to determine the fracture envelope of an adhesive joint and the influence of water on its behaviour. In order to do so, the fracture envelope of the adhesive was determined for three different environments and then a correlation between the mass of water absorbed by the adhesive and its fracture toughness is established.

1.3 Research methodology

In order to complete the objective of this thesis, the following research methodology was adopted:

1. An overview of the most used tests to characterize an adhesive's fracture toughness.
2. Study of the influence of water on the mechanical properties of the adhesive.
3. Characterization of the fracture envelope under humid (75% and 100% relative humidity - RH) and dry conditions (0% RH) using DCB and ENF tests, for pure mode I and II respectively, as well as an apparatus to simulate the mixed-mode I+II loadings.
4. Numerical simulation to predict the water concentration in the adhesive layer and to validate the data obtained from the fracture tests.
5. Data analysis and determination of the fracture envelope as a function of the water uptake.

1.4 Thesis outline

The structure of the thesis is divided in the following sections:

Chapter 1: Introduction to the thesis, its objectives and the research methodology adopted.

Chapter 2: Literature review on adhesive joints and their applications is done, followed by the most common fracture tests used to analyse the fracture toughness for each mode. Finally a study on the principles of water uptake and its influence in the mechanical properties of an adhesive joint.

Chapter 3: The specimen's and adhesives' properties are presented. Then, the specimen's manufacture process, for both standard DCB and modified DCB specimens, is described. The testing specifications and details for each loading mode are mentioned.

Chapter 4: Description of the finite element models created to simulate the water diffusion process, on both standard and modified DCB specimens, as well as the mechanic fracture tests, DCB, ENF and mixed-mode.

Chapter 5: Analysis and discussion of the results obtained numerically and experimentally.

Chapter 6: Summary of the conclusions obtained from the work developed in this research.

Chapter 7: Suggestions made to complement the work developed and to initiate new investigations.

2 Literature review

By definition, a structural adhesive is an adhesive capable of sustaining substantial loads and responsible for the strength and stiffness of a structure. The objective of the structural adhesive is to bond two different surfaces. The materials to be bonded are called substrates or, more generally, adherends [2].

As an alternative to mechanical joints, the usage of adhesive joints has been increasing since they provide several advantages over the conventional methods. An adhesive joint allows an uniform stress distribution along the bonded area, enhancing the stiffness, load transmission and fatigue resistance of the structure while reducing the weight and thus the cost [2, 3]. Adhesives can bond dissimilar materials and may also provide good damping properties due to their polymeric nature [2].

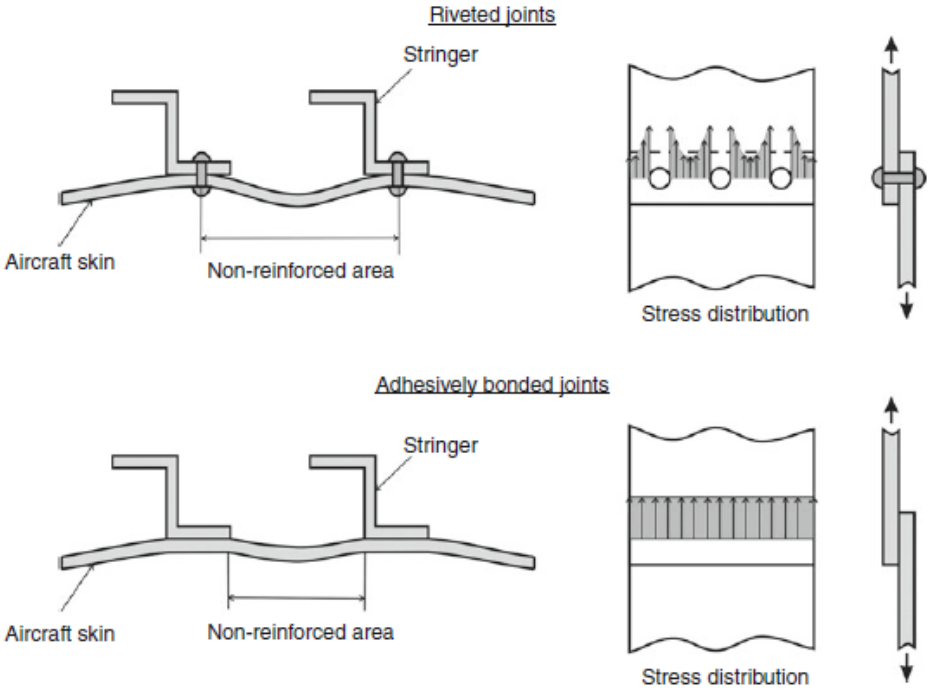

Figure 1: Improvement of the stiffness and stress distribution of adhesively bonded joints in relation to riveted joints [2].

Despite the vast number of advantages, adhesive bonding is also associated with some disadvantages. During the project of a structure, it is necessary to reduce the peeling and cleavage stress, as they concentrate the load in a small area and consider the adhesives' limited resistance to extreme temperatures, humidity and solar radiation. Furthermore, bonding is usually not instantaneous, the hardening process may require temperature and, to have a durable joint, a careful surface preparation is required [2, 3].

2.1 Transportation industry

Most of the transportation industries, which includes the aerospace, automotive, railway and marine industry, have been developing around three basic common concepts: safety, high speed and mass transportation. To achieve these objectives, composite materials have been increasingly used to create lightweight structures of aluminium, sandwich panels and carbon fibre reinforced plastics. Adhesive bonding is a method that allows these industries the possibility of joining dissimilar materials, reducing the weight of the structure without

compromising its safety and, as a consequence, decreasing the energy consumption of the vehicle [2, 3].

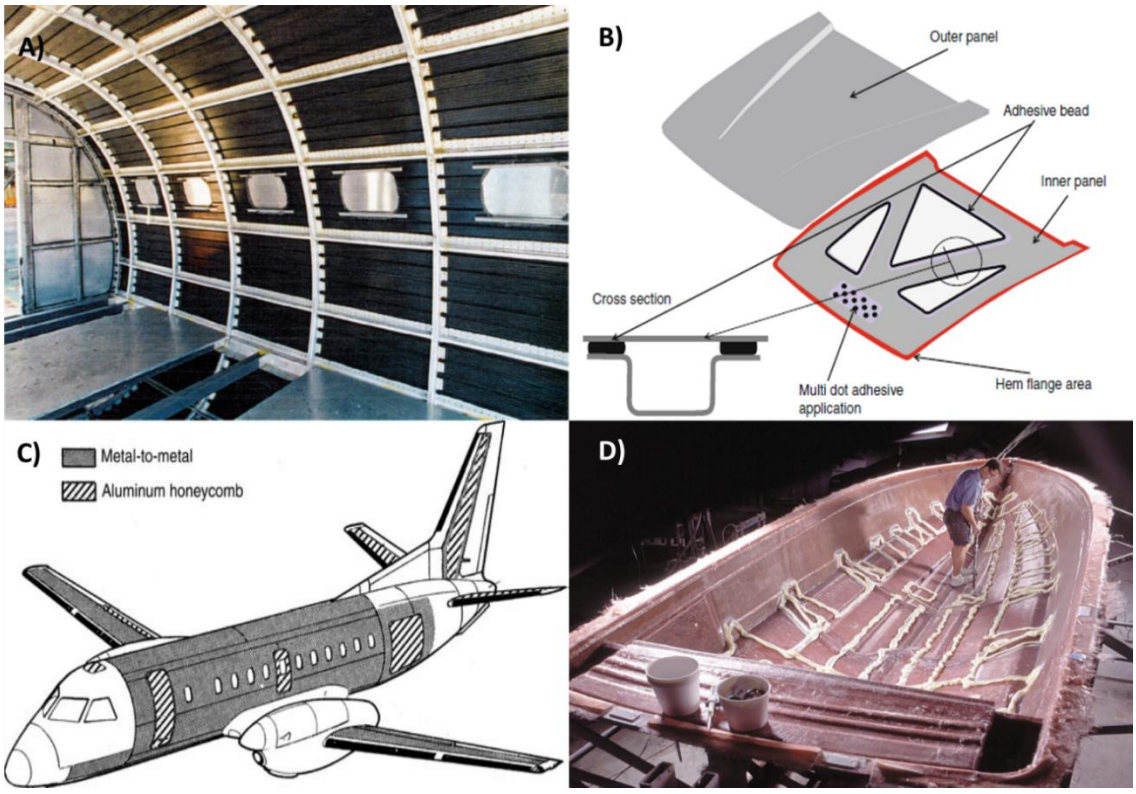

Figure 2: Application of adhesive bonding on the railway, automotive, aeronautic and maritime industries.

A) Railway industry: Prototype carbon fiber reinforced plastic body structure for high-speed trains using pultruded panels [2].
B) Automotive industry: Anti-flutter bonding applied on the front hood of a car [2].
C) Aeronautic industry: Application of adhesive bonding to SAAB 340 fuselage, wings and tail [2].
D) Maritime industry: Application of adhesive before bonding an internal motor boat structure (photo Plexus) [2]

2.2 Failure modes

There are three types of adhesive bond failure: cohesive failure, adhesive failure and mixed-mode failure.

- The cohesive failure occurs when the crack propagates in the adhesive, leaving traces of adhesion on both surfaces [4]. This means that both the adherend and the interface adherend-adhesive have a higher strength than the adhesive [3]. If any other type of failure is identified upon rupture, the bond is weaker than the original construction.

- The adhesion failure occurs at the interface between the adherend and the adhesive, creating a smooth surface on the adhesive [4]. Such scenario is caused by the lack of a proper surface treatment, as it can be proved that an adhesion failure can be avoided with a surface treatment adequate to the substrate's material [3].

- Mixed-mode failure is a combination of both previous types [3] and a transitional phase between cohesive and adhesive failure [4]. Upon rupture, the failure area exhibits a combination of smooth and rough zones [4]. Mixed-mode failure occurs when the interface is partially degraded, making the bond less resistant to the environment and promoting the further degradation of the interface [4].

Exposure to environmental effects also has an influence on the failure mode. For instance, an aluminium substrate exposed to oxygen will create an oxide surface. When water contacts the oxide, hydration occurs. Such degradation can cause a transition from a cohesive failure to an unpredictable and weaker mixed failure, where both cohesive failure on the adhesive and adhesive failure on the oxide layer can be identified [5]. As a consequence, the bond's durability depends directly upon its resistance to degradation in the service environment [4]. Often, the degradation caused by mechanical loading, humidity and temperature combined is greater than the degradation caused by each one of them individually [3].

The influence of environmental effects on adhesive joints are usually studied using accelerated processes. Based on the data collected, it is possible to extrapolate some results. However, the extrapolation needs to be done with caution to avoid reliability issues. Furthermore, this method does not provide information for the real service conditions [3]. A hygro-thermo-mechanical finite element analysis can be used to predict the influence of the environmental ageing on the adhesive's properties. This is a sequentially-coupled analysis carried in three stages. First, it is determined the distribution of moisture and temperature within the joint. Then, an evaluation of the environmental effects and mechanical loadings combined is done. Lastly, a failure criterion is applied to the model [1]. Another alternative is to use a fully-coupled analysis. In this analysis the effects of moisture, temperature and load are simulated simultaneously, with the moisture concentration affecting the stress distribution and the stress state affecting the moisture diffusion analyses at the same time [6].

2.3 Strength prediction approaches

The failure of adhesive joints can be characterized by three basic approaches: continuum mechanics, fracture mechanics and damage mechanics.

2.3.1 Continuum mechanics

The continuum mechanics theory assumes the existence of a perfect joining between the adhesive and the adherend, ignoring interface properties. This approach characterizes the stresses and deformations in the bonded parts and defines a maximal force that the joint may sustain under the four common loading scenarios: shear, stress, peeling and cleavage (Figure 3) [3, 7].

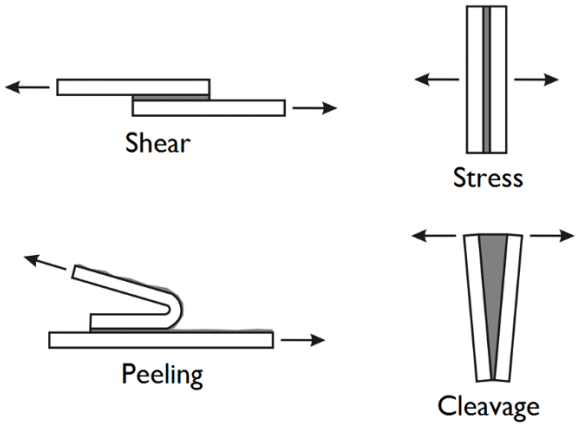

Figure 3: Most common loading scenarios (adapted from [3]).

There are, however, singularity points where stress will achieve an infinite value, making it difficult to apply these criteria as the stress on these points is mesh dependent (Figure 4) [3, 7, 8]. As an alternative, the adhesive and/or substrate can be rounded to avoid singularities [3].

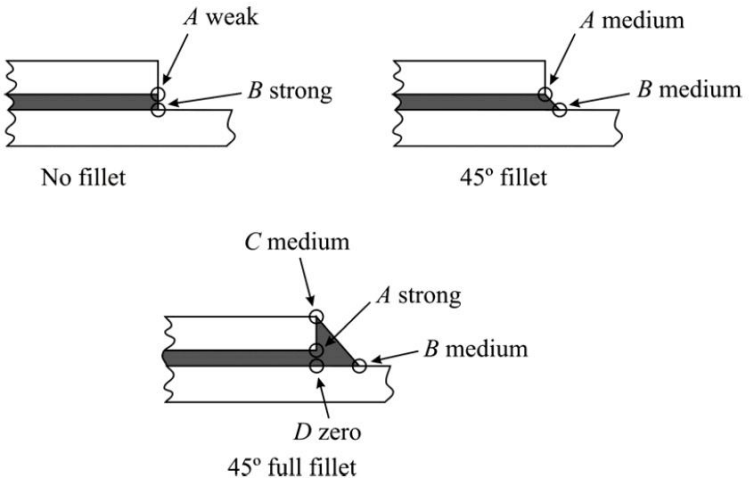

Figure 4: Singularity points on single lap joints and their strength [8].

2.3.2 Fracture mechanics

Fracture mechanics assumes a non-continuous structure, allowing the existence of defects or damages caused during its life at work. Imperfections such as delamination, debonding or cracks are possible points of stress concentration, promoting fracture initiation and propagation, leading to an eventual failure of the structure. This approach can determine if the dimensions of any defect remain under the critical fracture size which leads to structural failure [3, 7].

Fracture can occur due to three loading modes: mode I, opening mode, and modes II and III, shearing modes (Figure 5) [3].

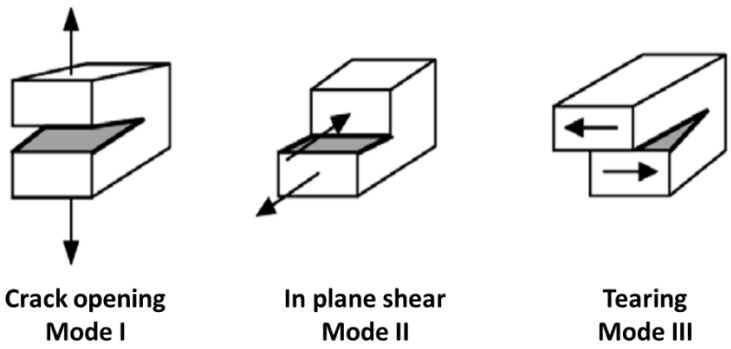

Figure 5:Adhesive joint fracture modes [9].

To study materials with cracks, fracture mechanics uses two criterions: a stress intensity factor criterion (K) and an energetic criterion (G) [3].

The stress intensity factor, K, is a scale parameter that quantifies changes in the stress state near the crack tip, originated by the infinite stress in that area [3, 7]. Considering a mode I loading, the stress intensity factor can be described as:

$$K_I = Y\sigma_r\sqrt{\pi a} \quad (1)$$

Where K_I depends of: a non-dimensional function (Y) dependent on the geometry and load distribution, a uniform stress σ_r perpendicular to the crack length (a).

A crack will occur when the intensity factor is equal to the material's mode I toughness (K_{Ic}), which is the property that measures the ability to prevent a crack propagation in mode I. While K_I is lower than K_{Ic}, no propagation will occur [7].

The energetic criterion hypothesises that the crack will only propagate when the available energy at the tip of the defect (G – energy release rate) is equal or higher than the energy needed for the crack to propagate (G_c- critical energy release rate) for the applied loading [3]. Therefore, the critical condition to avoid the crack propagation is:

$$G \leq G_c \qquad (2)$$

However, the fracture mechanics criteria mentioned are best suited for damage propagation, not for the damage initiation, as the dimension of any existing defects are unknown [7].

2.3.3 Damage mechanics

Damage mechanics combines both continuum and fracture mechanics in order to overcome the limitations and explore the potentials of the previous methods. In this approach, both strength and energy parameters are considered to characterize the adhesive joint fracture. While the continuum mechanics tools are used to model the damage initiation, fracture mechanics tools are used to describe the crack propagation. Furthermore, the continuum damage models consider the thickness' effect in the adhesive joint, an important aspect given that the fracture process zone (FPZ) changes with the thickness (Figure 6) and leads to different behaviours in the adhesive joint fracture [7].

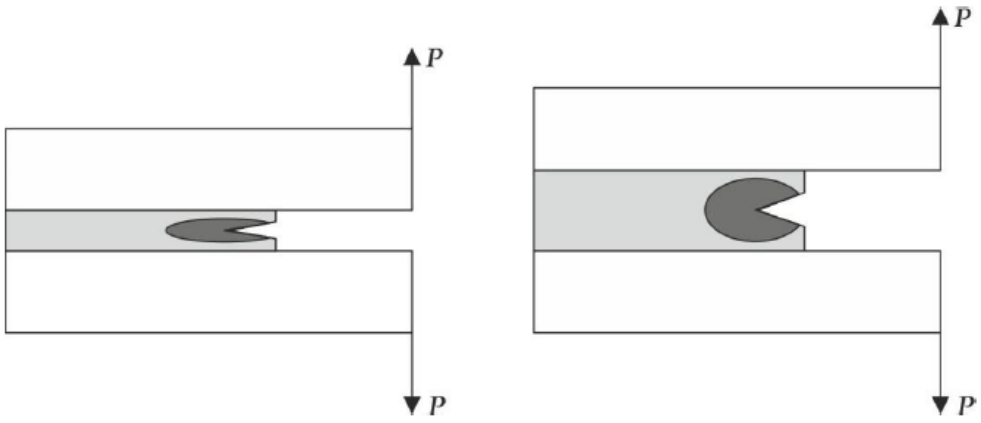

Figure 6:Influence of the adhesive's thickness on the fracture process zone (FPZ) [7].

The FPZ is a zone where inelastic processes occur and, as a consequence, any changes in this zone will influence the R-curve behaviour. The R-curves are graphical representations of Energy Release Rate variation (G) as a function of the crack length (a). The critical energy release rate (G_c) corresponds to a well-defined stabilization plateau of the R-curve [7].

To simulate an adhesive joint, two cohesive laws are used: trapezoidal cohesive law and triangular cohesive law (Figure 7) [3, 7]. The trapezoidal cohesive law is best suited for ductile adhesives [1, 7]. On the other hand, the triangular cohesive law, which is a particular case of the previous law, is more adequate for less ductile or brittle adhesives [1, 7].

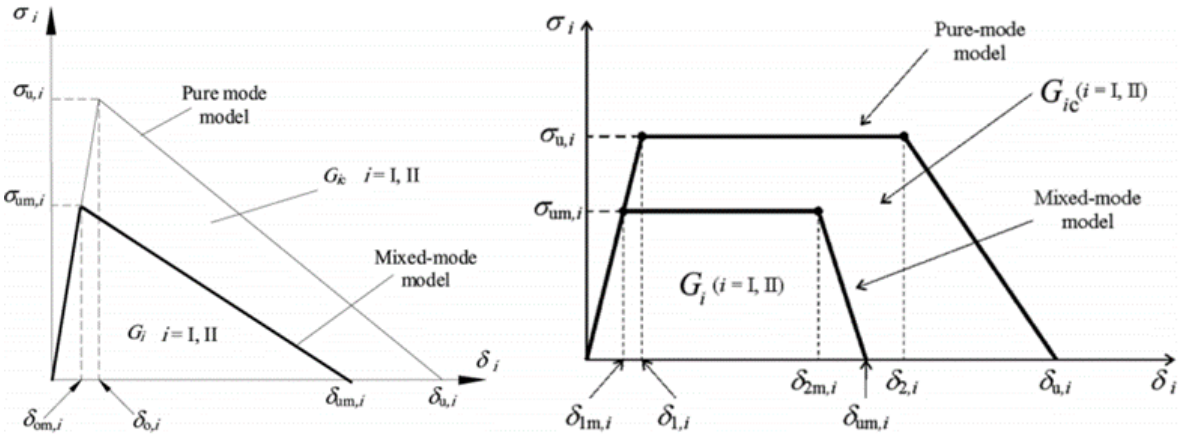

Figure 7: Trapezoidal and triangular softening law for pure and mixed-mode cohesive damage model (adapted from [7] and [10]).

2.4 Fracture mechanics tests

Fracture mechanics are accepted tools to characterize and help design the adhesive joint [7]. The energy dissipated during the crack growth (G_c), fracture toughness, is the most relevant property to analyse the different loading modes [11]. However, the fracture toughness varies with the type and combination of loading modes [9].

2.4.1 Mode I fracture tests

ASTM D 3433-99 and ISO 25217:2009 describe the two main tests to determine the energy release for mode I [3]:

- Double Cantilever Beam (DCB)
- Tapered Double Cantilever Beam (TDCB)

For the DCB test, the specimen is constituted by three parts: two beams, of constant thickness (h) and equal length (L), and the adhesive, of constant thickness (t). To simulate the pre crack (a_0 – pre crack length), an initial region is left without adhesive (Figure 8) [3, 7].

Figure 8: Representation of the DCB specimen in accordance to ASTM D3433-99 [7] (dimensions in mm).

During the test, the beams are open, usually with a speed between 0.5mm/min and 3mm/min, and the displacements (δ) are registered as a function of the crack length (a). Using Irwin-Keyes equation, it is possible to determine the fracture energy based on the load and displacement [3]:

$$G_c = \frac{P^2}{2b}\frac{dC}{da} \quad (3)$$

Where P is the load applied, b is the specimen's width and C is the adherend's compliance (δ/P). Applying this equation to the DCB specimen and considering the Compliance-Based Beam Method (CBBM), the fracture energy for mode I can be described as [3, 7]:

$$G_{Ic} = \frac{6P^2}{b^2h^3}\left(\frac{2a_e^2}{E_f} + \frac{h^2}{5G}\right) \quad (4)$$

The CBBM is a data processing technique based on the equivalent crack length's concept. This method does not require the measurement of the crack during the test. Instead, an equivalent crack length (a_e), which considers the length of the FPZ, is used [7, 12]. The equivalent crack length is determined by (Figure 9) [3, 7, 12]:

$$a_e = a + |\Delta| + \Delta a_{FPZ} \quad (5)$$

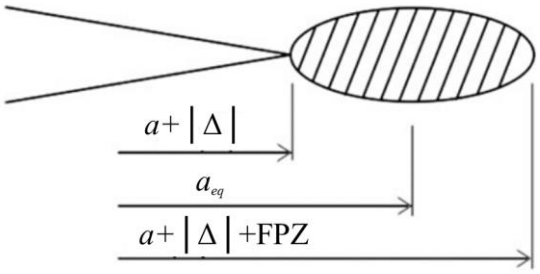

Figure 9: Definition of FPZ and equivalent crack length [12].

The value of a_e is given by:

$$a_e = \frac{1}{6\alpha}A - \frac{2\beta}{A} \quad (6)$$

Where:

$$\alpha = \frac{8}{Bh^3E}\ ;\ \beta = \frac{12}{5BhG};\ \gamma = -\frac{\delta_1}{P_1} \quad (7)$$

$$A = \left(\left(1\gamma + 12\sqrt{3\frac{(4\beta^3+27\gamma^2\alpha)}{\alpha} - 108}\right)\alpha^2\right)^{1/3} \quad (8)$$

The value of E_f, the equivalent flexural module, is given by [7]:

$$E_f = \left(C_0 - \frac{12(a_0 + |\Delta|)}{5BhG_{LR}}\right)^{-1}\frac{8(a_0 + |\Delta|)^3}{Bh^3} \quad (9)$$

Δ being the root rotation effect at the crack tip, defined by [7]:

$$\Delta = h\sqrt{\frac{E_f}{11G_{LR}}\left[3 - 2\left(\frac{\Gamma}{1+\Gamma}\right)^2\right]} \quad (10)$$

And [7]:

$$\Gamma = 1.18\frac{E}{G} \quad (11)$$

On the other hand, the TDCB test can be used to obtain the critical energy release rate regardless of the crack length but it is much more complex to manufacture (Figure 10) [3].

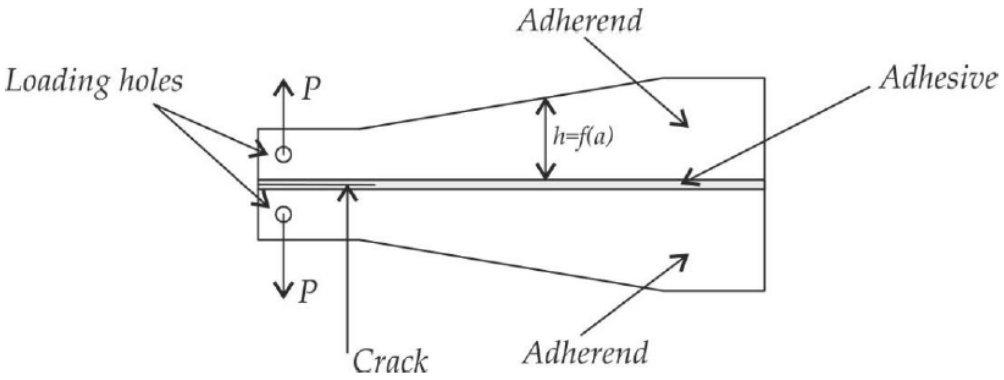

Figure 10: Representation of the TDCB specimen [7].

2.4.2 Mode II fracture tests

There are no standards for testing the mode II fracture toughness. The most used tests are (Figure 11) [7]:

- ELS (End Loaded Split)
- 4ENF (Four-point End Notched Flexure)
- ENF (End Notched Flexure)

The ELS test has the advantage of allowing the measurement of the mode II R-curve and promoting a stable crack initiation. However, it requires an elaborate data reduction scheme, which involves a clamp correction factor, and the specimen is susceptible to large displacements. All factors considered, it presents some difficulties to determine the correct value of the G_{IIc} [3, 7].

The 4ENF test is the most sophisticated but reveals some friction problems at the pre crack zone. These issues are caused by the loading systems [3, 7].

The most simple and most common test is the ENF. For this test, the specimens are made of two beams, with constant section and equal length ($2L$), bonded together along the length, with exception for the pre-crack length (a), and simply supported at both ends. A load is then applied at mid length of the beam to cause shear stress in the adhesive. Using the beam theory, Irwin-Keyes equation and ignoring the shear effect at the crack tip, G_{II} can be defined as [3, 7]:

$$G_{II} = \frac{9P^2a^2}{16b^2Eh^3} \quad (12)$$

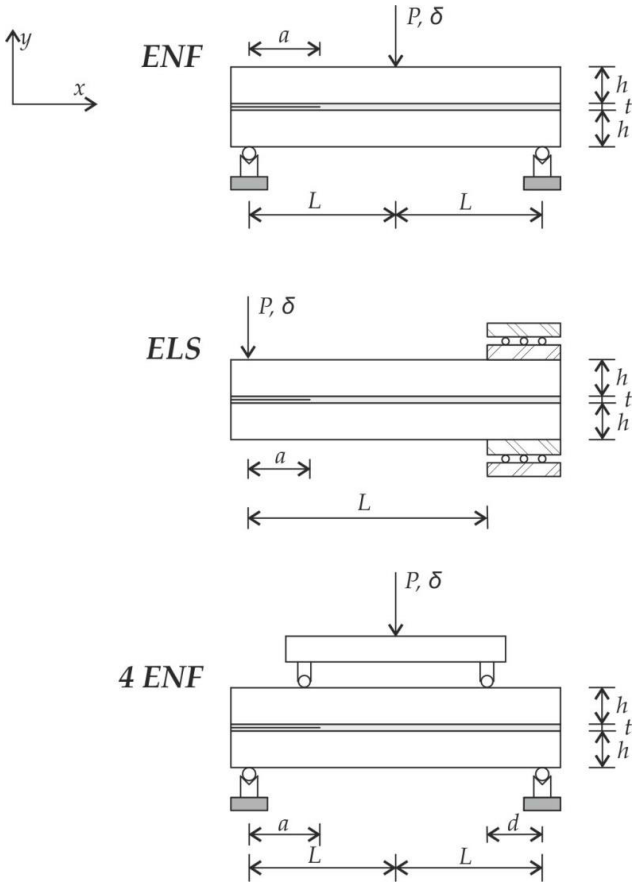

Figure 11: Representation of the ENF, ELS and 4ENF tests [7].

However, to consider the root rotation at the crack tip, the following equation should be used [7]:

$$G_{IIc} = \frac{9P^2(a + |\Delta_{II}|)^2}{16b^2Eh^3} \quad (13)$$

Where Δ_{II} is the crack length correction and is proportional to the crack length for mode I (Δ_I) from the DCB test [7]:

$$\Delta_{II} = 0.42\Delta_I \quad (14)$$

This method relies on the measurement of the crack length during the test. This can be quite difficult as the propagation occurs by shear stress with the adherends friction. Additionally, the FPZ at the crack tip is not considered, where damage occurs by inelastic processes, which absorbs part of the available energy [3, 7]. As a consequence, a correction needs to be considered to include the effect of the FPZ. The FPZ is included in the definition of compliance [3]:

$$C = \frac{3(a + \Delta a_{FPZ})^3 + 2L^3}{12E_f bh^3} + \frac{3L}{5Gbh} \quad (15)$$

Where the equivalent flexural modulus is:

$$E_f = \frac{3a_0^3 + 2L^3}{12bh^3}\left(C_0 - \frac{3L}{5Gbh}\right)^{-1} \quad (16)$$

2.4.3 Mixed-mode fracture tests

For the mixed-mode, there are several tests that describe this fracture [7] (Figure 12):

- Single Leg Bending (SLB)
- Asymmetric Tapered Double Cantilever Beam (ATDCB)
- Asymmetric Double Cantilever Beam (ADCB)
- Cracked Lap Shear (CLS)
- Mixed-Mode Bending (MMB)

For mixed-mode tests, the fracture ratio in planar problems can be defined as (Figure 12):

$$\Psi = \tan^{-1}\left(\frac{K_{II}}{K_I}\right) = \tan^{-1}\sqrt{\left(\frac{G_{II}}{G_I}\right)} \quad (17)$$

From these tests, only the MMB is standardized (defined in ASTM D6671) [3]. The MMB test is a combination of the DCB and ENF tests, used to determine the toughness in mode I and II respectively, as it involves the mid span load from the ENF test and the opening force of the DCB test [3]. The relative value of the two forces is responsible for the mode mixity degree at the crack tip. Alternatively, one single loading (P) can be applied through a loading beam and hinge, as shown on Figure 13. In this case, the mode ratio is defined by the loading distance (c) [3, 7].

Based on the beam theory, ignoring the transverse shear effect and considering the free body diagram for each mode, the following energy release rates can be obtained [3, 7]:

$$G_I = \frac{3a^2P^2}{4b^2Eh^3L^2}(3c - L)^2 \quad (18)$$

And [3]:

$$G_{II} = \frac{9a^2P^2}{16b^2Eh^3L^2}(c + L)^2 \quad (19)$$

The ratio for the MMB test is then [7]:

$$\frac{G_I}{G_{II}} = \frac{4}{3}\left(\frac{3c - L}{c + L}\right)^2 \qquad c \geq \frac{L}{3} \quad (20)$$

However, these two equations underestimate the values of G_I and G_{II}. To avoid this situation, the cantilever rotation at the crack tip caused by mode I and the shear effect of both modes should be considered. As a consequence, the following corrected equations are obtained [3, 7]:

$$G_I = \frac{3a^2P^2}{4b^2Eh^3L^2}(3c - L)^2\left(a^2 + \frac{2a}{\lambda} + \frac{1}{\lambda^2} + \frac{h^2E}{10G}\right) \quad (21)$$

And [3, 7]:

$$G_{II} = \frac{9a^2P^2(c + L)^2}{16b^2Eh^3L^2}\left(a^2 + \frac{0.2h^2E}{G}\right) \quad (22)$$

Test name	Test scheme	Global mixity φ (°)
Asymmetric Double Cantilever Beam (ADCB)		≈0 -34
Single Leg Bending (SLB)	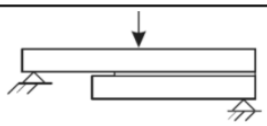	≈ 41
Crack Lap Shear (CLS)		≈49
Asymmetric Tapered Double Cantilever Beam (ATCB)		≈20
Mixed Mode Bending (MMB)	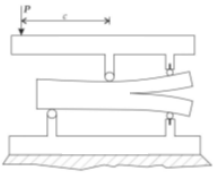	$\varphi=f(c)$
Spelt Loading Jig (SPELT)	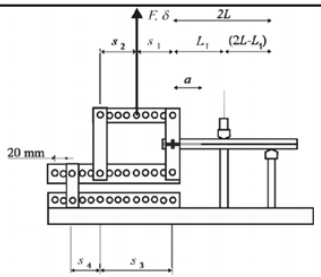	$\varphi=f(s_1, s_2, s_3, s_4)$

Figure 12:Mixed-mode tests and corresponding mode ratio Ψ [7] .

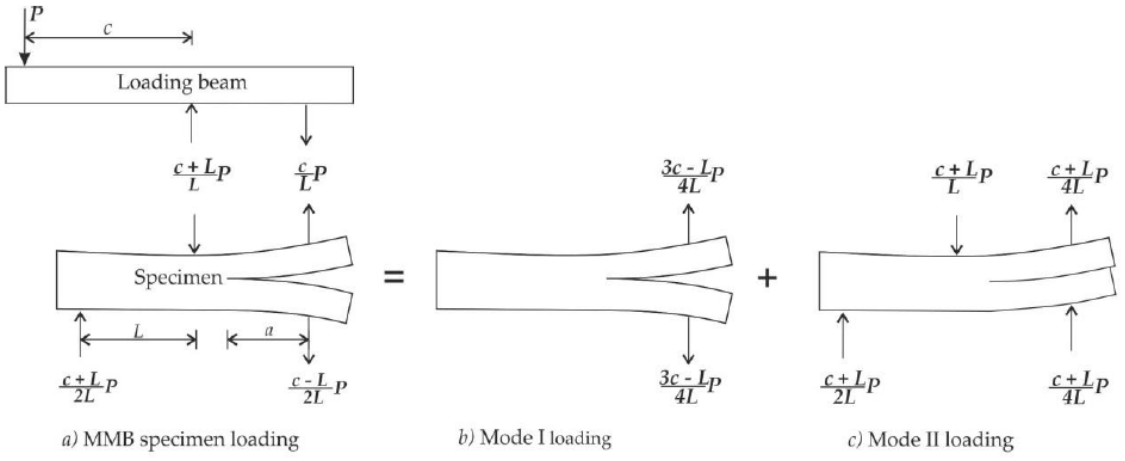

Figure 13: MMB free body diagram [7].

Where [3, 7]:

$$\lambda = \left(\frac{6E_2}{h^4 E}\right)^{1/4} \quad (23)$$

In this last equation, E_2 is the transversal Young's modulus (equal to E for isotropic materials) [3].

2.5 Fracture envelope

Fracture envelopes are graphics that depict the relation between the strain energy release rate for pure mode I and II (G_I and G_{II}, respectively), represented in each axis. On the first quadrant of this graphic, the mixed-mode fracture energy is plotted [7]. This graphic allows a more complete understanding of the adhesive bond's behaviour under a wide range of loading combinations.

The bonded joint's fracture under several mixed-mode I+II conditions has been characterized using the specimen's compliance, beam theory and crack equivalent concept [7, 10]. These cases can be analysed considering a linear or quadratic criteria (Figure 14).

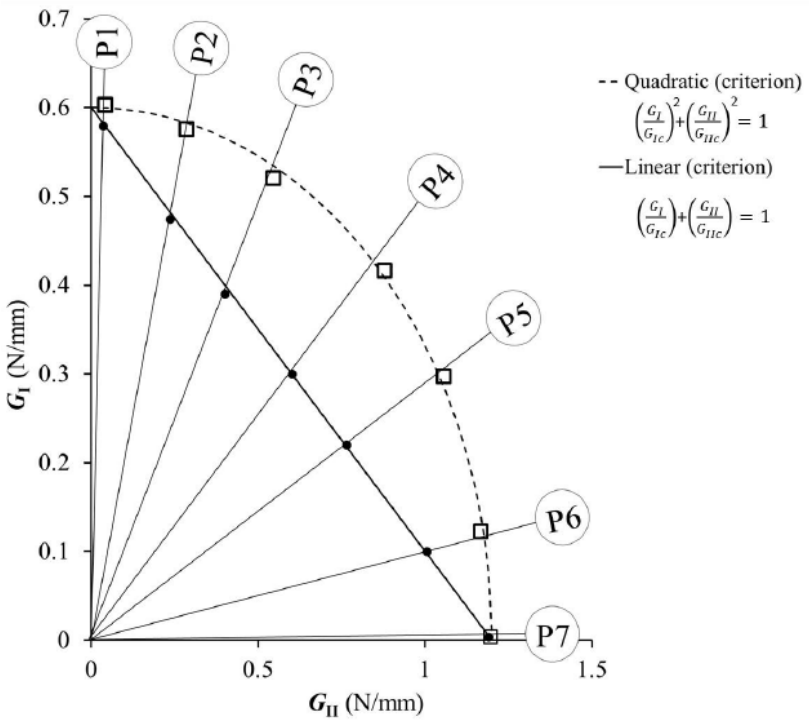

Figure 14: Fracture envelope for the cases analysed using a linear and quadratic criteria [10].

The toughness of the adhesive joints was measured using an apparatus capable of recreating a wide range of fracture modes from mode I to mode II (Figure 15). Using this loading jig and a universal testing machine, a load-displacement curve is obtained. This particular loading jig presents two main advantages [7]:

- It does not require the measurement of the crack, as the CBBM is used. Instead the displacement is obtained from two linear variable differential transformers (LVDT) connected to each beam.

-This invention places the specimen inside its structure, reducing the space needed for testing.

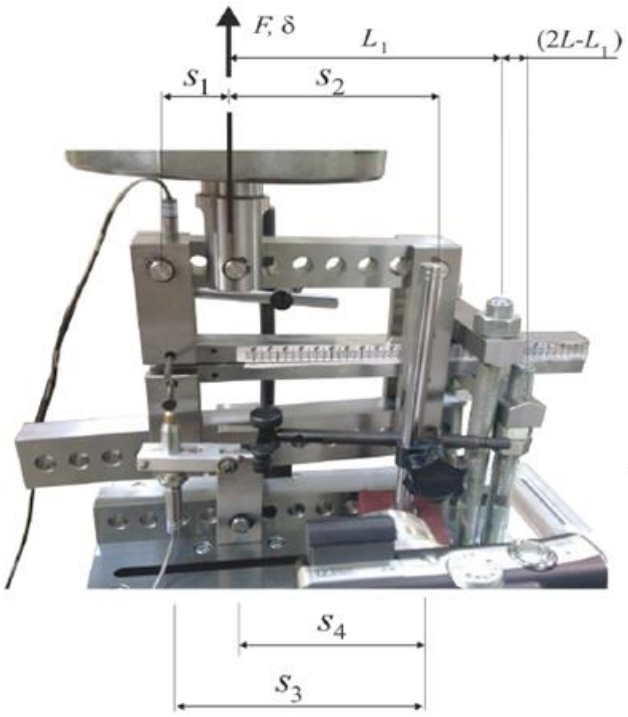

	Jig arrangement			
Scenarios	s_1 (mm)	s_2 (mm)	s_3 (mm)	s_4 (mm)
P1	100	40	140	-60
P2	120	40	160	-120
P3	40	120	160	40
P4	60	80	140	60
P5	60	80	140	120
P6	40	40	80	100
P7	100	40	140	80

Figure 15: Loading jig (set for mode I) and jig arrangements used (adapted from [7] and [10]).

2.6 Influence of moisture on adhesively bonded joints

The water uptake affects the mechanical properties of the adhesive, as well as the integrity of the adherend. This uptake may plasticize [13, 14] and swell the adhesive [15], cause unwanted chemical reactions, form cracks and crazes [16] and hydrate metallic substrates [4].

The eventual degradation of the interface is the main reason for failure of an adhesive joint. This occurs due to the following mechanisms [16]:

- Creation of a water film at the substrate-adhesive interface.
- Water movement through the adhesive, either by diffusion, capillaries or pores.
- Accumulation of water at the interface, caused by osmotic force, temperature differences and chemisorption or physisorption.
- Local increase of water molecules lateral to the driving forces mentioned above due to the continuous condensation of water.

2.7 Moisture uptake

Water may enter the adhesive joint by [17]: diffusion in bulk adhesive (Figure 16), transport along the interface, capillary action through cracks and crazes or diffusion through the adherend if permeable.

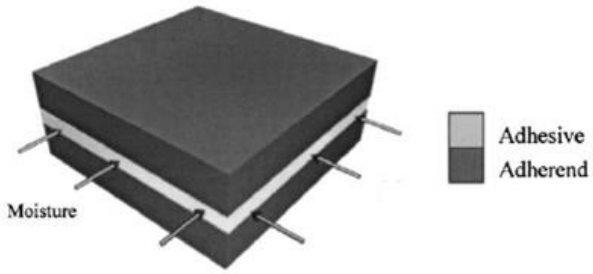

Figure 16: Moisture uptake of the adhesive of a single lap joint (adapted from [18]).

Moisture uptake is a diffusion process that occurs due to a concentration gradient that obeys Fick's laws and is a function of time, temperature, concentration and sheet thickness [17, 19-21]. According to this law, a gradient *dc/dx* causes a flux (F_X) in the same direction. Both parameters are related by the coefficient of moisture diffusion (*D*):

$$F_X = -D\frac{dc}{dx} \quad (24)$$

The concentration change as a function of time can be expressed by Fick's second law [20, 21]:

$$\frac{\partial c}{\partial t} = -D\frac{\partial^2 c}{\partial x^2} \quad (25)$$

The coefficient of moisture diffusion can be determined by measuring the slope of the theoretical absorption curve for one dimension Fickian behaviour (Figure 17) and can be defined as [19]:

$$D = (\frac{M_t}{M_\infty})^2 \times \frac{\pi}{16} \times \frac{h^2}{t} \quad (26)$$

Where M_t is the weight gained at each instant *t*, M_∞ is the mass attained at equilibrium (saturation) and *h* is the thickness of the adhesive.

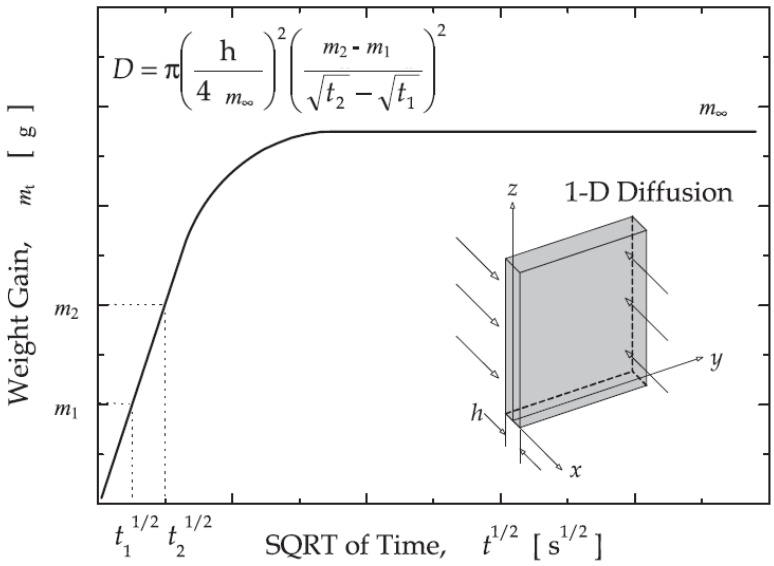

Figure 17: Theoretical absorption curve and diffusion parameters for one-dimensional Fickian diffusion [19].

While the environment's moisture content influences the mass uptake, the effect of the temperature may have an influence or not, depending on the adhesive [19]. However, the diffusion rate can increase significantly with the temperature [17, 22].

Due to the moisture uptake, swelling can occur. This phenomenon is a volumetric change which is independent of thermal expansion. Increasing the temperature will lead to a higher rate of water uptake and maximum water uptake [17]. Desorption will reverse the swelling effect [3, 23]. On the other hand, micro-cracking and hydrolysis are irreversible, promoting the degradation of adhesive properties [23].

2.8 Influence of water uptake on adhesive properties

The water uptake can lead to changes on the properties of the adhesive. These changes can occur due to the plasticization of the adhesive and adherend, which leads to a change of thermal and mechanical properties, involving: lower rigidity at room temperature, decrease of the glass transition temperature (T_g) [19] and increase of the strain failure at room temperature [24].

The glass transition temperature (T_g) decreases with the intake of water until a final value of T_g is achieved upon saturation (Figure 18). Factors such as the time of exposure and absorption rate do not influence this variation, making it dependent only of the water uptake [19].

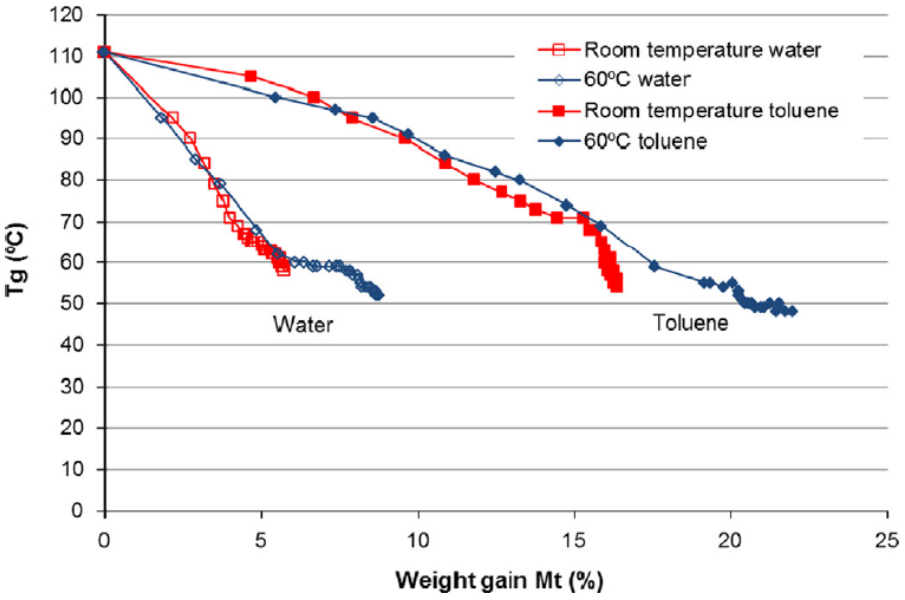

Figure 18: AV119 adhesive's Tg as a function of water or toluene uptake [19]. The final values represented correspond to the saturation of the adhesive.

A decrease of rigidity (Figure 19) and maximum tensile stress (Figure 20) can be observed, contrasting with an increase of the maximum strain (Figure 21) [18]. However, similarly to the swelling effect, these changes caused by plasticization can be partially or fully reversed with desorption [23].

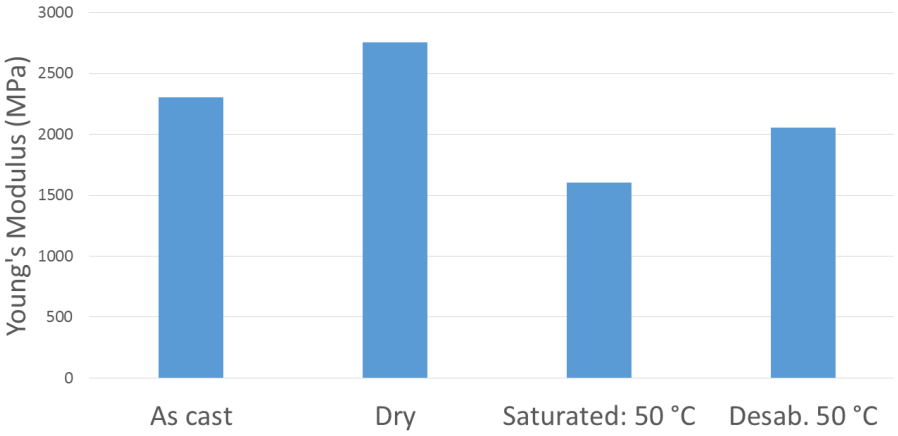

Figure 19: Young's Modulus for different moisture stages (adapted from [23]).

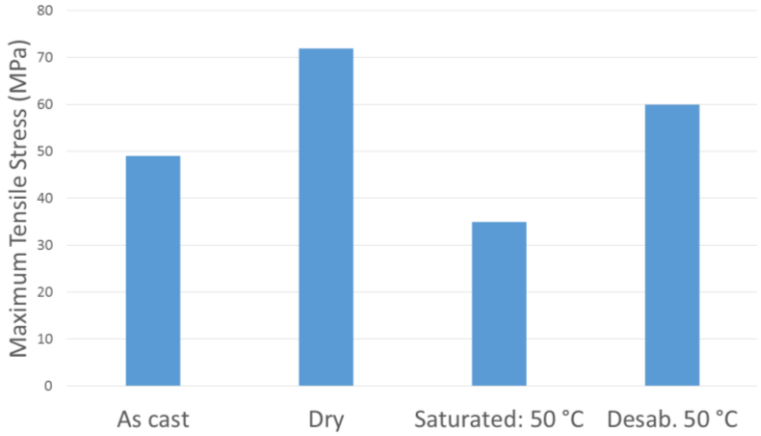

Figure 20: Maximum Tensile Stress for different moisture stages (adapted from [23]).

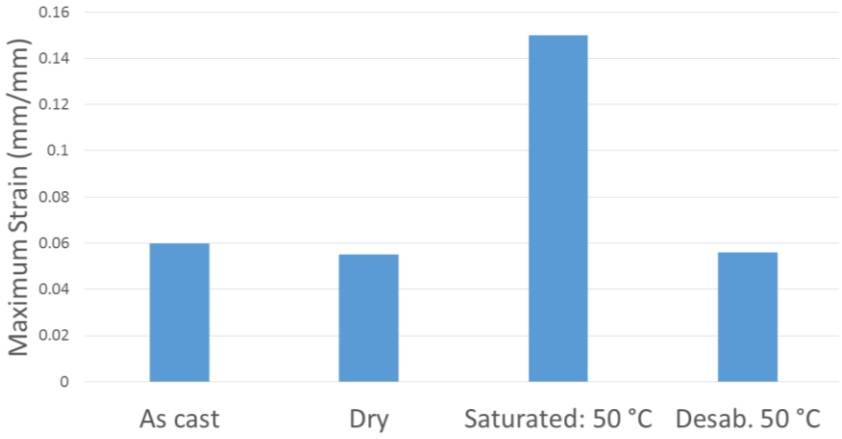

Figure 21: Maximum Strain for different moisture stages (adapted from [23]).

A decrease of the initial crack load with an increase of moisture uptake has also been reported (Figure 22). Once more, the reduction observed depended of the water uptake alone, being independent of the absorption rate and exposure time [18].

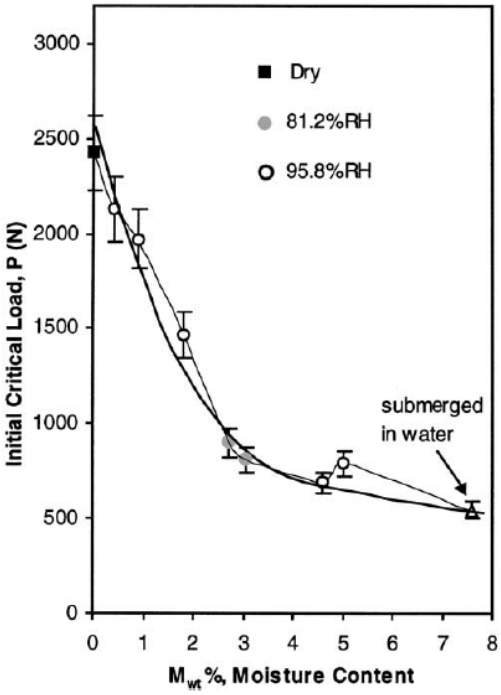

Figure 22:Initial critical load as a function of moisture content [18].

The presence of water on the adhesive leads to a reduction of its fracture toughness [1, 17, 25, 26] (Figure 23). Nonetheless, it has been reported an initial increase in strength due to plasticization effects followed by a decrease in the strength due to degradation [26] (Figure 24).

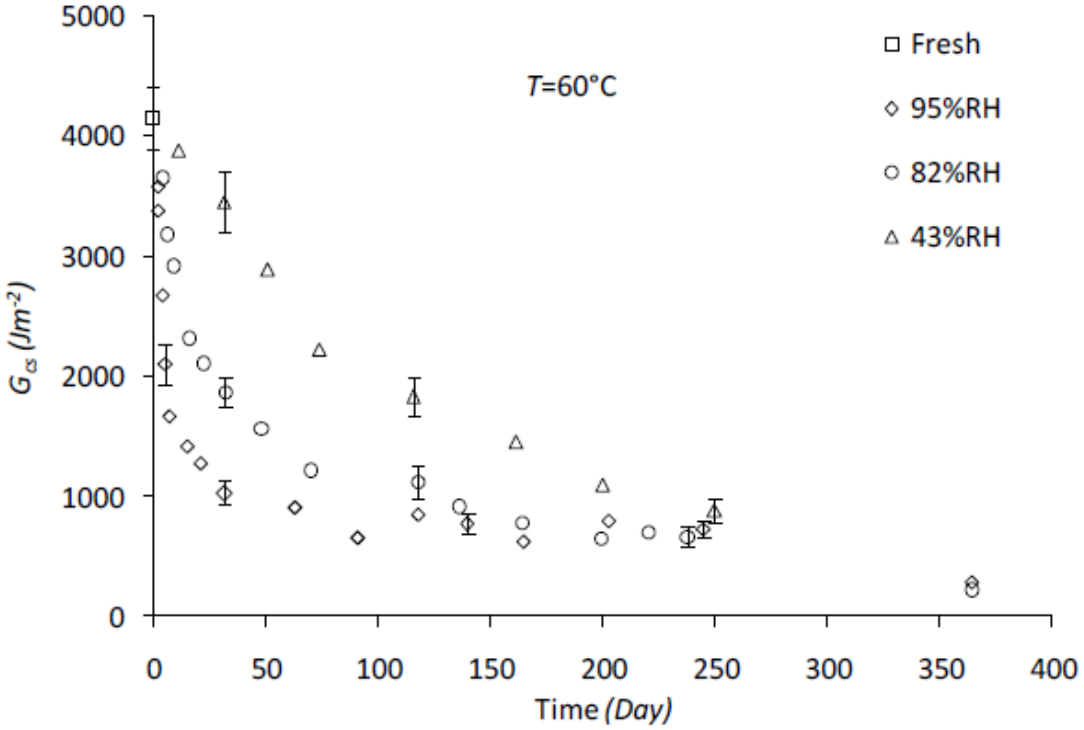

Figure 23: Variation of G_{cs} (ψ = 27°) with the time of exposure at 60°C and three different RH. Each data point without error bars is an average of at least 20 measurements within one DCB specimen. Each data point with an error bar is an average value obtained from three different DCB specimens. Error bars show the specimen-to-specimen standard deviation [25].

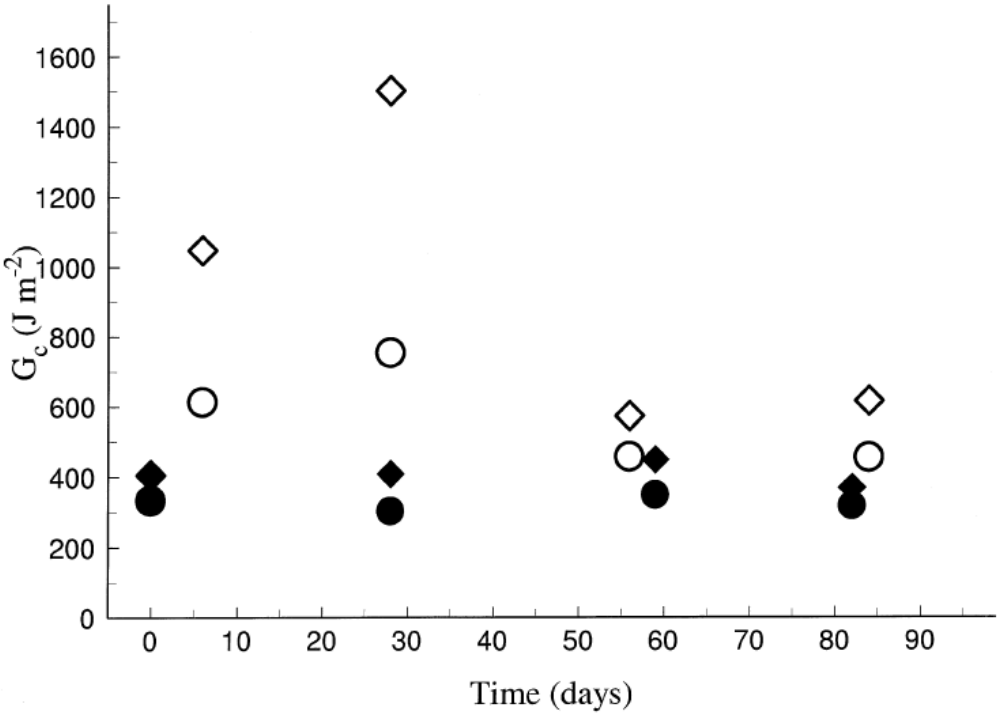

Figure 24: G_c versus exposure time for Cybond 4523GB degraded 100% relative humidity φ=48° (○) *and φ=60°* (□) *(wet) and in dry conditions φ=48°* (•) *and φ=60º* (♦) *[26].*

2.9 Diffusion in epoxies

The simple Fickian diffusion process can be observed in epoxies below the T_g. However, in many cases, this model does not represent the absorption process and leads to an overestimation of the water concentration [25]. These cases are known as non-Fickian or anomalous. Regarding thermosetting epoxy resins, two stages of moisture absorption are observed and can be described with a dual Fickian model (Figure 25) [25]. The dual Fickian model assumes a Fickian diffusion but considers the simultaneous existence of two mechanisms with different diffusion properties [25].

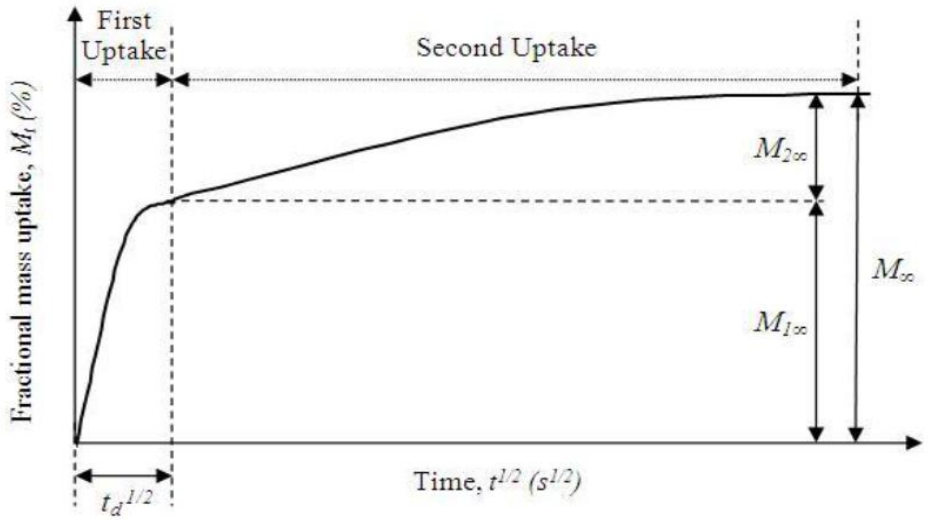

Figure 25: Schematic illustration of the sequential dual Fickian model [25].

The thickness of the adhesive also influences these two stages, as they are more visible when the adhesive layer is thinner adhesive (Figure 26). On the other hand, increasing the thickness of the adhesive leads to a lower overestimation of the water concentration using the simple Fickian diffusion model [27].

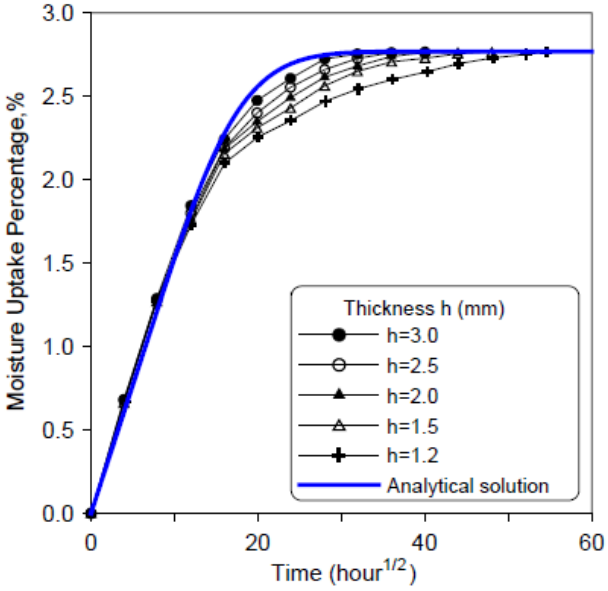

Figure 26: Moisture Uptake Percentage as function of different thicknesses [27].

2.10 Surface treatment

Surface treatment is one the most important steps during the manufacture of an adhesive joint (Table 1). The objective of this step is to create a more resistant surface, as well as making it more wettable [3]. The successfulness of an adhesive joint is much dependent on strong primary chemical bonds [28]. On the other hand, factors like surface area and mechanical interlocking are relevant on a much lower extent [28]. Furthermore, when exposed to the environment, phenomenon like hydration may occur, weakening the bond and causing mixed-mode or adhesive failures [5]. Scenarios like this can only be prevented with surface treatments, as paints and sealants only slow down the moisture diffusion [4].

Table 1: Influence of surface treatments on short and long-term strength of adhesive bonds [29].

Condition	Short-term effect	Long-term effect
Contaminated surface	Chemical reactions are inhibited Bonds are weak	Weak bond which fails soon after manufacture
Clean surface without hydration resistance	Short-term bonds are strong	Gradual degradation leads to interfacial failure. The joint strength will decay to zero
Clean and chemically active surface with hydration resistance	Short-term bonds are strong	Bond maintains integrity throughout its service life

Surface treatments follow three main steps: removal of surface contamination [29], chemical modification of the surface [29] and change of the surface's topography [3]. Analysis

of the performance of different surface treatments have been done based on the crack growth during a wedge test [17]. The result reveals a lower crack growth on phosphoric acid anodize (PAA), followed by chromic acid anodize (CAA), chromic acid etched (CAE), grit-blasting and degreasing (Figure 27) [17].

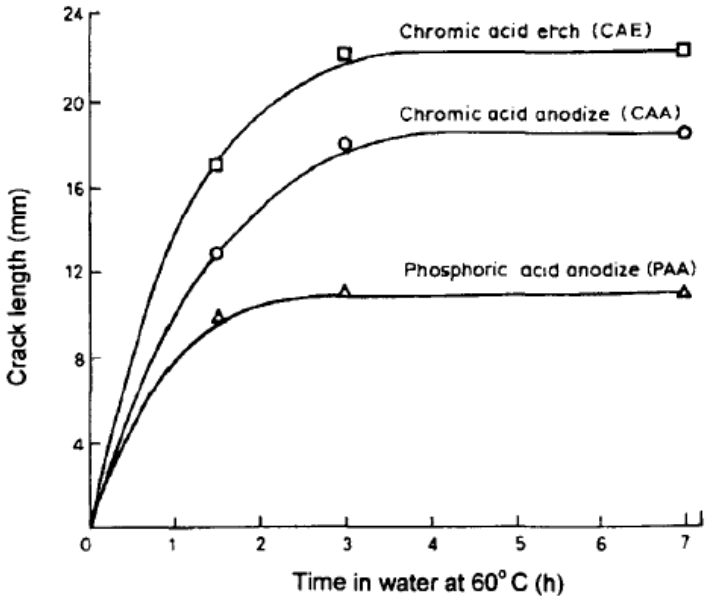

Figure 27: Crack growth on aluminium joints with different surface treatments (after Kinloch, [17])

A higher durability is achieved with PAA due to the formation of "micro-composite" structure of adhesive and oxides, where the porous arrangement of the oxide (Figure 28) is filled with the adhesive, increasing the contact area [17]. The structure and chemistry of the anodic oxide film depends on several factors, such as: the alloy being treated, pre-processing, electrolyte used, anodising temperature and time, voltage conditions and post-treatments (etching and sealing) [1].

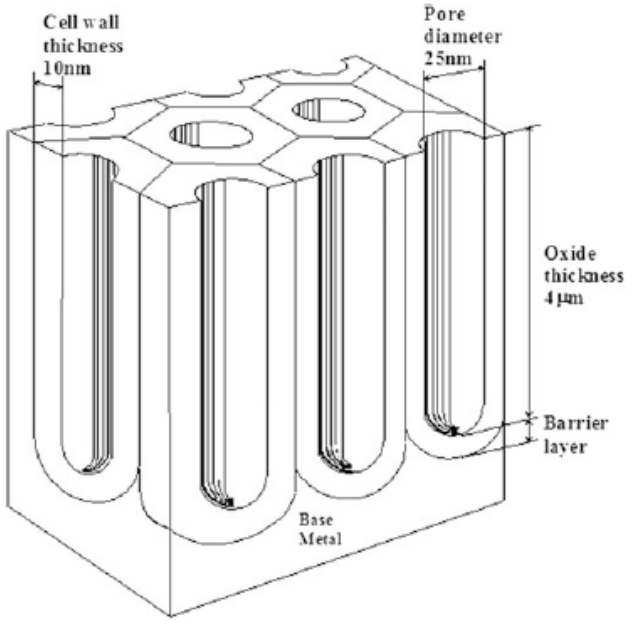

Figure 28: Idealised structure of an anodic oxide on aluminium [1].

3 Experimental details

In order to determine the fracture envelope as a function of water content, DCB specimens standardized by ASTM were used. However, due to the geometry of this specimen, the saturation process would take several years (Figure 29). In order to fully saturate the adhesive within the scope of a Master's thesis, open-DCB specimens (ODCB) were used to accelerate the diffusion process. Due to the configuration of the ODCB specimens, they are able to replicate the diffusion process that occurs in an adhesive plate (Figure 30 and Figure 31).

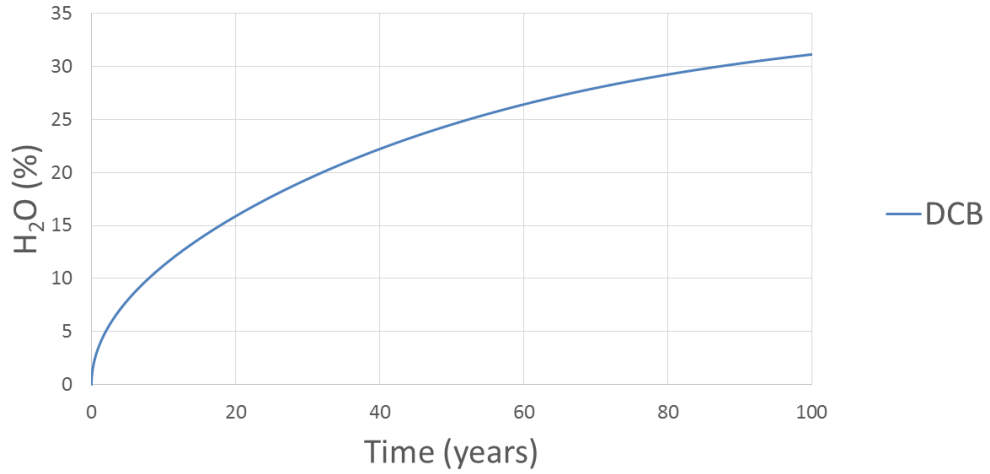

Figure 29: Water uptake of the adhesive SikaPower®-4720 in a DCB specimen when exposed to a 100% RH environment according to numerical simulations.

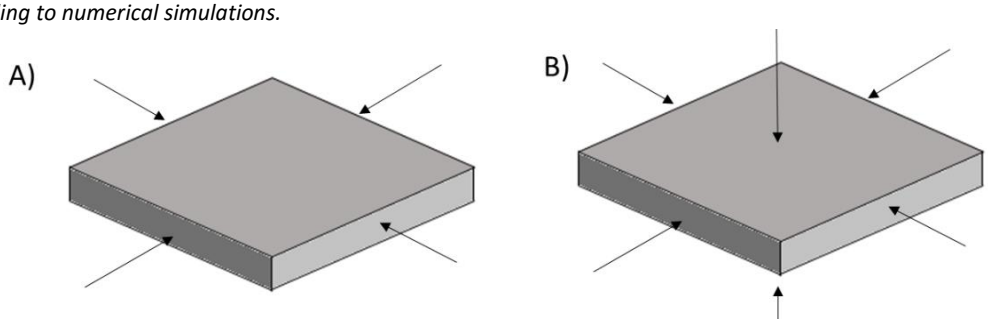

Figure 30: Diffusion paths: A) if the adhesive is in a DCB specimen, B) in an adhesive plate.

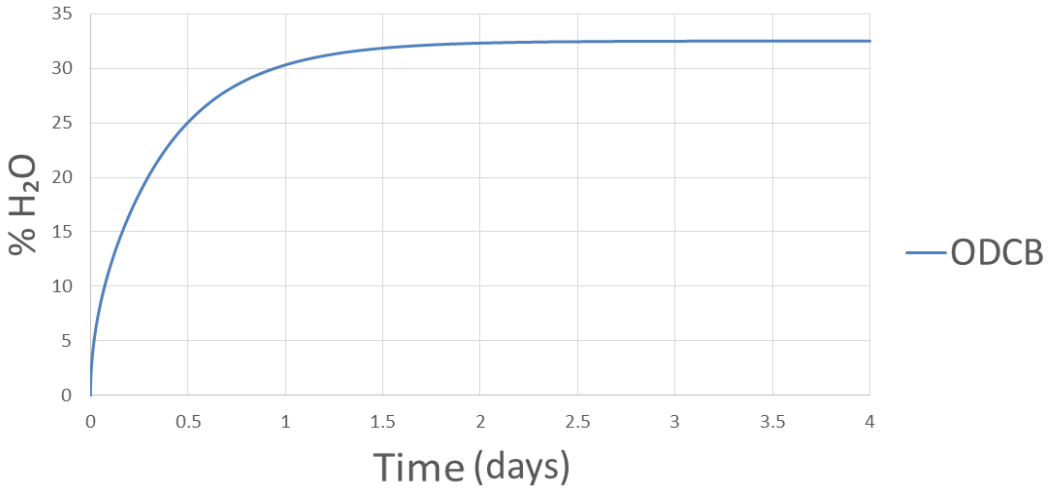

Figure 31: Water uptake of the adhesive SikaPower®-4720 in an ODCB specimen when exposed to a 100% RH environment according to numerical simulations

In this work, both types of specimens were used. The standard DCB specimen were used to determine the fracture envelope in a dry environment (0% RH), while the ODCB specimens were used to characterize the fracture envelope in a 75% and 100% RH environment.

To be able to compare the influence of water on the fracture envelope using two different specimens, it was necessary to determine the influence of their geometry in the value of the fracture toughness measured experimentally. This analysis was done only for mode I and assumed to be constant for the other modes.

The characterization of the fracture envelopes was done using three loading modes: pure mode I, mixed-mode 55° and mixed-mode 87°. Exceptionally, ENF tests will be done using DCB specimens in a dry environment to determine the G_{IIC} of the adhesive and be able to input this property in the numerical models. At least 3 valid tests will be done for each mode.

3.1 DCB specimens

3.1.1 Adherend

The adherend's material used for the DCB specimens was aluminium Al7075-T6 supplied by Lanema (Ovar, Portugal). Aluminium was chosen over steel due to the aging environment. When exposed to distilled or salt water, the steel adherend would be corroded. This situation can be completely avoided by using phosphoric acid anodized aluminium instead. The choice of this particular aluminium alloy (Table 2) was based on its yield strength, which is high enough to avoid any plastic deformation during the tests.

Table 2: Mechanical properties of aluminium Al7075-T6.

Maximum strength (R_m)	**Yield strength (R_p 0.2)**	**Hardness (Brinell)**
525 MPa	455 MPa	130-150

3.1.2 Specimen's geometry

To characterize the fracture envelope with DCB and MMB tests, a standard DCB specimen was used (Figure 8), in accordance to ASTM 3433-99.

3.1.3 Adhesive

SikaPower®-4720

SikaPower®-4720 is a two-component high-strength epoxy adhesive. It is specifically designed for metal, particularly aluminium, and composite panel bonding. The adhesive is not intended to use for body structural parts [30].

The two components were mixed in a centrifuge mixing machine, a SpeedMixer DAC 150TM (Hauchild, Hamm, Germany), for 1 minute at 3500 rpm. The adhesive is then cured at room temperature for 5 days.

The stress-strain curve, as well as the mechanical properties of this adhesive, have been determined previously with tensile tests using bulk specimens [31] (Figure 32 and Table 3). These tests were performed at a displacement rate of 1mm/min.

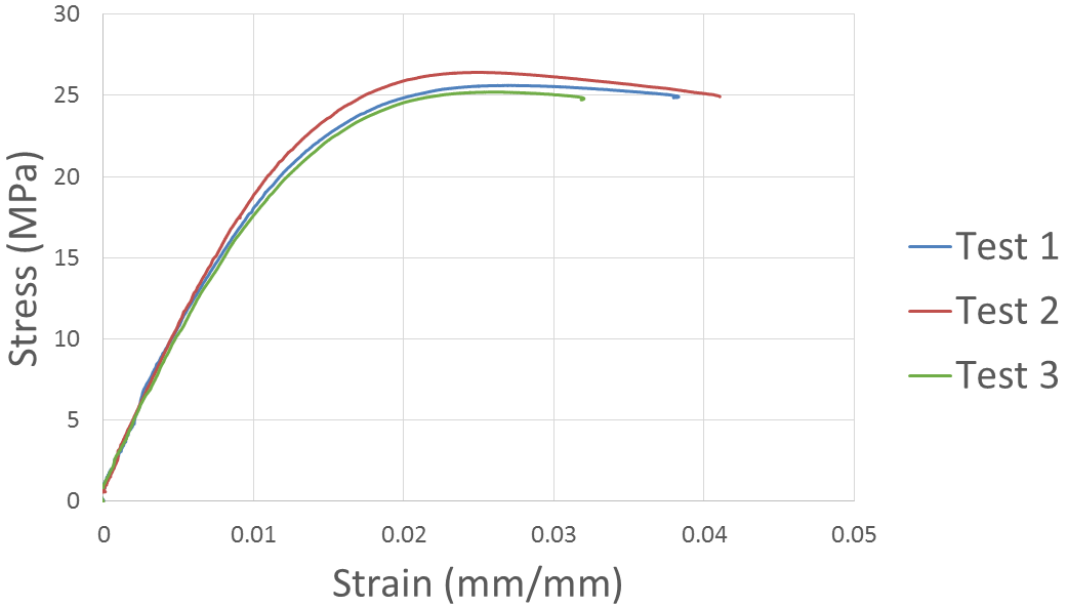

Figure 32: Stress-strain curve of dogbone specimens for SikaPower®-4720 [31].

*Table 3: Mechanical properties of SikaPower®-4720 [31, 32]. *Property deduced from tensile properties.*

Property	SikaPower®-4720
Young's modulus, *E* [MPa]	2170
Tensile strength, σ_{max} [MPa]	25.8
Strain to failure, ε_f[%]	2.7
Shear modulus, *G* [MPa]	800*
Shear strength, τ_{max} [MPa]	14.9*
Critical energy release rate, G_{Ic} [N/mm]	1.15
Traction toughness, G_{IIc} [N/mm]	4.5

3.1.4 Specimen manufacture

The specimen manufacture process can be divided in the following steps:

1. Mould preparation;
2. Substrate preparation;
3. Application of adhesive;
4. Application of pressure;
5. Curing stage;
6. Removal and cleaning;

Mould preparation

Before using the mould, its surface is cleaned with acetone to remove any trace of adhesive. After cleaning, a release agent was applied to the surface to prevent bonding between any adhesive excess and the mould plates.

Adherend preparation

The adherend preparation focuses on the application of a proper surface treatment that promotes a cohesive failure on the adhesive, avoiding a non-acceptable adhesive failure between the adhesive and the adherend.

The surface treatment was done following these stages:

- Grit blasting the adherends;
- Degreasing with acetone;
- Phosphoric acid-anodizing (PAA).

The PAA is the most suitable treatment for aluminium adherends. To anodize the aluminium, the adherends were dipped into a recipient filled with 12% concentrated solution of phosphoric acid and distilled water. The aluminium was then connected to the positive pole of a power source, while the negative pole was connected to a wire (cathode) dipped on the same solution. A 16 V tension is applied to the circuit during 20 to 25 min (Figure 33). After the anodizing process is completed, the aluminium adherends were cleaned using tap water and dried in air.

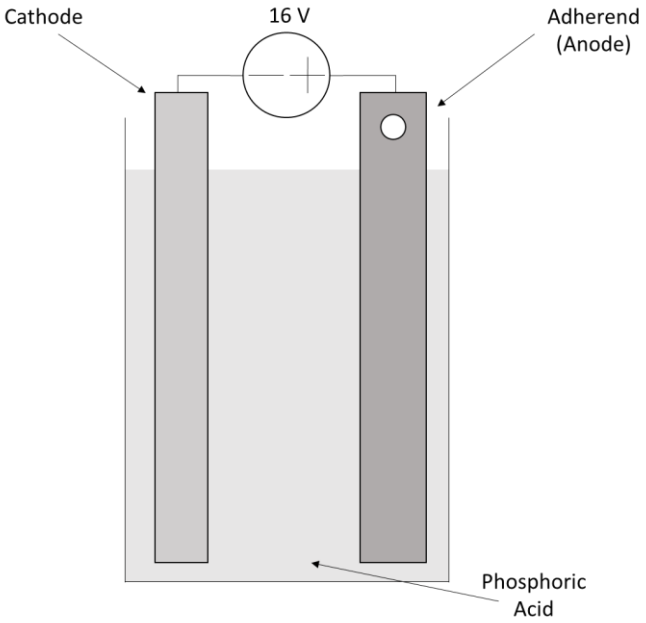

Figure 33: Scheme of the anodization's electric circuit.

Application of adhesive

In order to guarantee a constant thickness of adhesive, two spacers were inserted between the adherends. Both spacers were coated with a release agent. One of the spacers was a 0.2 mm steel plate which is placed on the end of the specimen. The other spacer was made of three components: a 0.1 mm blade glued to two 0.05 mm steel plates, one on each side. The latter also had the objective of creating a pre-crack and, therefore, was placed 45 mm away from the tip of the specimen.

Application of pressure

The mould with the DCB specimens was placed on a hydraulic press where sufficient pressure is applied.

Removal and cleaning

After curing, any excess of adhesive was removed using a rasp and sandpaper.

3.2 ODCB specimens

The open-DCB specimens are a modification of the standardized DCB specimens. They differ on the fact that, instead of one adhesive layer, the ODCB specimens are constituted by three adhesive layers: one primary bond and two secondary bonds (Figure 34)

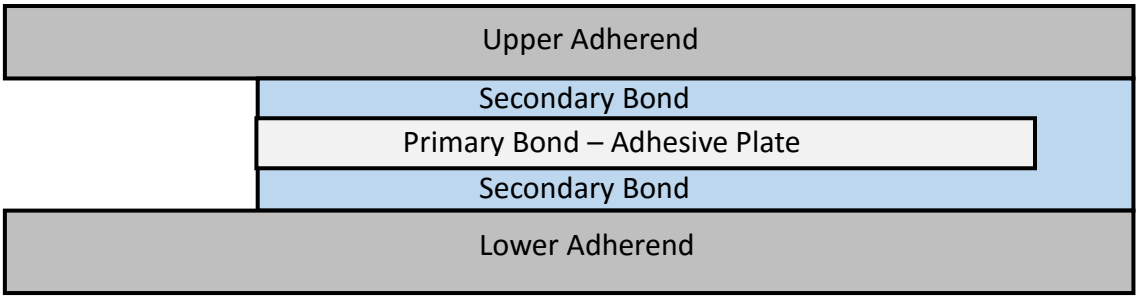

Figure 34: Scheme of an ODCB specimen.

The primary bond is a plate made of the adhesive that is meant to be degraded. The plate is produced in a mould and, after it is fully cured, it can be exposed to the aging environment. Since the adhesive plate is not bonded to any adherend, the area exposed to the environment is much larger than the area of adhesive on a standard DCB specimen, which accelerates the saturation process.

The secondary bond is a secondary adhesive, with higher mechanical properties, which is meant to bond the degraded adhesive plate to the adherends. For this reason, two layers of the secondary adhesive are used, one on each side of the adhesive plate.

3.2.1 Adherend

The adherend's material used for the ODCB specimens was the same that was used for the standard DCB specimens, aluminium Al7075-T6 supplied by Lanema (Ovar, Portugal). This choice was made for the same reasons stated previously.

3.2.2 Specimen geometry

The ODCB geometry is very similar to the standard DCB specimen (Figure 35). The only difference is the existence of three adhesive layers, one primary bond and two secondary bonds, instead of only one adhesive layer.

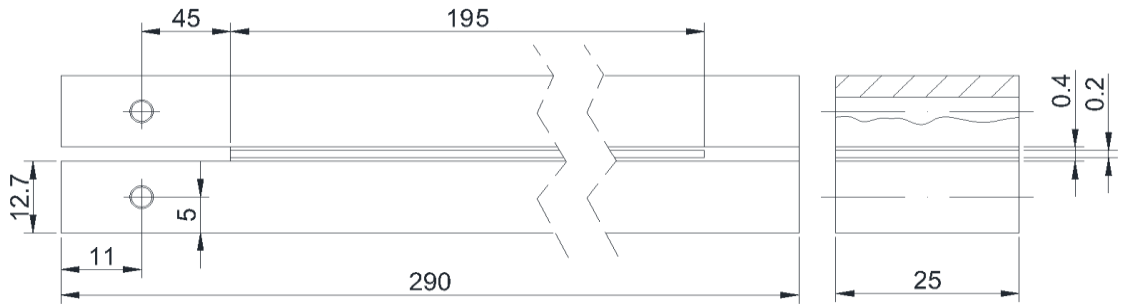

Figure 35: Definition draw of an ODCB specimen (dimensions in mm).

3.2.3 Adhesive

SikaPower®-4720 – Primary bond

The same adhesive used for the standard DCB specimens was used to make adhesive plates.

Araldite® 420 – Secondary bond for 75% RH

A two component epoxy, room temperature curing paste adhesive of high strength, toughness and moisture resistance. This adhesive cures at room temperature for 5 days.

This adhesive was chosen as a secondary bonding due to the higher mechanical properties (Table 4). Also, it has been used in the literature as a secondary bond for a similar process [18].

Table 4: Mechanical properties of Araldite® 420 A/B [33, 34].

Property	Araldite® 420 A/B
Young's modulus, *E* [MPa]	1800
Tensile strength, σ_{max} [MPa]	28.6
Shear modulus, *G* [MPa]	692
Shear strength, ζ_{max} [MPa]	16.5
Critical energy release rate, G_{Ic} [N/mm]	3
Traction toughness, G_{IIc} [N/mm]	12.5

During the experimental tests, this secondary bond would not adhere to the primary adhesive if the adhesive plate was degraded in a 100% RH environment. This would lead to adhesive failures that are not acceptable. However, it was proven that the secondary bond had no influence in the critical energy release rate. Therefore, it was possible to choose a different secondary bond for the 100% RH environment, Araldite® 2021.

Araldite® 2021 – Secondary bond for 100% RH

A two component toughened methacrylate adhesive system that cures at room temperature in 1 day.

This adhesive was chosen for its fast cure cycle, which minimizes the loss of water during the production of the ODCB specimens. It was also chosen for having slightly better mechanical properties than the primary adhesive (Table 5). In this environment, it is acceptable for the secondary bond and primary bond to have similar properties, as the mechanical properties of the primary bond will be degraded.

Table 5: Mechanical properties of Araldite® 2021 [35-37]

Property	Araldite® 2021
Young's modulus, *E* [MPa]	1130
Tensile strength, σ_{max} [MPa]	26.2
Shear modulus, *G* [MPa]	403.6
Shear strength, τ_{max} [MPa]	18.4
Critical energy release rate, G_{Ic} [N/mm]	1.6
Traction toughness, G_{IIc} [N/mm]	3.17

3.2.4 Specimen manufacture

The ODCB specimen manufacture process is similar to the one described for the DCB specimens, only differing in the existence of a step dedicated to the production of the adhesive plate. This process can be divided in the following steps:

1. Mould preparation;
2. Substrate preparation;
3. Adhesive plate manufacture;
4. Application of secondary bond;
5. Application of pressure;
6. Curing stage;
7. Removal and cleaning;

Due to the similarity to the previous process, only steps number 3, 4 and 6 will be described.

Adhesive plate manufacture

The adhesive plate, made of SikaPower®-4720, was produced in a mould coated with a release agent (Figure 36). After the adhesive is applied (Figure 37), the mould was placed in a hydraulic press and subjected to a 30 bar pressure for 8 hours. After this process, the adhesive was fully cured and could be removed from the mould to be cut into three plates.

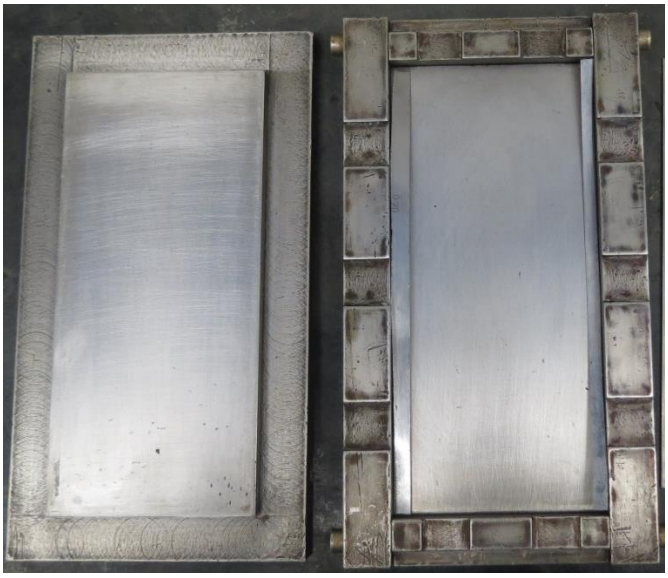

Figure 36: Mould used to produce adhesive plates.

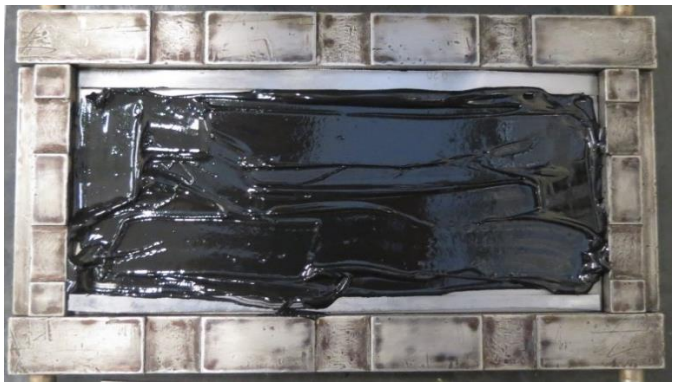

Figure 37: Mould with the adhesive SikaPower®-4720.

It is important to note that due to the size of the mould, the adhesive plate produced does not cover the whole specimen. However, the length of the adhesive plate (195mm) was long enough to reach the critical energy release rate during the DCB, ENF and mixed-mode tests.

After the adhesive plate is produced, it can be abraded with sandpaper and cleaned with acetone before and after being exposed to the aging environment (Figure 38). This procedure was adopted in order to allow a better adhesion between the primary and secondary bonds.

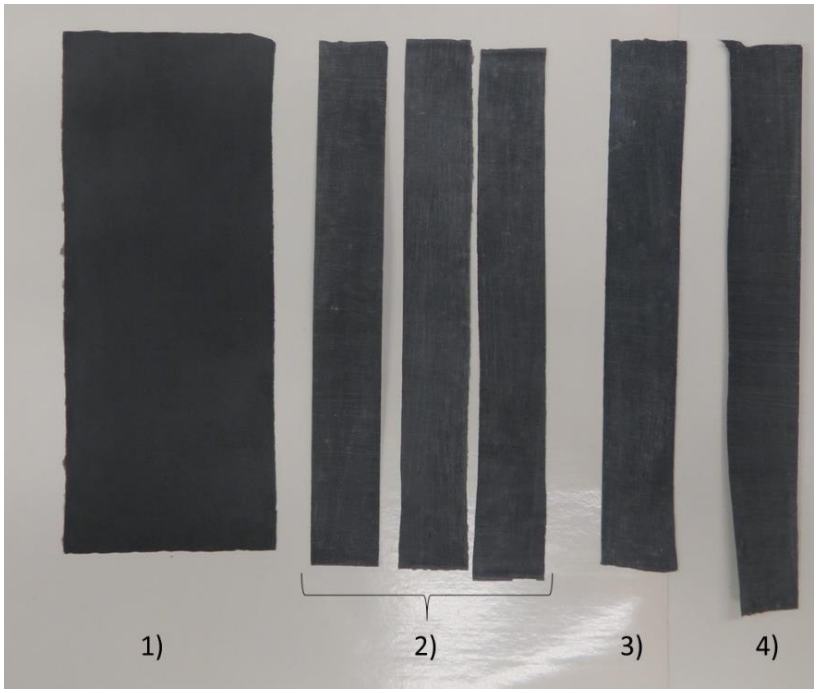

Figure 38: Adhesive plates on their 3 stages of production. 1) After curing and being removed from the mould. 2) After being cut into 3 pieces and then abraded with sandpaper. 3) and 4) after being degraded in a 75% RH or 100% environment, respectively.

Application of the secondary bond

This step is similar to the application of adhesive on the standard DCB specimens. However, in this case, the secondary bond was applied first, followed by the adhesive plate and finally the upper secondary bond was placed.

To ensure the thickness of the adhesive layers, spacers are used on both ends of the specimen. One of the spacers was a 0.4 mm steel plate, placed on the end of the specimen. The other spacer had the same thickness but was placed 45 mm away from the tip of the specimen. Unlike in the DCB specimens, using a blade to create a crack tip would have no effect as the adhesive plate is bonded in a solid state.

Curing stage

The curing stage of the ODCB specimens is equal to the cure cycle of the secondary bond, as the primary adhesive was cured during the manufacture of the adhesive plate. However, to avoid the evaporation of the water absorbed by the adhesive plate during its degradation, the secondary bond was cured at room temperature. This process takes 5 days for the adhesive Araldite® 420 A/B, used in the 75% RH environment, and 1 day for the adhesive Araldite® 2021, used in the 100% RH environment.

3.2.5 Validation of the ODCB specimens

Changing from DCB to ODCB specimens may have an influence in the fracture toughness measured experimentally. This change is justified by the change of thickness of the adhesive layer, which changes the shape of the fracture process zone, and by the inclusion of a secondary adhesive to bond the adhesive plate to the adherend (Figure 39).

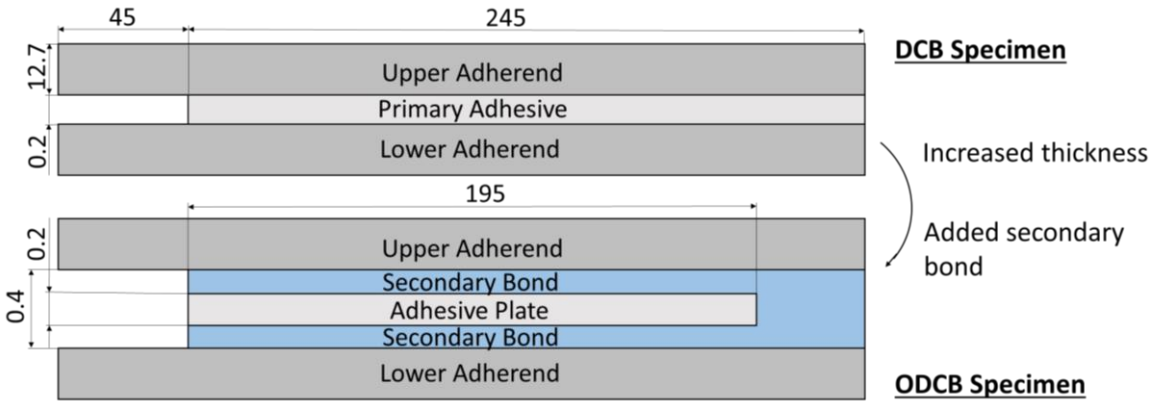

Figure 39: Differences between the DCB and ODCB specimens (dimensions in mm).

To validate the use of the ODCB specimens, a comparison between the mode I fracture toughness of 3 different specimen configurations was done. The first specimen was a DCB specimen with a 0.2mm thick adhesive layer. The second, a DCB specimen with a 0.4mm thick adhesive layer. The last one, an ODCB specimen which had an adhesive layer with a total thickness of 0.4mm (Figure 40).

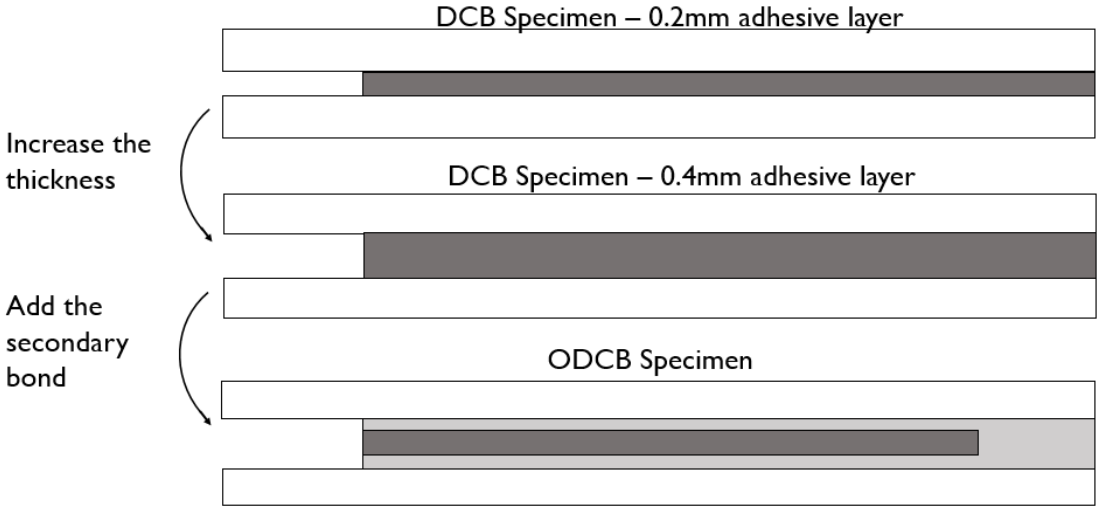

Figure 40: Three specimen configurations (DCB with 0.2 and 0.4 mm thick adhesive layer and ODCB specimen) and their differences.

With these three configurations it was possible to isolate the influence of the adhesive's thickness and the influence of the secondary bond. In the end, it was possible to understand if the fracture toughness measured was different and what is the cause of this change.

3.3 Specimen's ageing

The ageing of the adhesive was done by immersing the DCB specimens and the adhesive plates in a container with either distilled water or salt water at 32.5°C. The container with

distilled water created an environment with 100% relative humidity (RH), while the container with salt water created an environment with 75% RH [38, 39].

The standard DCB specimens were placed in a way that allows the contact between the sides of the adhesive layer and the water. These specimens were kept in the ageing environments since the 29th of April of 2016. These specimens were not tested in this thesis. Instead, the ageing process will be prolonged for as long as possible. In the future, they will be tested to validate the results of this thesis.

The adhesive plates were kept in the ageing environment for 4 days only. In this case, the area of contact between the adhesive and the water is much larger, which accelerates the saturation process, justifying the reduced exposure time. This time of exposure was estimated through a numerical model. However, to ensure that the saturation of the adhesive plate was achieved, the weight variation of the adhesive plate was measured. Once a constant value is reached, the adhesive is saturated.

3.4 Fracture tests

3.4.1 Mode I tests (DCB)

DCB tests were done to determine the G_{Ic} of the adhesive. To determine this value, three specimens were tested. During the DCB tests, an opening force is applied to the specimens. The load and displacements are recorded by the computers data acquisition system using an Instron® 3367 Universal Testing Machine (Norwood, USA) with a load cell of 30 kN. With the data collected, it is possible to determine the R-curves using the CBBM.

Before testing, a pre-crack was done to all specimens to avoid a blunt crack, which could lead to an increase of the energy required for the crack to propagate. After the pre-crack was done, the initial crack length was measured. The specimen was then tested at room temperature and at a constant displacement rate of 0.2mm/min.

Data analysis

Using the CBBM, the value of G_{Ic} can be determined according to the follow expression:

$$G_{Ic} = \frac{6P^2}{b^2h^3}\left(\frac{2a_e^2}{E_f} + \frac{h^2}{5G}\right) \quad (27)$$

Which depends only on the specimen's compliance, corrected flexural modulus (E_f), shear modulus of the adherend (G) and equivalent crack length determined by:

$$a_e = a + |\Delta| + \Delta a_{FPZ} \quad (28)$$

3.4.2 Mode II tests (ENF)

To determine the G_{IIc} of the adhesive, ENF tests were done. The equipment used for these tests was the same that was used for the DCB tests. The difference is that in this case the specimen was subjected to a shear stress.

Before testing, a pre-crack was done, the initial crack length was measured and a Teflon® film with an oil droplet was placed between the two adherends, to avoid any friction during the test.

Data analysis

Using the CBBM, the value of G_{IIc} can be determined according to the follow expression:

$$G_{IIc} = \frac{9P^2(a + |\Delta_{II}|)^2}{16b^2Eh^3} \quad (29)$$

In this particular test, it is quite difficult to monitor the crack length as the specimen is adhesive is being compressed. For that reason, the CBBM deserves a special mention, as it does not require the measurement of the crack length to determine the value of G_{IIc}.

3.4.3 Mixed-mode tests

To perform the mixed-mode tests, a loading jig was used (Portuguese patent nº 107188 B). This apparatus was designed to perform mixed-mode fracture tests on adhesively bonded DCB specimens (Figure 41). It can be equipped on a universal testing machine and, by adjusting its configuration, it is possible to apply loadings with a wide range of mode combinations that go from pure mode I to almost pure mode II.

The nominal phase angle of loading (φ), which characterizes each configuration of the equipment, can vary from 0° (pure mode I) to 90° (pure mode II) and is defined by the following equation:

$$\varphi = \tan^{-1}\left(\frac{\sqrt{3}\left(\frac{F_1}{F_2} + 1\right)}{2\left(\frac{F_1}{F_2} - 1\right)}\right) \quad (30)$$

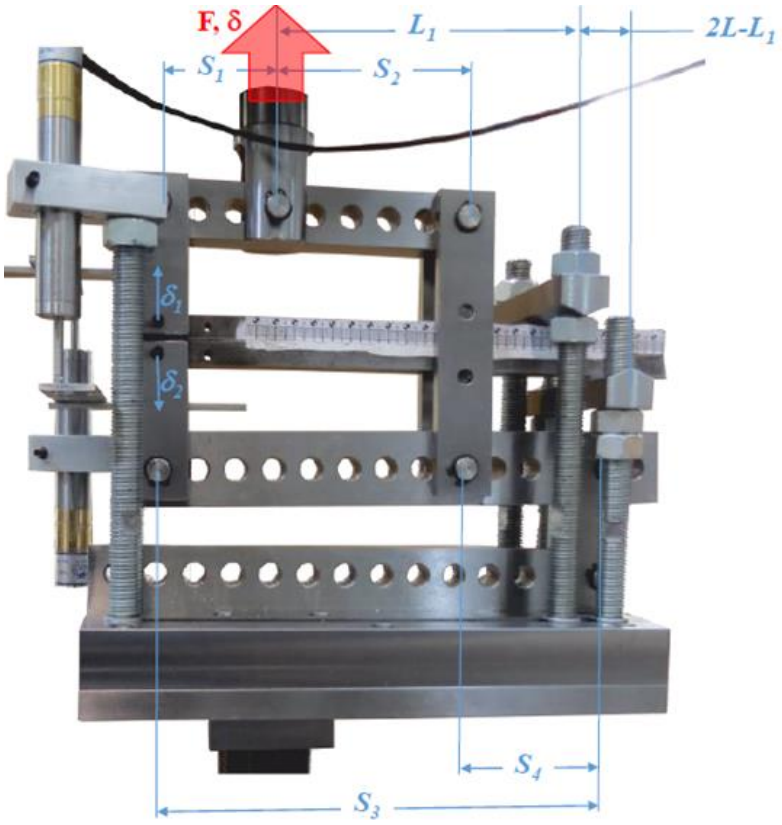

Figure 41: Mixed-mode apparatus.

Where F_1 and F_2 are the loads applied to the upper and lower substrate, respectively (Figure 42).

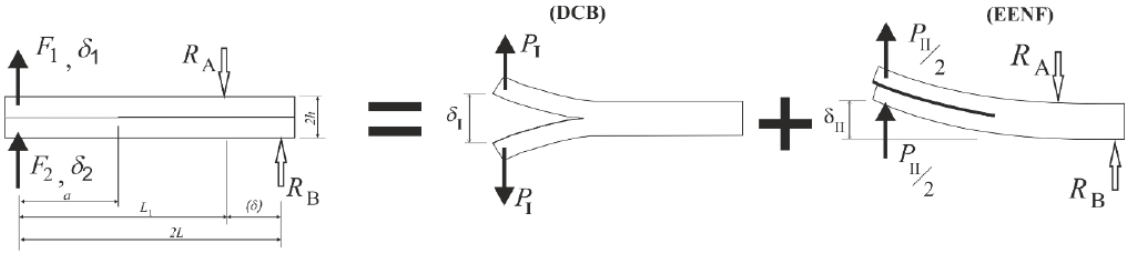

$$F_1 = F\frac{s_2}{s_3} \quad ; \quad F_2 = F\frac{s_1 s_4}{s_3\left(s_3+s_4\right)} \qquad P_I = \frac{F_1 - F_2}{2} \qquad P_{II} = F_1 + F_2$$

$$\delta_I = \delta_1 - \delta_2 \qquad \delta_{II} = \frac{\delta_1 + \delta_2}{2}$$

Figure 42: Free body diagram of the specimen, divided in component for mode I and II, when loaded on the apparatus.

During this test, 3 variables were recorded:

- The load applied to the apparatus, obtained from an Instron® 3367 Universal Testing Machine (Norwood, USA).
- Displacement of the upper and lower adherend, δ_1 and δ_2, obtained from two LVDTs attached to each beam.

Data analysis

The data obtained from the mixed-mode tests was analysed using the CBBM. This method requires the data obtained from the test, as well as the geometry and material properties of the adherend (B, h, E, G).

The fracture toughness's for mode I and II are then determined, independently from each other:

$$G_I = \frac{6P^2}{b^2h^3}\left(\frac{2a_{eI}^2}{E} + \frac{h^2}{5G}\right) \qquad (31)$$

$$G_{II} = \frac{9P^2a_{eII}^2}{4b^2Eh^3} \qquad (32)$$

4 Numerical modelling

4.1 Diffusion models

Two 1D finite element models were built in ABAQUS® to simulate the diffusion process in the standard DCB joint and in the adhesive plate, used for the ODCB specimens. The objective of these models is to determine the concentration of water in the adhesive. In order to do so, an analogy between heat transfer and moisture diffusion was used [17].

In both cases, a 2-node heat transfer link was used (DC1D2).

The water sorption parameters of the adhesive SikaPower®-4720 were reported in the literature [40].

Table 6: Diffusion parameters of the adhesive SikaPower®-4720 [40].

		$D_1\ (\mathrm{m^2/s})$	$m_\infty^1(\%)$	$D_2\ (\mathrm{m^2/s})$	$m_\infty^2(\%)$
SikaPower®-4720	Distilled water	1.2×10^{-13}	32.5	-	-
	Salt water	2.6×10^{-13}	2.0	2.5×10^{-14}	1.8

4.1.1 Diffusion in the DCB specimen

To simulate the diffusion in the DCB specimen, a 1D finite element model representing half the width of the adhesive layer was used (Figure 43). The decision of using a 1D model was based on two assumptions:

- The water uptake will only occur through the adhesive exposed to the aging environment. This assumes the inexistence of empty paths between the adhesive layer and the adherend that could accelerate the diffusion process.

- The water uptake perpendicular to the length of the adhesive layer is much larger than the uptake perpendicular to the width. This assumption is based on the geometry of the DCB specimen, where the length is much longer than the width.

Considering these assumption, a unidirectional diffusion process through the adhesive's thickness can be assumed.

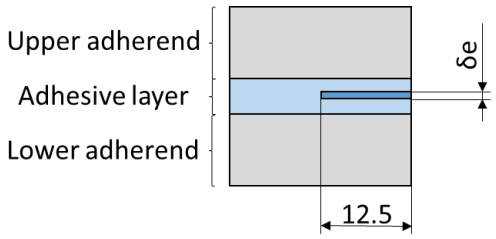

Figure 43: Representation of the 1D element modelled for the diffusion in the DCB specimen (dimensions in mm).

In total, this model has 500 elements and 501 nodes.

4.1.2 Diffusion in the adhesive plate

To simulate the diffusion in the adhesive plate, a 1D finite element model representing half the thickness of the adhesive plate was used (Figure 44). In this case, the use of a 1D model was based on the geometry of the adhesive plate. Since the water uptake can occur through all direction, and given the fact that the length and width of the plate are much larger than its thickness, a unidirectional diffusion process through the adhesive's thickness can be assumed.

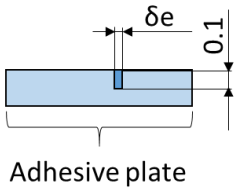

Figure 44: Representation of the 1D element modelled for the diffusion in the adhesive plate (dimensions in mm).

In total, this model has 500 elements and 501 nodes.

4.2 Fracture tests

Numerical models were developed in ABAQUS® to simulate the 4 fracture tests (DCB, MM 55°, MM 87° and ENF) for both DCB and ODCB specimens. The models used for the DCB specimens consider elastic elements for the adherends and cohesive elements for the adhesive.

CZM's model three different stages of the failure process: an elastic loading, damage initiation and the propagation that occurs due to local failure within the material. This type of model establishes a relationship between stresses and relative displacements between nodes, allowing the simulation of an elastic behaviour followed by a softening and gradual degradation of the material properties [41].

For the ODCB specimens, two possible scenarios were modelled (Figure 45):

1) The primary adhesive is modelled with a cohesive element and the secondary adhesive with an elastic element, making a total of only 1 cohesive layer. This enables the possibility of analysing the stress through the thickness of the secondary bond. However, it assumes that the crack will always propagate in the primary adhesive.
2) Both primary and secondary adhesives are modelled using a 50% ratio of cohesive elements and elastic elements, making a total of 3 cohesive layers. This gives the possibility of analysing the degradation of both primary and secondary adhesive, as it assumes that the crack can propagate in all three adhesive bonds.

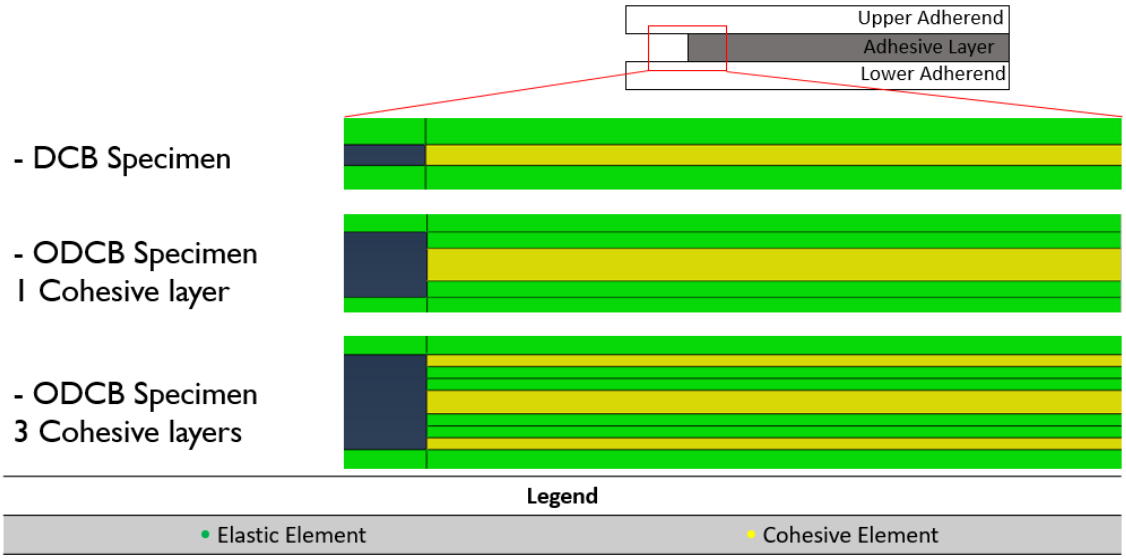

Figure 45: Pictures of the 3 specimen configurations modelled (not to scale).

In all three cases, the elastic elements were modelled using 4-node bilinear plane strain quadrilateral elements (CPE4R in ABAQUS®), while the cohesive elements used 4-node two-dimensional cohesive elements (COH2D4 in ABAQUS®). The mechanical and cohesive properties used in the simulations are shown in Table 7. A triangular traction-separation law available in ABAQUS® was used. This law assumes an elastic behaviour up to σ_f or τ_f. The shear maximum relative displacements are calculated based on the area below the traction-separation law (G_{Ic} and G_{IIc}).

Table 7: Elastic and cohesive properties.

	Elastic Properties		Cohesive Properties				
	E [GPa]	ν	G [MPa]	σ_f [MPa]	τ_f [MPa]	G_{Ic} [N/mm]	G_{IIc} [N/mm]
Aluminium	70	0.33	-	-	-	-	-
SikaPower®-4720	2.171	0.35	750	25.8	15.5	1.15	4.5
Araldite 2021	1.130	0.35	404	26.5	18.4	1.6	3.17

Due to the different thickness of the adhesive layers, the mesh applied to each one of these three model types was different. However, all the different mesh refinements used were based on the same principle: maximizing the quality of the mesh in the adhesive layer, where the crack propagate, and applying a less refined mesh in less critical zones, such as the top and bottom of the specimen. The different mesh refinements applied to each model type are shown in the figures below. For any other component used in these tests, a uniform mesh with a 0.2mm element size was used.

DCB specimen

For the DCB and mixed-mode tests, the mesh's element size changes from 1mm, in the extremes of the specimen, to 0.2mm in the adhesive (Figure 46).

However, for the particular case of the DCB specimen with a 0.4mm thick adhesive layer, the mesh shown in Figure 47 was used, where the refinement of the elements change from 1mm to 0.4mm in the adhesive layer.

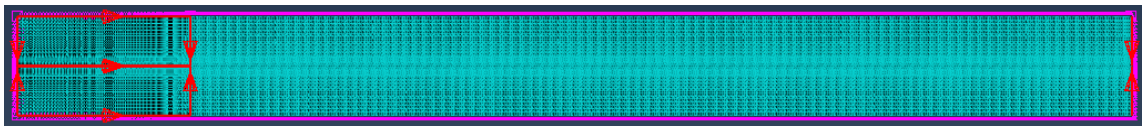

Figure 46: Mesh applied to the DCB specimen for the DCB and mixed-mode tests.

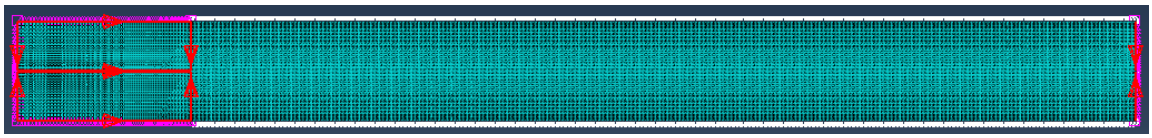

Figure 47: Mesh applied to the DCB specimen with 0.4mm thick adhesive layer.

ODCB specimen – 1 and 3 cohesive layers

The most refined mesh was applied to the DCB and mixed-mode tests, where the mesh's element size decreases from 1mm, in the extremes of the specimen, to 0.05mm in the adhesive (Figure 48). The reason behind the refinement used is that the secondary bond was divided in two partitions: a 0.05mm thick layer modelled with elastic elements and another equal layer modelled with cohesive elements, making a total of a 0.1mm thick secondary bond.

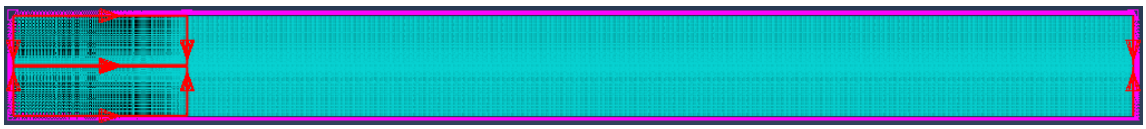

Figure 48: Mesh applied to the ODCB specimens, with 1 or 3 cohesive layers, used for the DCB and mixed-mode tests.

4.2.1 Mode I

To model this test, a pinned support was applied to the lower adherend, representing the pin that connects the specimen to the testing machine, and a vertical displacement was applied to the upper adherend. When both boundary conditions are applied, the upper adherend moves vertically from its pair and creates and opening load. The dimension of this problem and its boundary conditions can be seen in Figure 49 and Table 8.

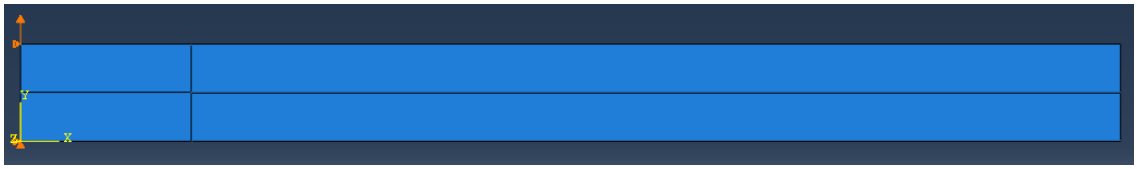

Figure 49: Assembly and boundary conditions used for the DCB test.

Table 8: Dimensions of the 3 DCB test problems.

	DCB Specimen	ODCB Specimen – 1 Cohesive layer	ODCB Specimen – 3 Cohesive layers
Number of elements	66975	417698	427498
Number of nodes	68432	422964	432766
Total number of variables	136864	845928	865532
Cohesive elements	1225	4900	14700

In order to validate the influence of the secondary bonding, another Mode I model was developed. The only difference is the thickness of the adhesive layer, which is 0.4mm in this case. The dimension of this problem is shown in Table 9.

Table 9: Dimensions of the DCB test problem using a DCB specimen with a 0.4mm thick adhesive layer.

	DCB Specimen – 0.4mm
Number of elements	26529
Number of nodes	27320
Total number of variables	54640
Cohesive elements	1225

4.2.2 Mixed-mode 55°

In the mixed-mode simulations, part of the apparatus used for the experimental tests was modelled. It was necessary to include 4 beams, with a rectangular cross section equal to the real equipment and modelled with beam elements, which were connected to each other and to the specimen with pin multi-point constraints. Similarly to the experimental test, the load is applied to the upper bar, causing the other beams to move and create a combination of both opening and shear modes.

The dimension of this problem and its boundary conditions can be seen in Table 10 and Figure 50.

Table 10: Dimensions of the 3 mixed-mode 55° test problems.

	DCB Specimen	**ODCB Specimen – 1 Cohesive layer**	**ODCB Specimen – 3 Cohesive layers**
Number of elements	70147	420868	430668
Number of nodes	77953	432479	442281
Total number of variables	146395	855453	875057
Cohesive elements	1225	4900	14700

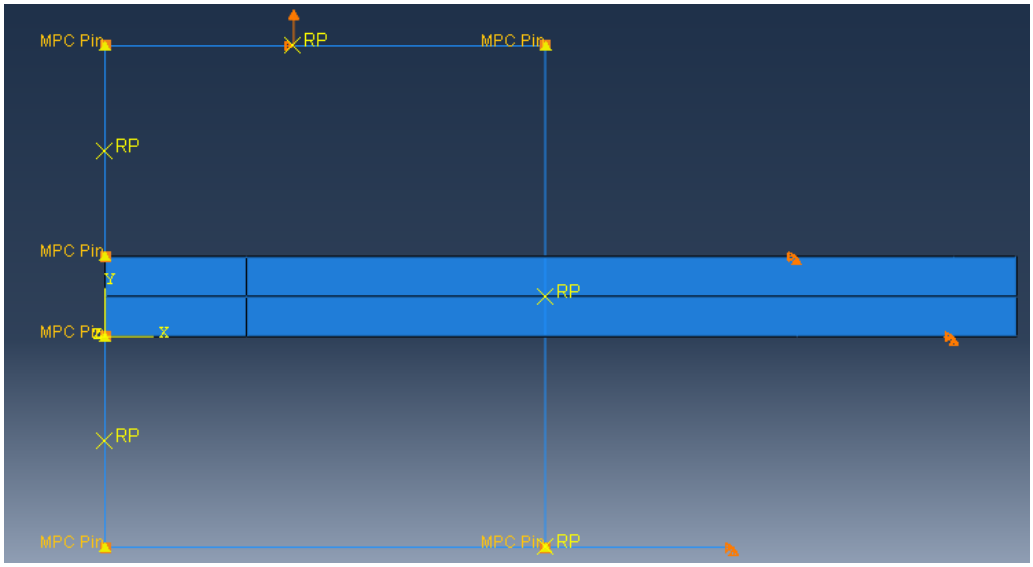

Figure 50: Assembly and boundary conditions used for the mixed-mode 55° test.

4.2.3 Mixed-mode 87°

This mixed-mode was modelled the same way as the previous one. The only difference being the dimensions of the 4 beams and the points where the boundary conditions are applied. The dimension of this problem and its boundary conditions can be seen in Table 11 and Figure 51.

Table 11: Dimensions of the 3 mixed-mode 87° test problems.

	DCB Specimen	ODCB Specimen – 1 Cohesive layer	ODCB Specimen – 3 Cohesive layers
Number of elements	70247	420968	430768
Number of nodes	78253	432779	442581
Total number of variables	146695	855753	875357
Cohesive elements	1225	4900	14700

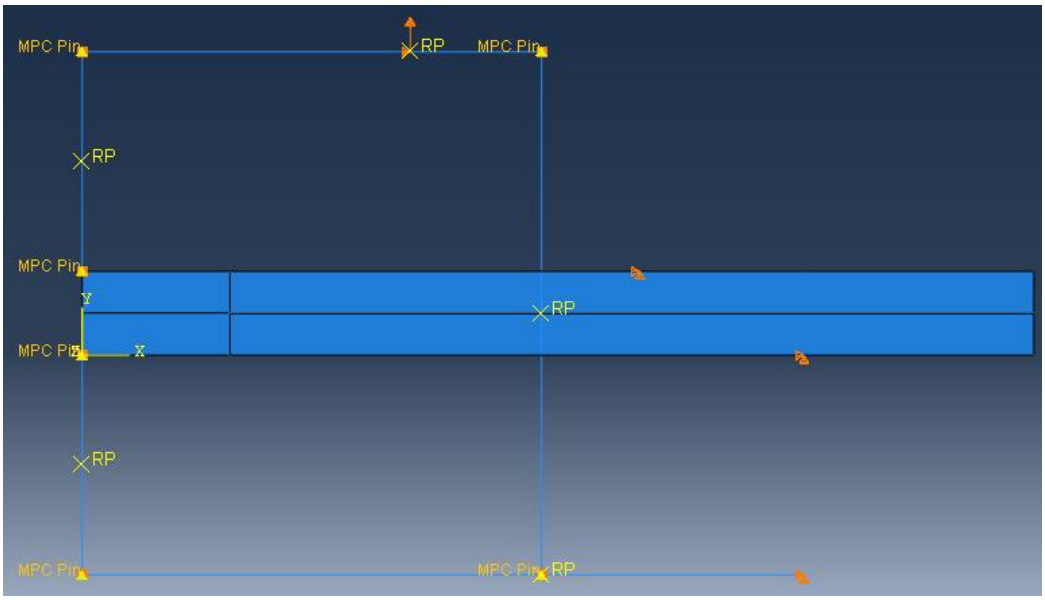

Figure 51: Assembly and boundary conditions used for the mixed-mode 87° test.

5 Results and discussion

In this chapter, both experimental and numerical results are presented and compares. At the end of each section, an analysis and discussion of the results is done.

5.1 Diffusion analysis

Considering the diffusion parameters mentioned in Table 6 and the experimental measurements of the adhesive's plate mass, the results shown in Figure 52 were obtained.

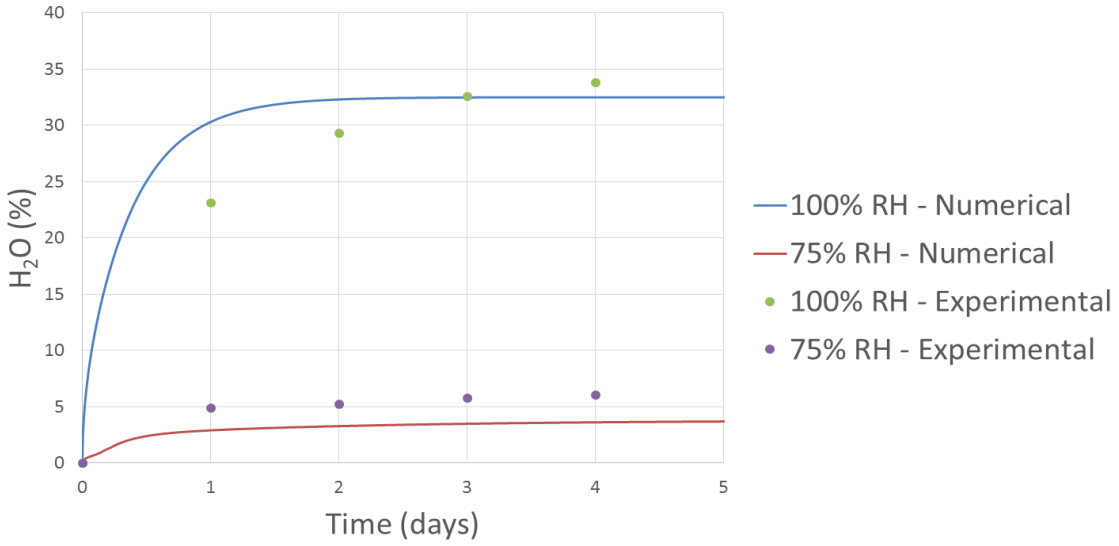

Figure 52: Experimental and numerical results for the mass uptake of the adhesive plate submerged in distilled water.

The numerical simulations suggested that the adhesive plates would be saturated after 2 days, in both environments. However, the experimental results show that the diffusion process is slower. The reason behind this difference is that the data used for the numerical models was determined with a 1 mm thick specimen, 5 times larger than the adhesive plates. As studied in the literature, the diffusion coefficient and the saturation levels change as a function of the specimen's thickness [42].

Using the experimental results, the diffusion coefficient and saturation level were updated (Table 12) and reintroduced in the numerical model. The results are shown in Figure 53.

Table 12: Corrected diffusion parameters for the adhesive SikaPower®-4720.

		$D_1\ (\mathrm{m^2/s})$	$m_\infty^1(\%)$	$D_2\ (\mathrm{m^2/s})$	$m_\infty^2(\%)$
SikaPower®-4720	Distilled water	0.4×10^{-13}	35.0	-	-
	Salt water	3.0×10^{-13}	4.7	1.5×10^{-14}	1.5

For the 100% RH environment, both experimental and numerical results show a good agreement. In other words, the simulation done to estimate the saturation time was validated. The same can be said for the 75% RH environment, although the value of D_1 seems to have been overestimated. To accurately determine this value, a thorough diffusion analysis would be required during the first day of ageing.

In the end, it was proven that the adhesive plates are saturated at the end of 4 days, for both 75% and 100% RH environments.

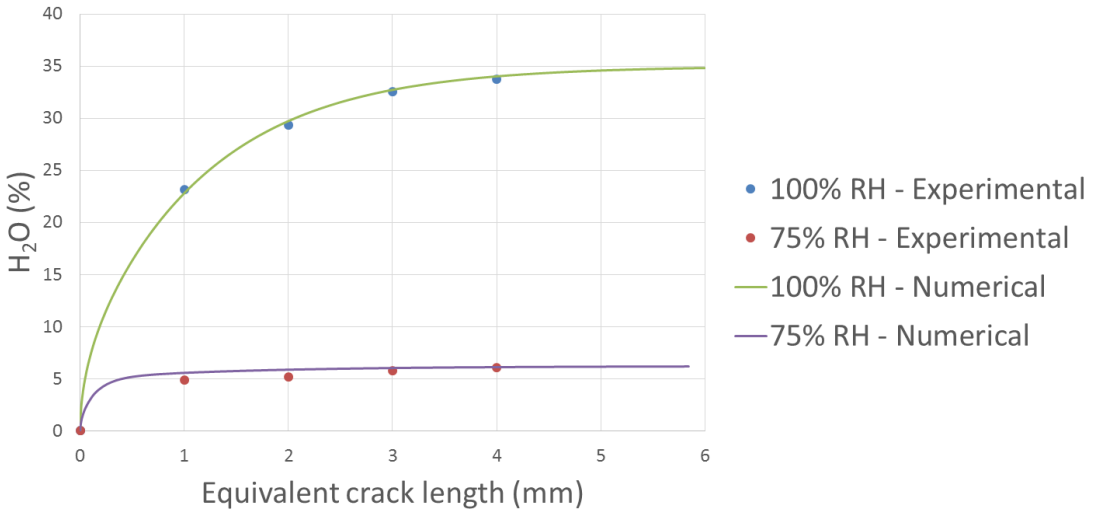

Figure 53: Updated numerical and experimental results for the mass uptake of the adhesive plate submerged in distilled water.

5.1.1 Swelling measurement

During the saturation process in both environments, the variation of the adhesive plate's length was measured. There are two reasons behind this measurement: first, the expansion of the adhesive in a joint can induce significant strain [15], making it an important factor in the joint design process, and second, the length of the adhesive plate can influence the load-displacement curves obtained. The latter will help explain some of the results described in Chapter 5.2.

The swelling of the adhesive plate is more noticeable on its length, as this dimension is much larger than the width or thickness. For this reason, only the variation of the length was measured. The results obtained are shown in Figure 54.

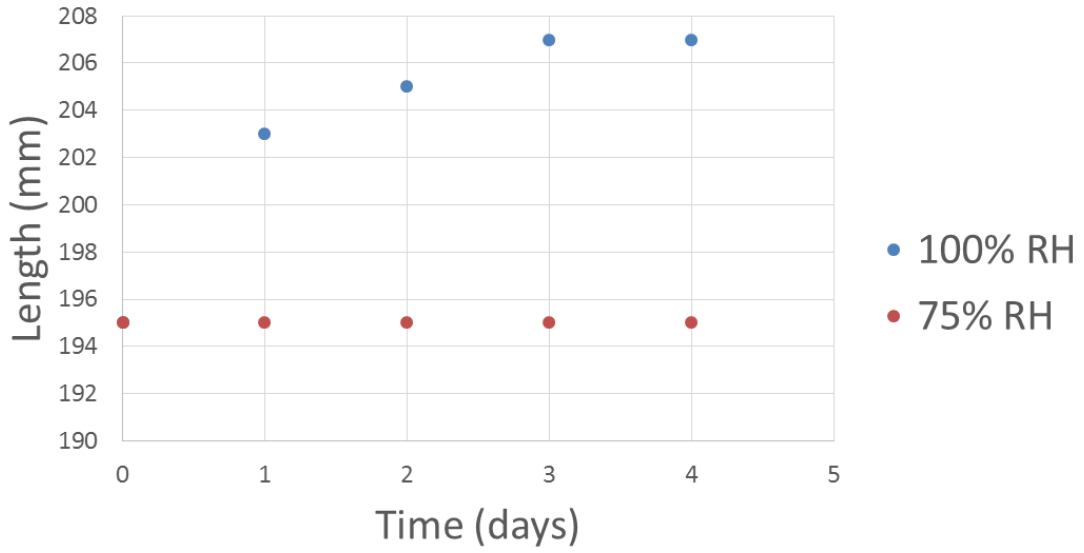

Figure 54: Variation of the adhesive plate's length as a function of time for both 100% and 75% RH environments.

In both cases, the initial length is equal to 195mm. However, while there is a significant length increase in the 100% RH environment, no variation is observed in the plate aged in salt water. This difference in results can be justified with the mass uptake registered in both

environments. For instance, the fact that no swelling is observed in the 75% RH environment is supported by the low mass uptake measured. On the other hand, there is a 35% mass increase in the 100% RH environment, which sustains the increase in length reported. Furthermore, the T_g of SikaPower®-4720, when saturated in distilled water, is below room temperature [40], making the adhesive more susceptible to volumetric changes. In the 75% RH environment, the T_g is above room temperature, making the adhesive less prone to swelling effects.

5.2 Toughness tests

In this chapter, a representative curve of each test will be presented for the three ageing environments, as well as a comparison with the respective numerical simulation. This analysis will be shown in detail for mode I, since it was the mode used to validate the use of the ODCB specimens. For the mixed-mode at 55° and 87°, only the analysis in the dry environment is described, as the process is equal for all the environments. At the end of this chapter, an analysis of the influence of water on the fracture toughness of 3 loading modes is done. Also, the results of the ENF tests are described in this section, although they were only used to determine the value of G_{IIC} to input in the numerical models.

5.2.1 Mode I

5.2.1.1 DCB – 0% RH

The DCB tests were used to determine the fracture toughness of the adhesive for mode I, G_{Ic}. During these tests, there was no plastic deformation of the aluminium adherend and a cohesive failure was observed for all the tested specimens (Figure 55).

Figure 55: Typical failure surfaces of a DCB specimen tested under mode I in a dry environment.

The normal load-displacement curve obtained from the DCB tests can be seen in Figure 56.

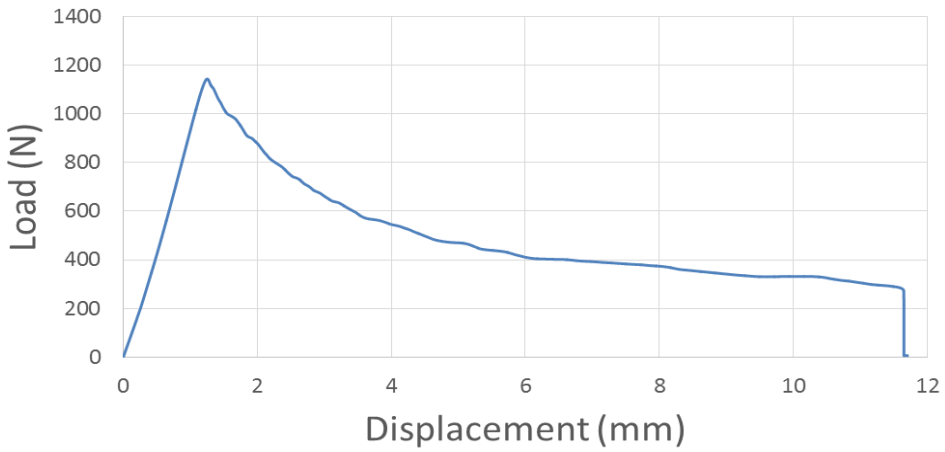

Figure 56: Representative load-displacement curves of the DCB specimens tested under mode I loading in a 0% RH environment.

The initial loading peak, critical load, corresponds to the moment when the elastic energy stored is equal to the energy required for the crack propagation, G_{Ic}. The beginning of the crack propagation is characterized by the reduction of the applied load.

Using the CBBM, it is possible to determine the R-Curves for these specimens, which can be seen in Figure 57. As the crack progresses, the energy release rate reaches a plateau that defines the critical energy release rate under mode I, G_{Ic}.

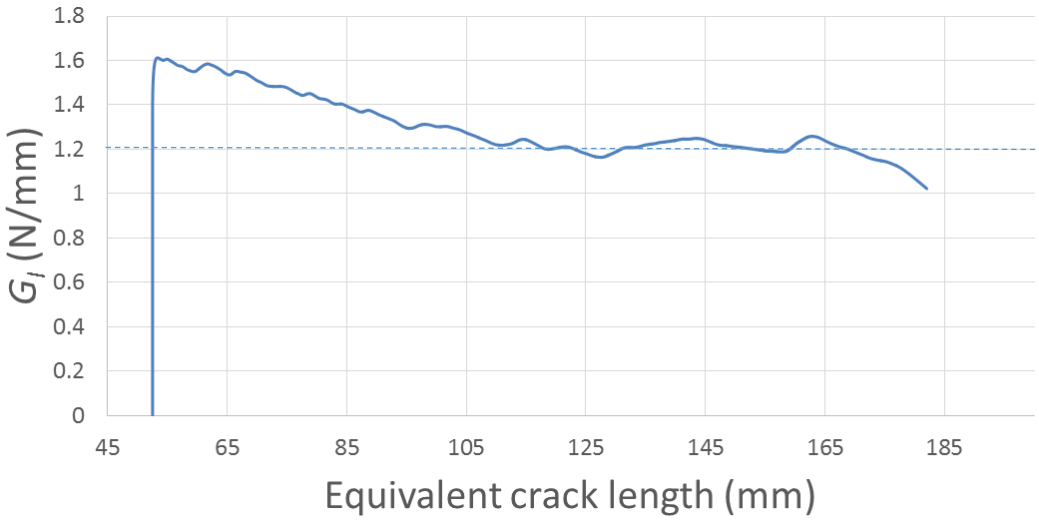

Figure 57: Representative R-Curve of the DCB specimens tested under mode I loading in a 0% RH environment.

Numerical results

The numerical and experimental R-curves (Figure 58) show a good agreement with one another, as both of them tend to the same value. Some irregularities can be seen in the experimental curve, which do not appear in the numerical result. This difference is acceptable as the numerical model considers the existence of a perfect adhesive layer and, therefore, no irregularities are shown in the R-curve.

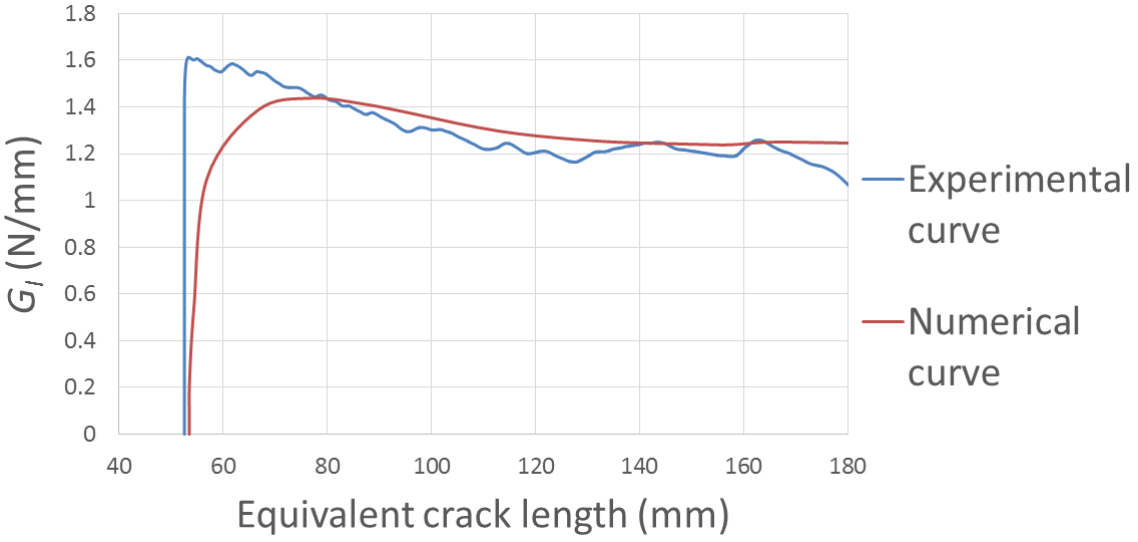

Figure 58: Numerical and experimental R-curves for mode I loading.

5.2.1.2 DCB 0.4mm – 0% RH

The use of the adhesive plates leads to an increase of thickness of the adhesive layer, going from 0.2mm to 0.4mm. As a consequence, it is necessary to compare the critical energy release rate of the ODCB specimens with a standard DCB specimen of equal thickness. After testing, a cohesive failure was observed (Figure 59). A representative load-displacement curve and R-curve are shown in Figure 60 and Figure 61, respectively.

Figure 59: Typical failure surface of the DCB specimens with an adhesive layer of 0.4mm thickness tested under mode I loading in a 0% RH environment.

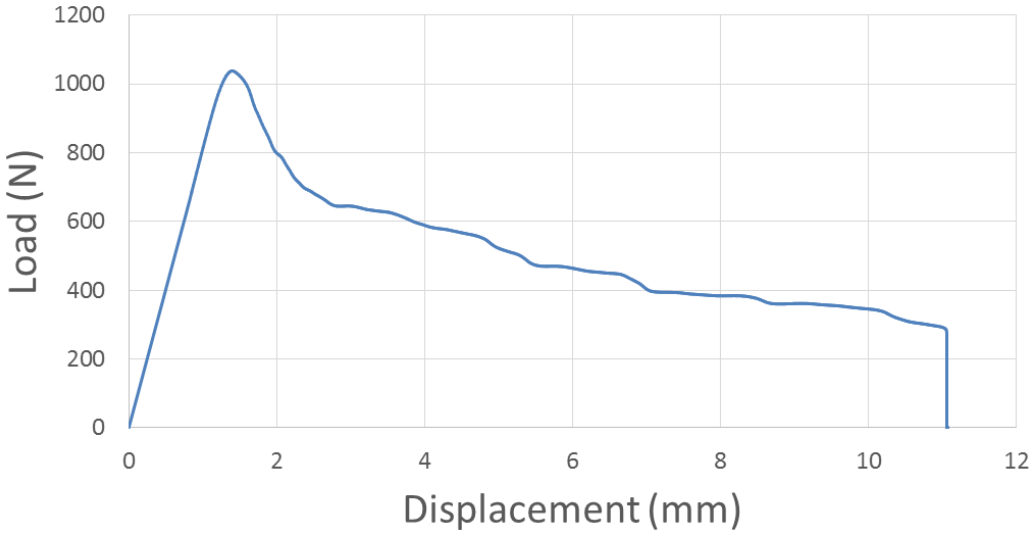

Figure 60: Representative load-displacement curve of the DCB specimens with an adhesive layer of 0.4mm thickness tested under mode I loading in a 0% RH environment.

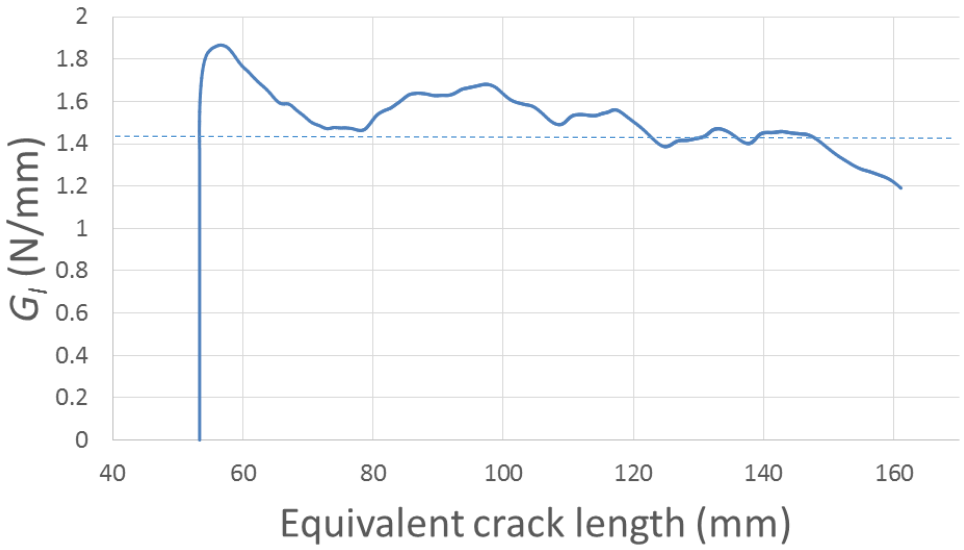

Figure 61: Representative R-curve of the DCB specimens with an adhesive layer of 0.4mm tested under mode I loading in a 0% RH environment.

Numerical results

The comparison between the numerical curve and a representative curve of the experimental tests is shown in Figure 62. The value obtained for the G_{IC} is aproximatly the same in both cases.

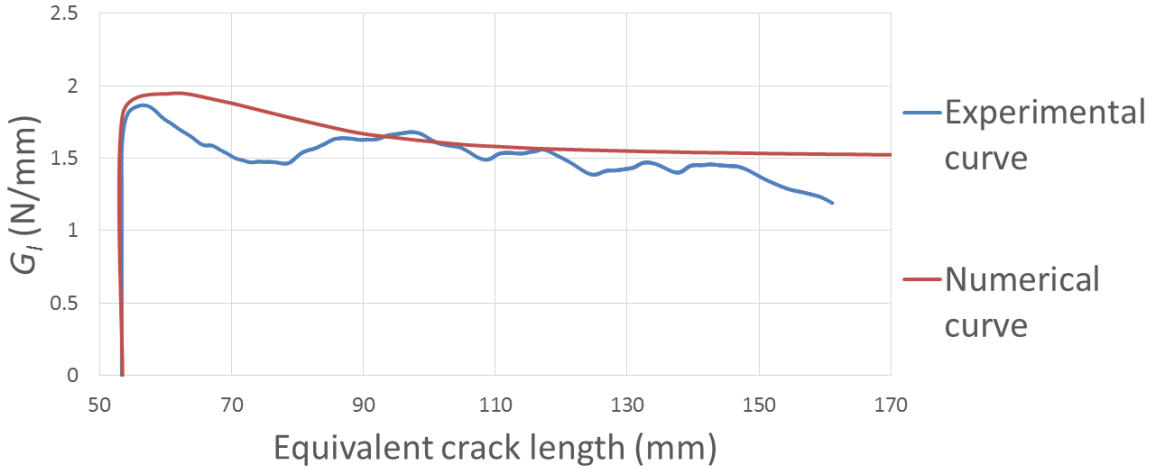

Figure 62: Numerical and experimental R- curves of the DCB specimens with an adhesive layer of 0.4mm thickness tested under mode I loading in a 0% RH environment.

5.2.1.3 ODCB – 0% RH

After testing the standard DCB specimens with a 0.4mm thick adhesive layer, a comparison can be done with ODCB specimens in the same environment. After testing ODCB specimens in a 0% RH environment, a cohesive failure in the adhesive plate was observed (Figure 63).

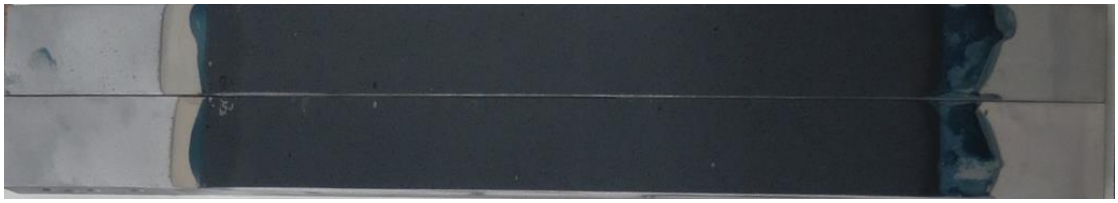

Figure 63: Typical failure surface of an ODCB specimen tested under mode I with a dry adhesive plate.

A typical experimental load-displacement curve is shown in Figure 64. In some tests with ODCB specimens, it is common to find a linear increase in load follows the failure of the primary adhesive. To justify this increase, it is important to remember that the adhesive plate does not cover the whole length of the specimen and there is a zone at the end of the specimen bonded exclusively with the secondary adhesive. The linear increase observed at the end of tests corresponds to the elastic deformation of the secondary bond (Figure 65).

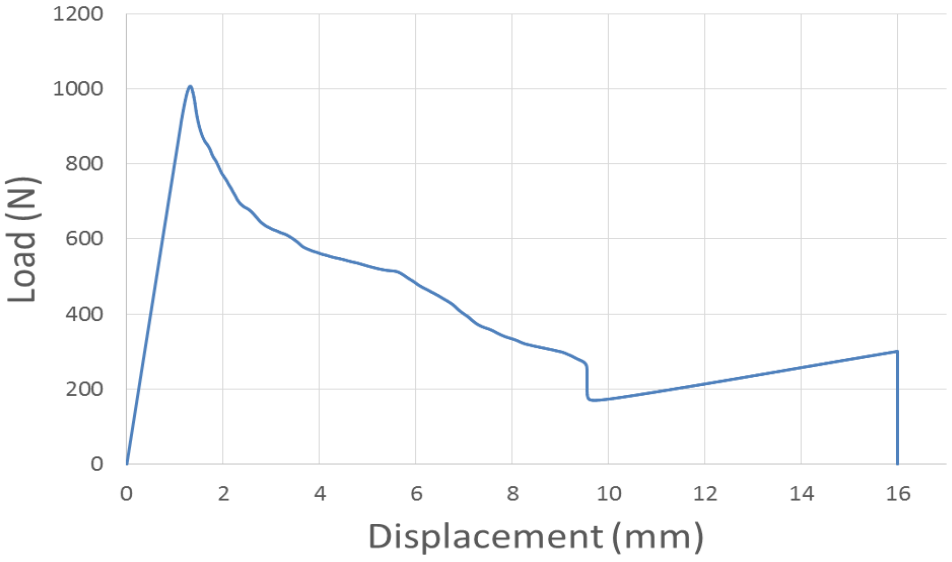

Figure 64: Representative load-displacement curve of the ODCB specimens tested with a dry adhesive plate.

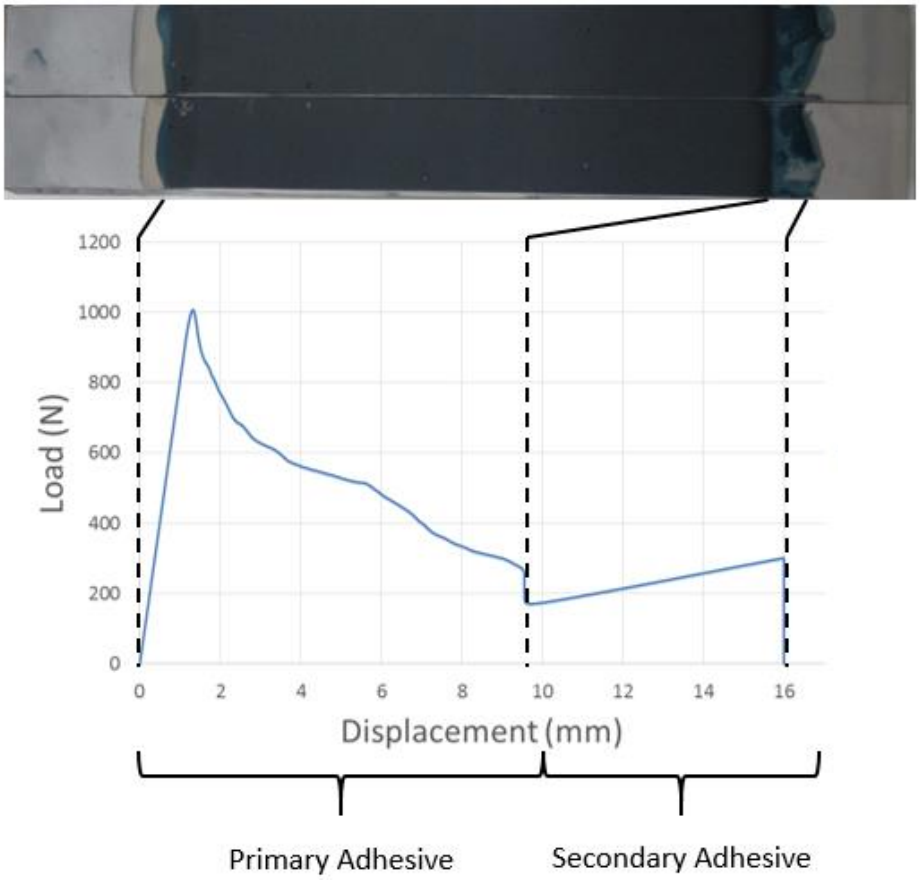

Figure 65: Influence of the excess of secondary adhesive on the load-displacement curve

However, since the objective is to characterize the primary adhesive, the test was stopped and only the first part of the load-displacement curves were used to determine the R-curves (Figure 66). The fact that an approximately constant value of G_I was achieved means that the length of the adhesive plate is long enough to determine the G_{IC}.

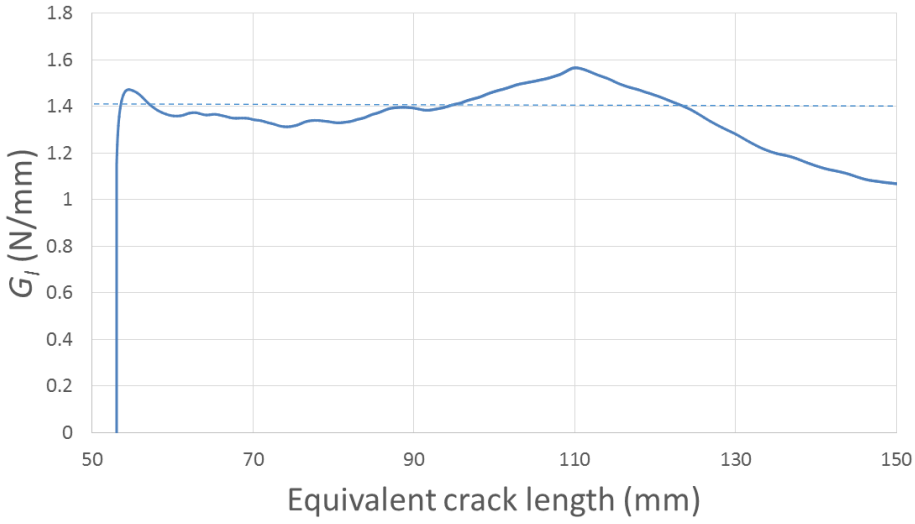

Figure 66: Representative R-curve of the ODCB specimens tested with a dry adhesive plate.

Numerical results

In both numerical models, with either 1 or 3 layers of cohesive elements, it can be seen that there is an agreement between the experimental and numerical results regarding the critical energy release rate (Figure 67). In the model it was considered that the adhesive plate would cover the whole specimen, which is not true. However, since there is an agreement between the experimental and numerical results, it can be concluded that the adhesive plate is long enough to reach a constant crack propagation.

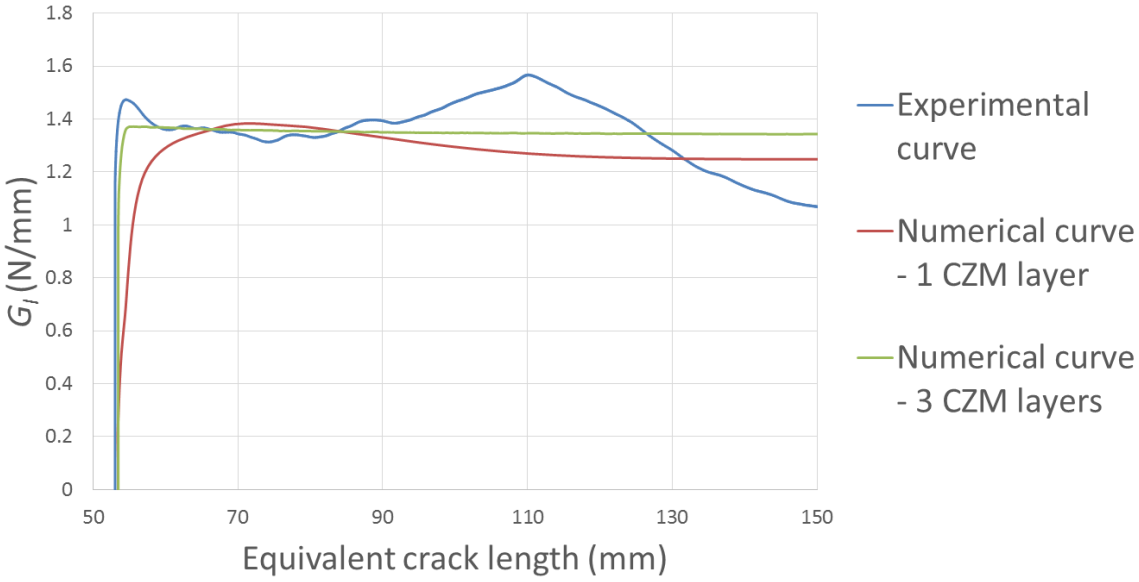

Figure 67: Numerical and experimental R-curves of the ODCB specimens tested under mode I with a dry adhesive plate.

According to the same numerical simulation, there is no degradation of the secondary bond (Figure 68). This result suggests that the inclusion of the secondary adhesive does not influence the fracture toughness determined experimentally.

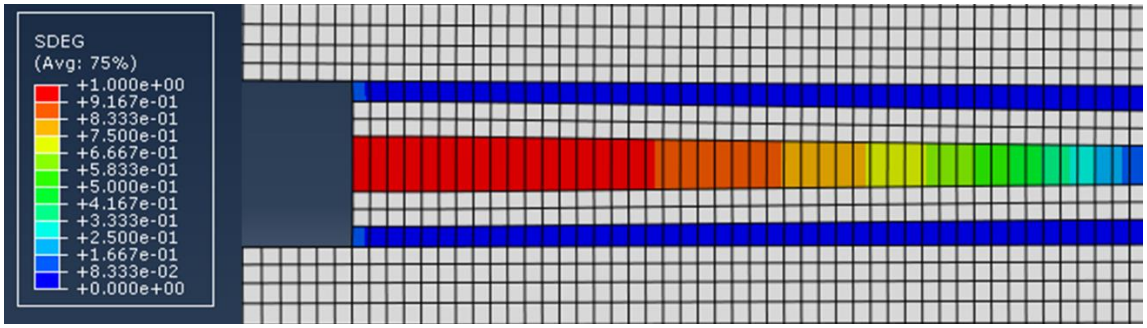

Figure 68: Degradation of the primary and secondary bonds for the ODCB specimens tested under mode I with a dry adhesive plate.

5.2.1.4 *Validation of the ODCB specimens*

The curve obtained for the DCB with a 0.2mm thick adhesive layer will be the reference. It can be seen a slight change in the maximum load when the thickness is increased to 0.4mm. However, the results obtained for the DCB with 0.4mm thick adhesive layer and for the ODCB specimen tested in a 0% RH are in agreement with each other, suggesting that the introduction of a secondary bond does not affect the properties obtained (Figure 69).

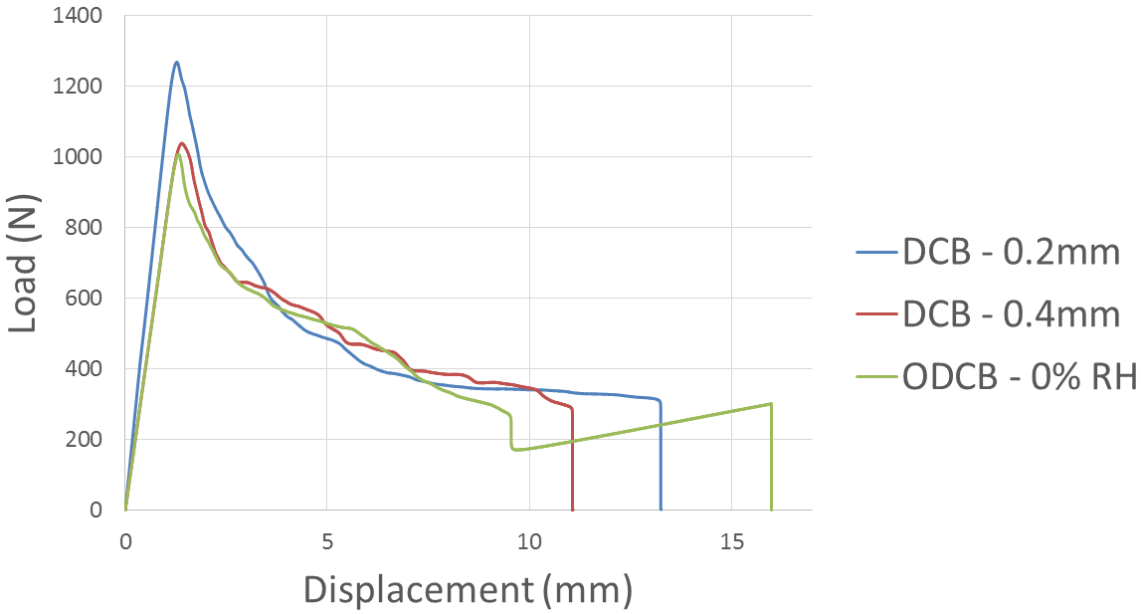

Figure 69: Load-displacement curves of the 3 types of specimens used to validate the influence of the adhesive's thickness and of the secondary bond.

Analysing the R-curves, slight increase of G_{IC} is observed when the thickness of the adhesive increases, but no difference is seen with the inclusion of the secondary bond (Figure 70). This result is also supported with the numerical analysis shown in Figure 68, where no degradation of the secondary bonding was observed.

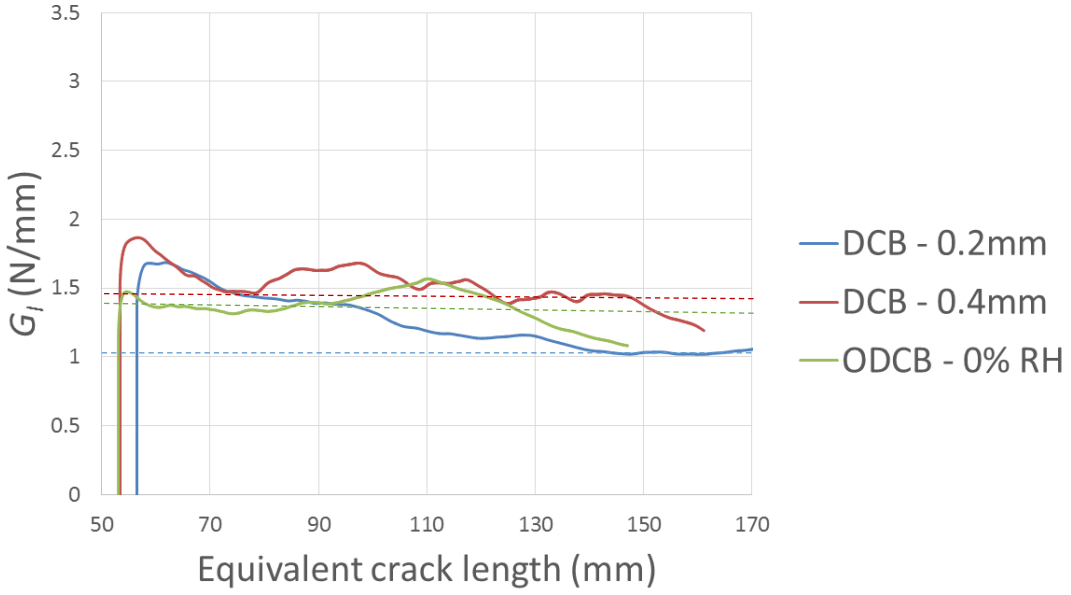

Figure 70: R-curves of the 3 types of specimens used to validate the influence of the adhesive's thickness and of the secondary bond.

As a result, the increase of the adhesive layer's thickness lead to an overestimation of the fracture toughness in 0.2 N/mm. The inclusion of the secondary bond did not have an influence.

Validation of the ODCB specimens for other loading modes

No further experimental tests were done to validate the use of ODCB specimens under other loading modes. To compensate for this fact, the influence of this method was studied numerically and the results have shown that the secondary bonds should not influence the fracture toughness measured under mixed-mode 55° and mixed-mode 87°. This conclusion is based on 2 results: the inexistence of degradation in the secondary bonds (Figure 71 and Figure 72) and the equal fracture toughness obtained in the R-curves (Figure 73 and Figure 74).

Regarding the degradation of the secondary bonds, only two partially degraded points can be seen at the crack tip. However, this corresponds to a much reduced length of adhesive that does not compromise the results obtained.

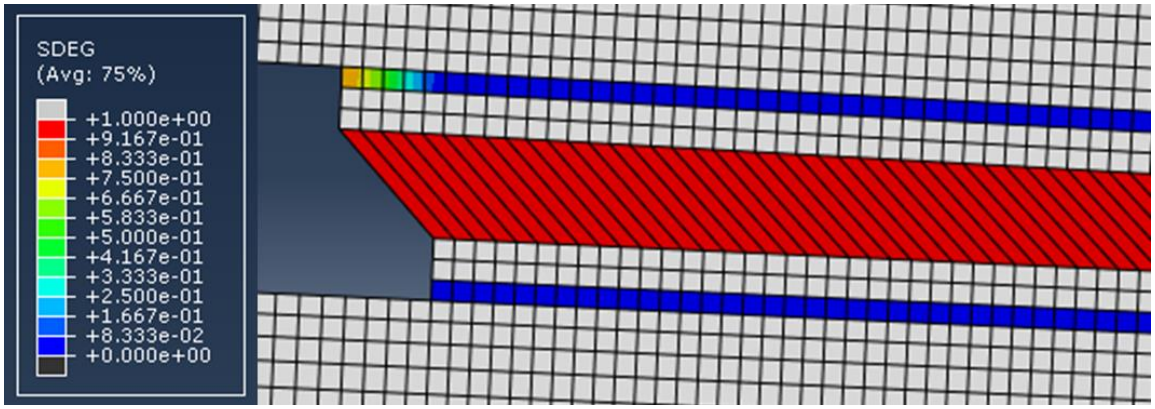

Figure 71: Degradation of the primary and secondary bonds for the ODCB specimens tested under mixed-mode 55° with a dry adhesive plate.

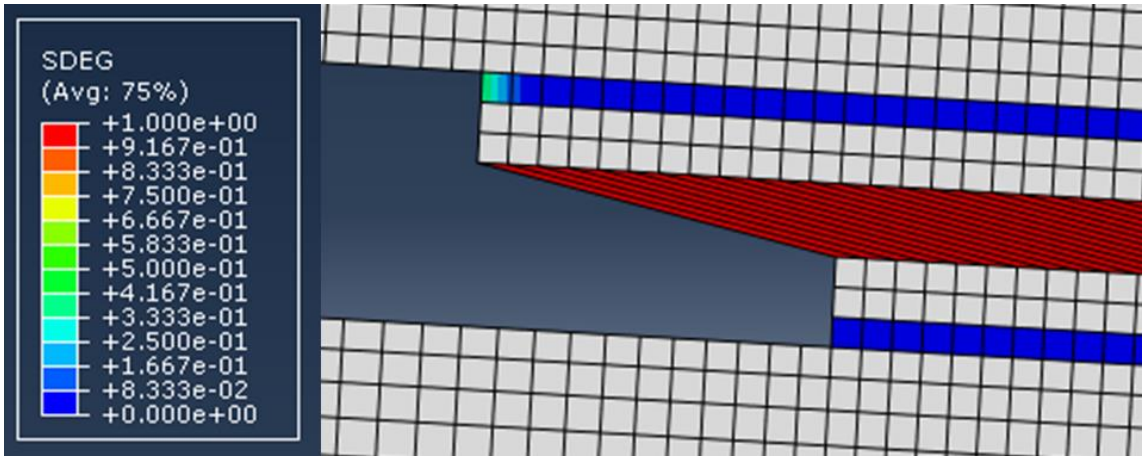

Figure 72: Degradation of the primary and secondary bonds for the ODCB specimens tested under mixed-mode 87° with a dry adhesive plate.

On the other hand, the R-curves obtained show equivalent results to what was obtained experimentally for mode I. It can be seen that the increase of the adhesive layer's thickness changes the fracture toughness, while the inclusion of the secondary bond does not influence the result. The numerical simulations using only 1 or 3 CZM layers reported the same fracture

toughness in both mixed-modes. For this reason, and in order to make the graphics more readable, only the latter is shown.

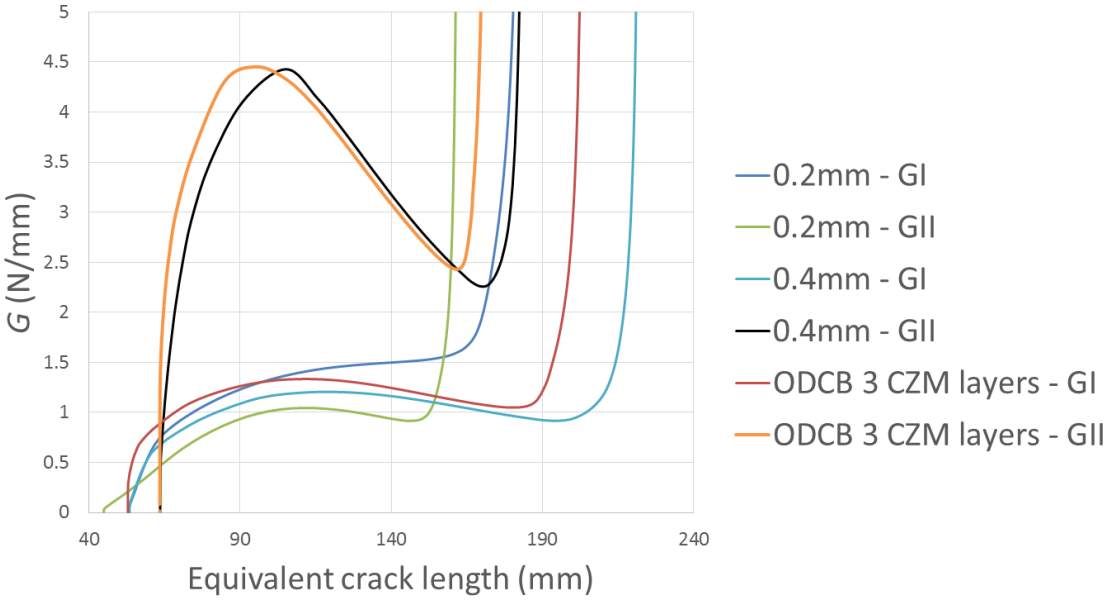

Figure 73: Numerical R-curves for the DCB and ODCB specimens tested under mixed-mode 55°.

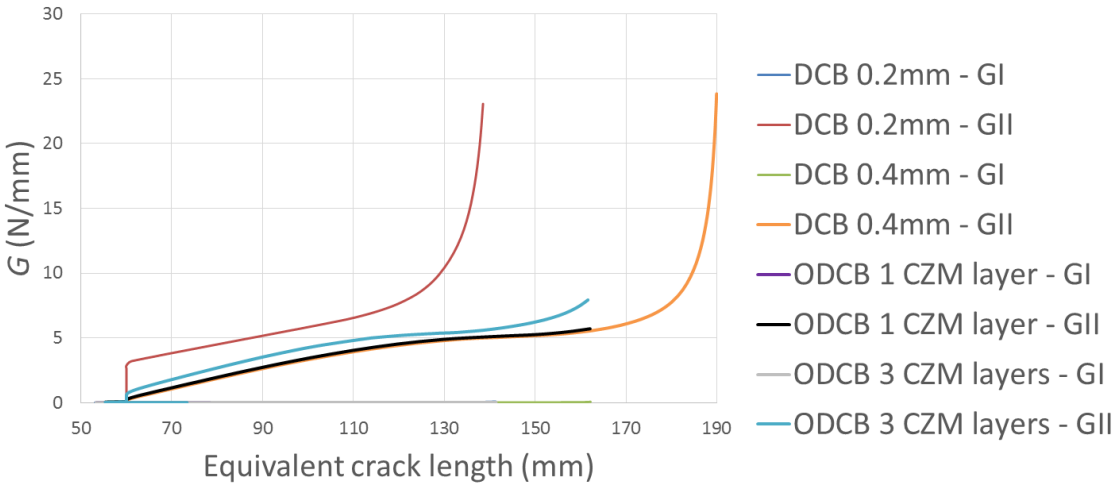

Figure 74: Numerical R-curves for the specimens tested under mixed-mode 87°.

5.2.1.5 ODCB – 75% RH

In this test, a cohesive failure in the adhesive plate was obtained (Figure 75). Similarly to the previous case, the load-displacement curve reveals a linear increase after the rupture of the primary adhesive (Figure 76), which has already been justified. The R-curve obtained is shown in Figure 77.

Figure 75: Typical failure surface of the ODCB specimens tested under mode I with an adhesive plate aged in a 75% RH environment.

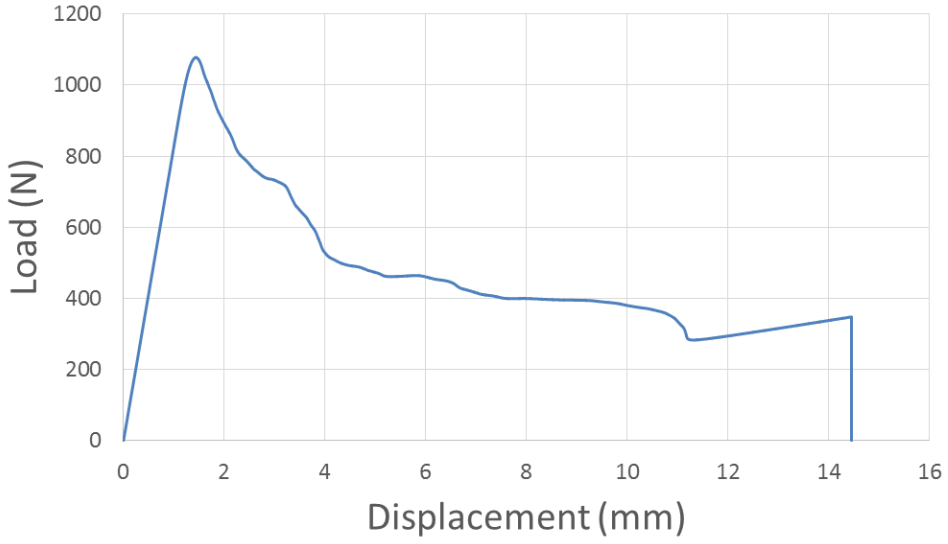

Figure 76: Representative load-displacement curve of the ODCB specimens tested under mode I with an adhesive plate aged in a 75% RH environment.

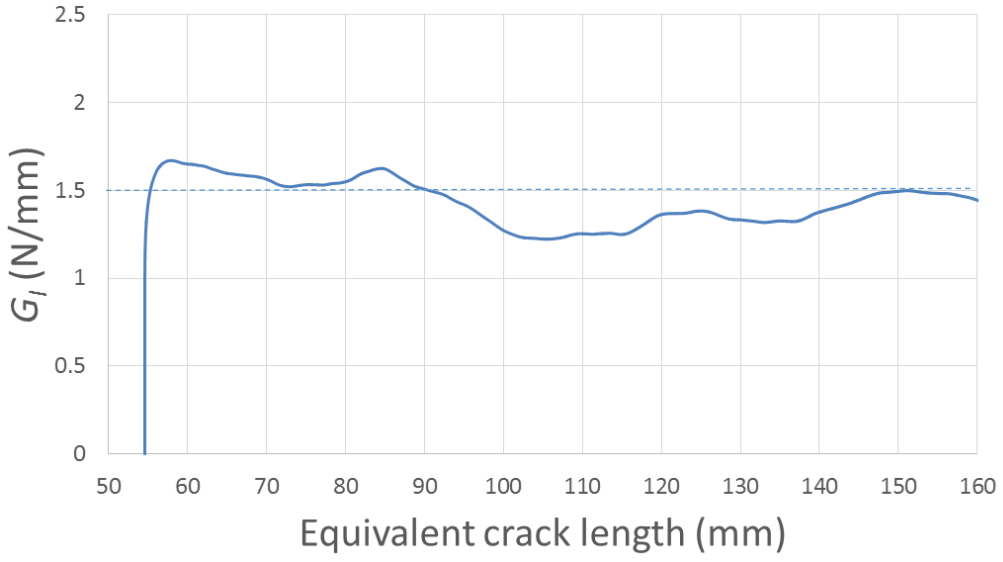

Figure 77: Representative R-curve of the ODCB specimens tested under mode I with an adhesive plate aged in a 75% RH environment.

5.2.1.6 DCB – 100% RH

In the cases of the adhesive plates aged in distilled water (100% RH), cohesive failure surfaces were observed. However, in this environment, the failure occurred closed to the interface between the adhesive plate and the secondary bond (Figure 78).

Figure 78: Typical failure surfaces of the ODCB specimens tested under mode I with an adhesive plate aged in a 100% RH environment.

Unlike the previous cases analysed, there was no load increase after the rupture of the adhesive (Figure 79). This can be explained with the swelling of the primary bond, making the adhesive plate longer and capable of covering a larger length of the adherend. As a consequence, the excess of adhesive is minor. Furthermore, the secondary adhesive used in this environment has mechanical properties more similar to the primary bond, making it unlikely that such small excess of secondary bond would avoid the complete rupture of the specimen. Given these conditions, the whole load-displacement curves were analysed, leading to the representative result shown in Figure 80.

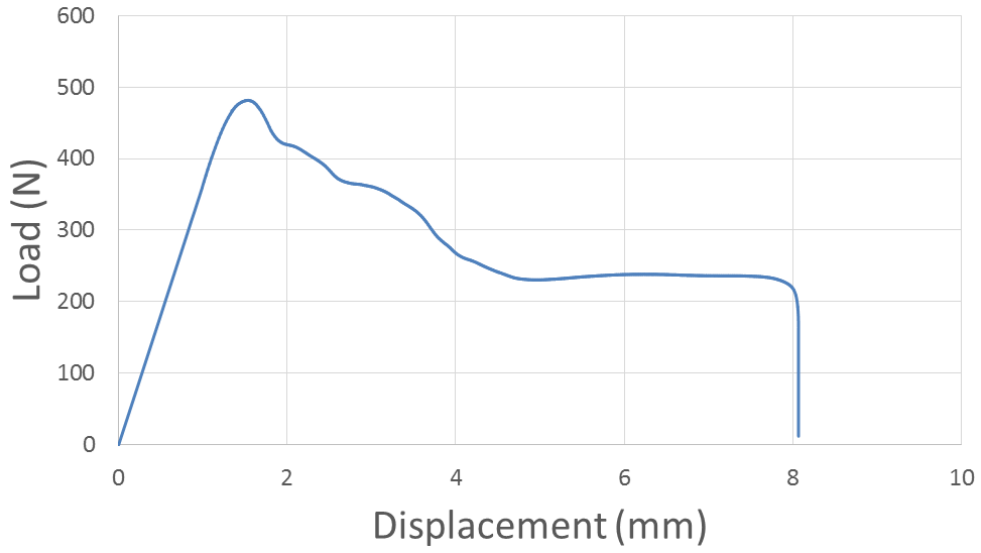

Figure 79: Representative load-displacement curve of the ODCB specimens tested under mode I loading with an adhesive plate degraded in a 100% RH environment.

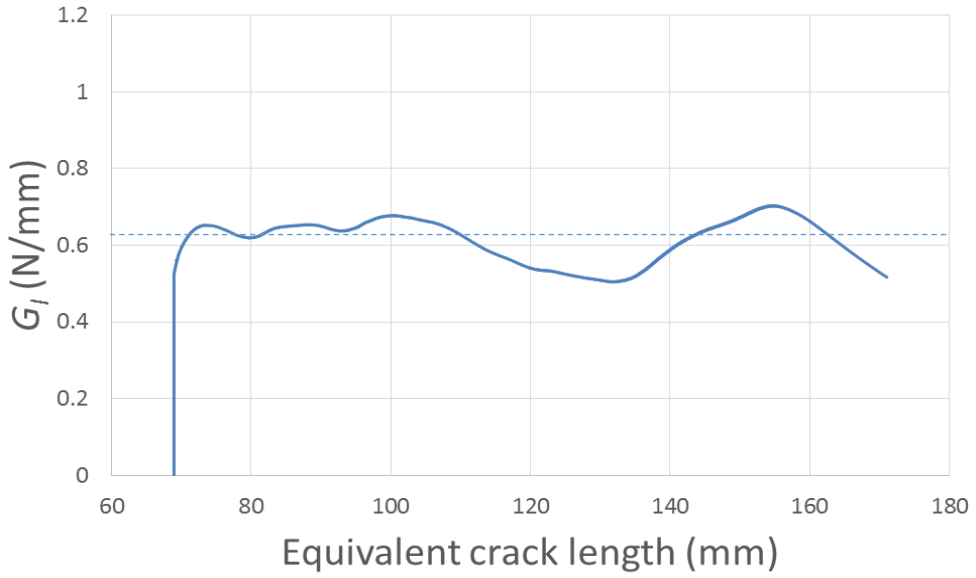

Figure 80: Representative R-Curve of the ODCB specimens tested under mode I loading with an adhesive plate aged in a 100% RH environment.

5.2.1.7 Comparison of the results for mode I loading

Using a representative curve of each test done under mode I loading, it is possible to compare the two types of specimens used, as well as studying the influence of water on the adhesive.

It can be seen that the ageing environments do influence the behaviour of the adhesive. The 100% RH environments causes degradation of the adhesive, which can be seen in both load-displacement curves (Figure 81) and R-curves (Figure 82). On the other hand, 75% RH environment does not seem to influence the load-displacement curve. However, it is important to note that the compliance of this curve is different from the one obtained in the dry environment. As a result, the fracture toughness is different despite the similarities in the load-displacement curves for both 0% and 75% RH environments.

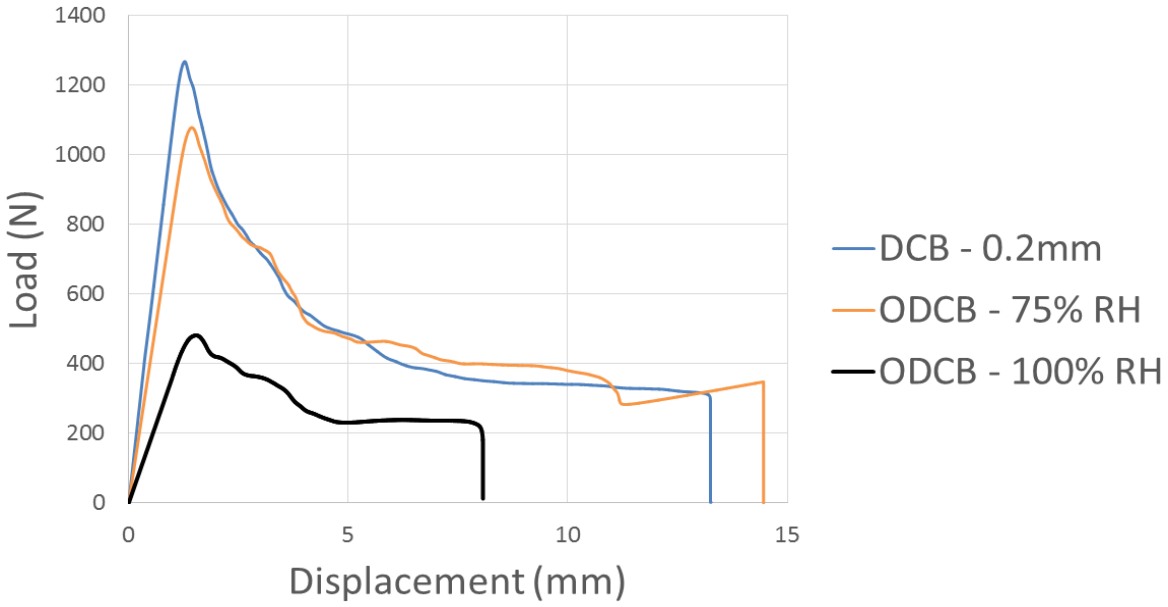

Figure 81: Load-displacement curves of the tests done under mode I.

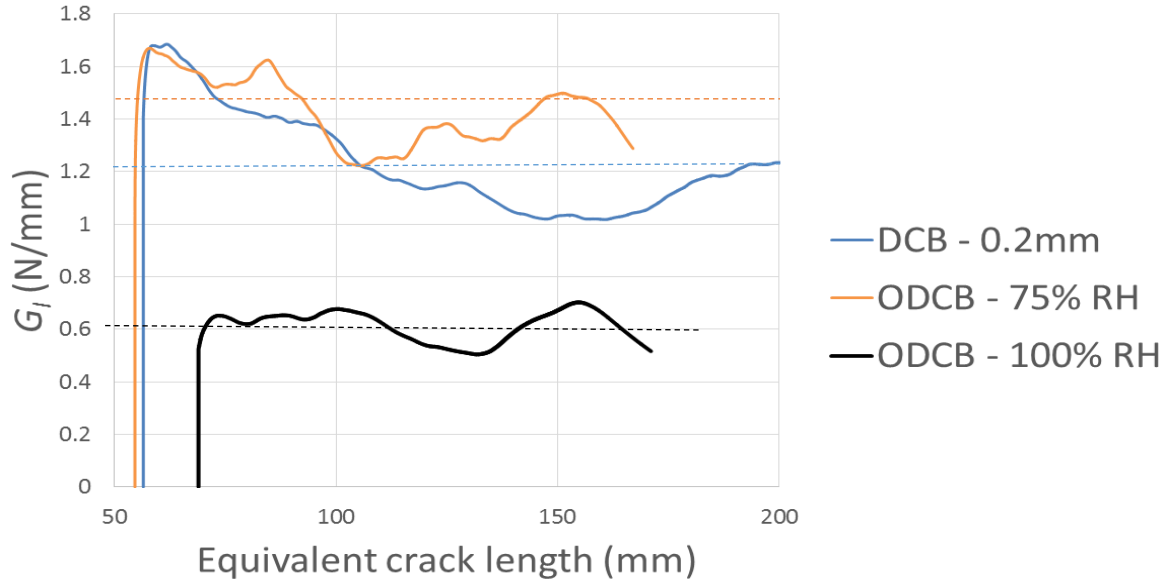

Figure 82: R-curves of the tests done under mode I.

Table 13: G_{IC} obtained for the 0%, 75% and 100% RH environments.

Specimen	Environment	G_{IC} (N/mm)
DCB	0% RH	1.15
ODCB	75% RH	1.6
	100% RH	0.6

In the literature, it was predicted that the fracture toughness of the adhesive SikaPower®-4720 aged in distilled water would be equal to 0.6 N/mm [43].The fracture toughness determined with the ODCB specimen in a 100% RH environment is in agreement with the prediction made.

5.2.2 Mixed-mode 55°

5.2.2.1 DCB – 0% RH

Under the mixed-mode 55° loading, a cohesive failure was observed (Figure 83). It is important to note that in this loading mode the crack only propagates until mid-length of the specimen. To check the failure surface, it is necessary to open the specimen using a mode I loading. Given this condition, the type of failure surface is determined analysing exclusively the first half of the adhesive layer. The same condition is applied to the mixed-mode 87° loading and ENF test.

Figure 83: Typical failure surfaces of the DCB specimens tested under mixed-mode 55° loading in a 0% RH environment.

Analysing the load-displacement cures (Figure 84), it can be seen that the load decreased throughout a certain displacement (0.1mm to 0.2mm). This suggests that the crack propagation was stable.

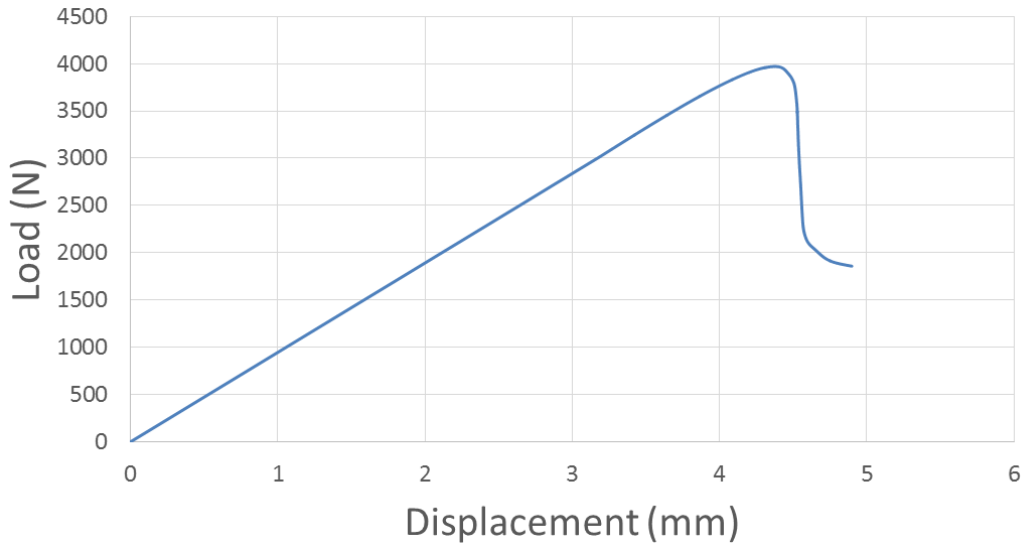

Figure 84: Representative load-displacement curve of the DCB specimens tested under mixed-mode 55° loading in a 0% RH environment.

The three R-curves obtained (Figure 85) prove that the crack propagation was stable, as the value of the fracture toughness reached a plateau before failure. Had an unstable crack propagation occurred, the R-curve would stop without reaching a constant value.

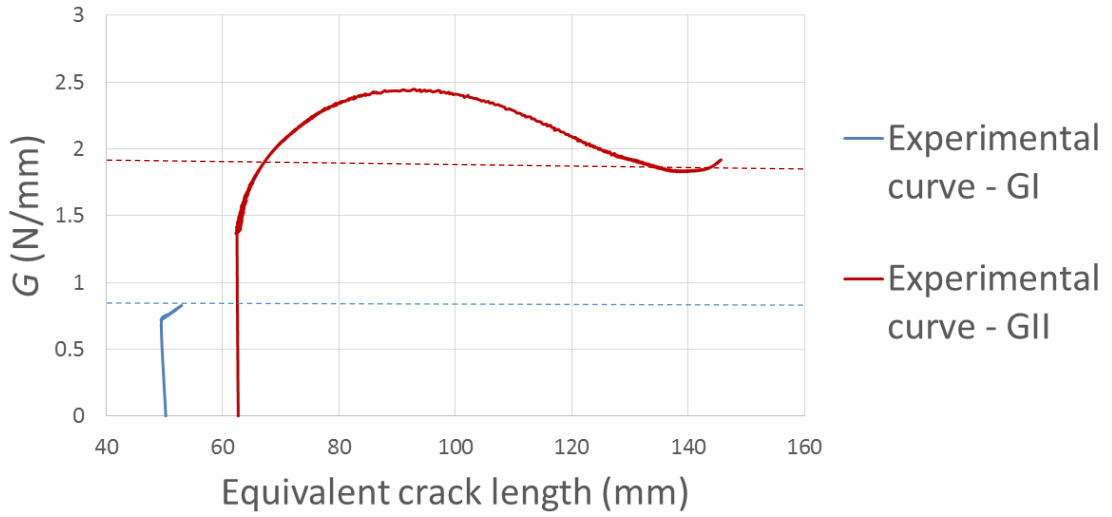

Figure 85: Representative R- curve of the DCB specimens tested under mixed-mode 55° loading in a dry environment.

Numerical Results

The critical energy release rates were determined by the value the plateau reached in the R-curve. Since the simulation considers a stable crack propagation, a good agreement was found between experimental and numerical results (Figure 86).

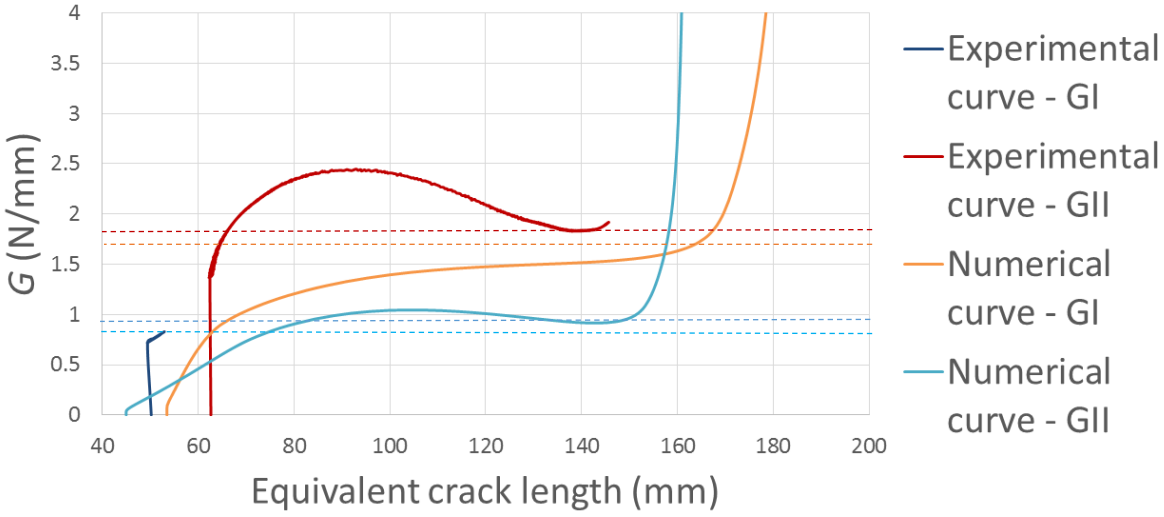

Figure 86: Numerical and experimental R-curves for the DCB specimens tested under mixed-mode 55° in a dry environment.

5.2.3 Mixed-mode 87°

5.2.3.1 DCB – 0% RH

The failure surface shows a cohesive failure in the adhesive (Figure 87).

Figure 87: Typical failure surfaces of the DCB specimens tested under mixed-mode 87° in a 0% RH environment.

The load-displacement curves (Figure 88) show a significant similarity to the load-displacement curve usually obtained in the ENF test. This is to be expected as the loading mode is almost identical to a pure mode II load. The same reason justifies why the mode I component of the R-curves (Figure 89) is almost null.

Unlike the previous case, the crack propagation was unstable, which can be proved with the sudden drop in load of the load-displacement curve. As a consequence, the R-curve does not reach a plateau (Figure 89). In this scenario, the critical energy release rate was considered to be the highest value reached.

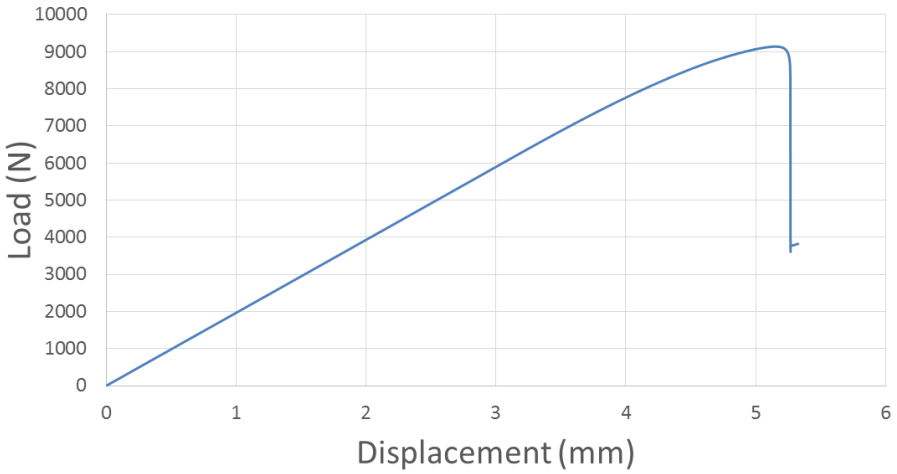

Figure 88: Representative load-displacement curves of the DCB specimens tested under mixed-mode 87° in a 0% RH environment.

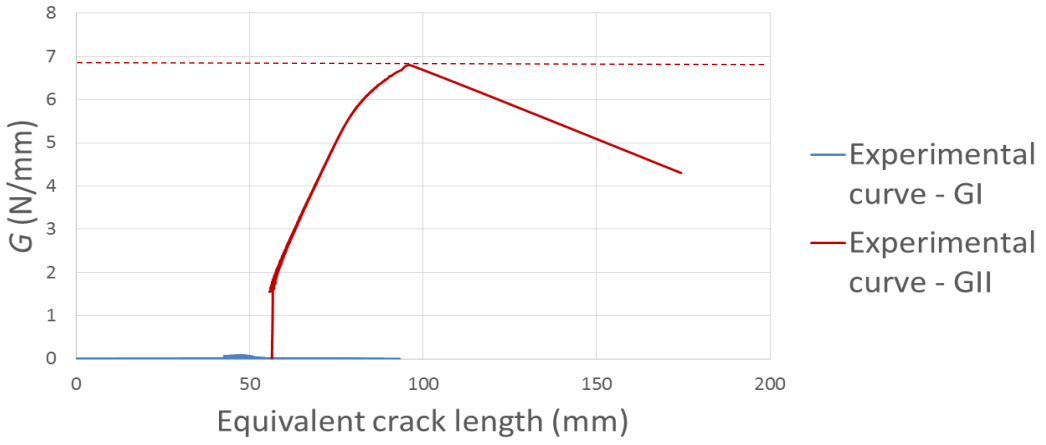

Figure 89: Representative R-curve of the DCB specimens tested under mixed-mode 87° in a 0% RH environment.

Numerical results

The value of G_{IIC} obtained from this experimental tests is higher than the value obtained from the ENF test (Figure 90). In normal conditions, this situation should never happen as the mode II critical energy release rate of a mixed-mode loading must be lower than the critical energy release rate of a pure mode II loading. However, the numerical analysis confirms this increase, which must be caused by the influence of the apparatus used to create the mixed-mode loading.

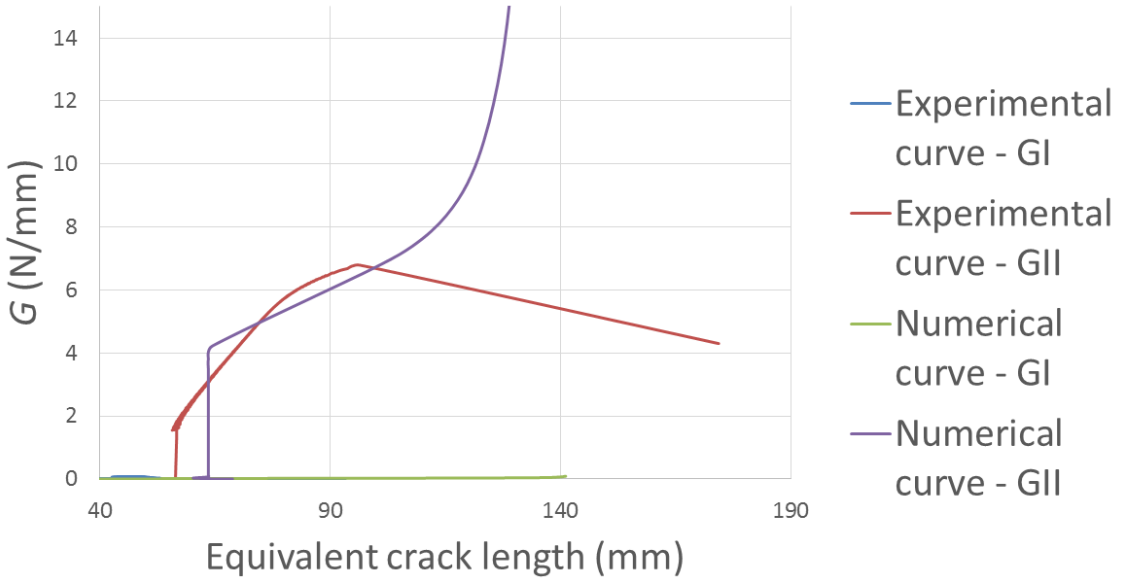

Figure 90: Numerical and experimental R-curves for the DCB specimens tested under mixed-mode 87° in a dry environment.

5.2.4 Mode II

5.2.4.1 DCB – 0% RH

ENF tests were done to determine the value of G_{IIC} and allow the possibility of modelling all the tests done in this work.

After testing and opening the specimens, a cohesive failure on the adhesive could be observed (Figure 91). The load-displacement curve (Figure 92) shows a clearly stable crack propagation. As a result, a constant value was reached in the R-curve (Figure 93).

Figure 91: Typical failure surface of the DCB specimens tested under mode II in a 0% RH environment.

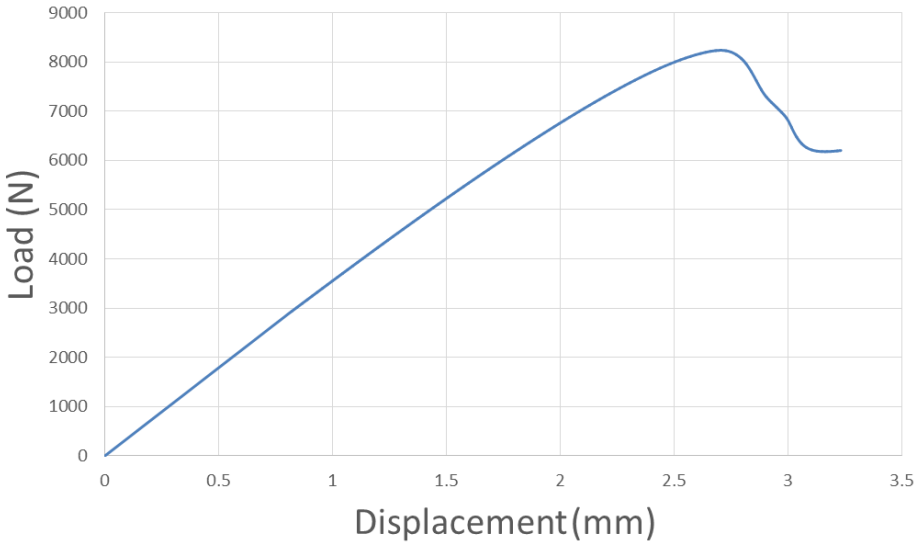

Figure 92: Representative load-displacement curve of the DCB specimens tested under mode II in a dry environment.

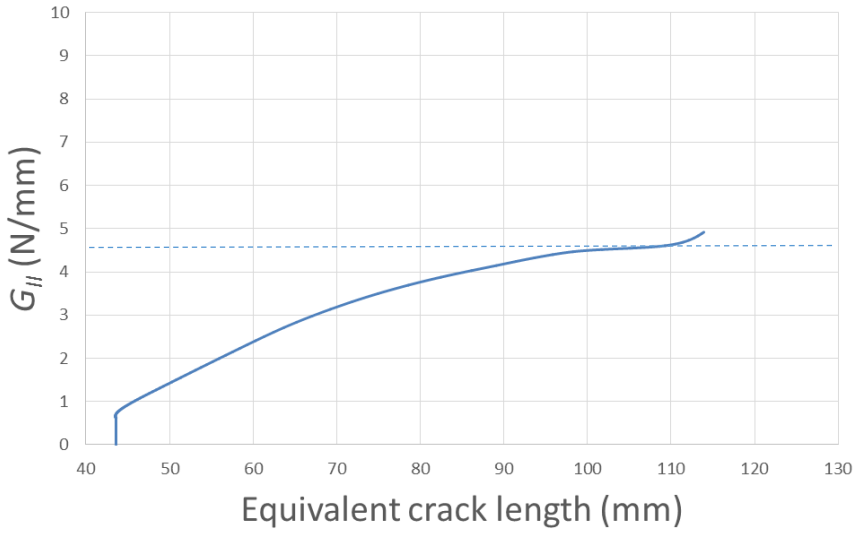

Figure 93: Representative R-curve of the DCB specimens tested under mode II in a dry environment.

5.2.5 Fracture envelopes

With the results from the experimental tests (Table 14) it was possible to define the fracture envelopes for the three environments studied (Figure 94).

Table 14: Summary of the fracture toughness for the different loading modes as a function of the relative humidity.

		Mode I	Mixed-mode 55°		Mixed-mode 87°		Mode II
Specimen	Environment	G_{IC} (N/mm)	G_I (N/mm)	G_{II} (N/mm)	G_I (N/mm)	G_{II} (N/mm)	G_{IIC} (N/mm)
DCB	0% RH	1.15	0.82	1.69	0.04	6.61	4.55
ODCB	75% RH	1.7	1.48	0.73	0.02	7.02	-
	100% RH	0.57	0.5	0.37	0.22	0.83	-

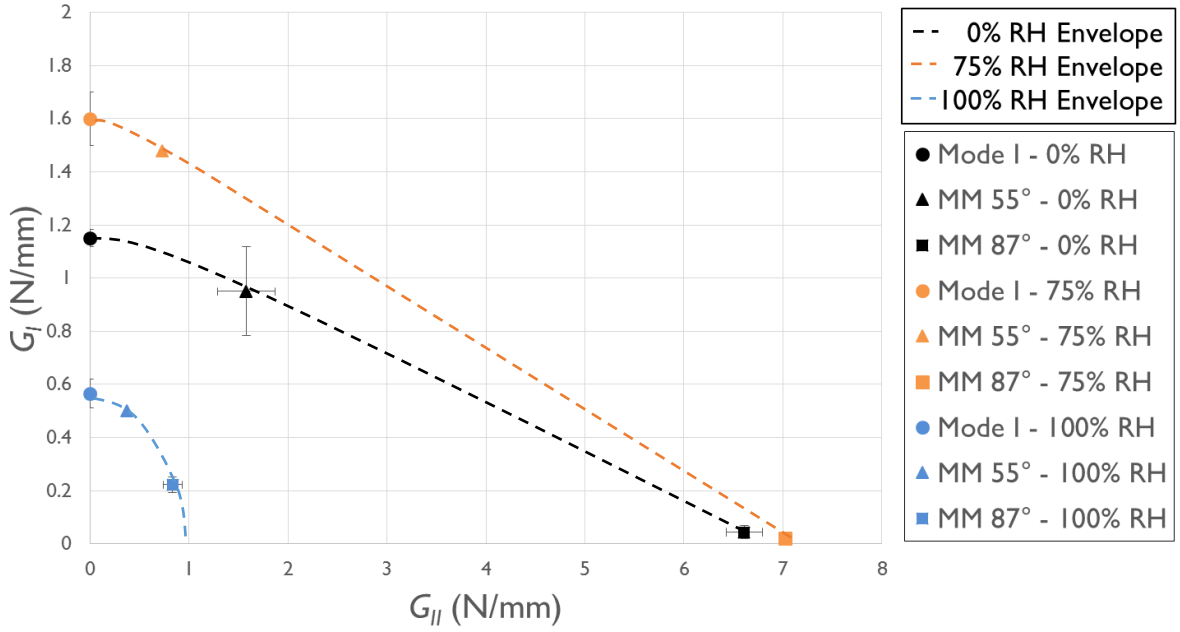

Figure 94: Fracture envelopes of the specimens tested in a 0%, 75% and 100% RH environments.

0% RH

In this envelope, the difference between the values of G_{II} obtained for the ENF and mixed-mode 87° tests stands out. It was expected that the mode II component of the fracture toughness measured in the mixed-mode 55° test would be lower than the one measured in the ENF test, as the mixed-mode test introduces an opening load. However, the experimental results show otherwise. It is relevant to point out that these two tests were done using different equipment, with distinct rigidities, which may help explain the difference in the values obtained.

Ignoring the data obtained with the ENF test, the fracture envelope for the dry environment can be described with a linear function.

75% RH

The fracture envelope for the 75% RH environment, only 1 valid result has been obtained for the mixed-mode 55° and mixed-mode 87° test. For this reason, it is difficult to take valid conclusions from these results. However, similarly to the results of the dry environment, it seems possible to describe this envelope with a linear function. Also, an increase in the fracture toughness can be observed in comparison with the envelope determined in a dry environment.

100% RH

Unlike previous results, the shape of the fracture envelope determined in the 100% RH environment can be approximated with a quadratic function. It can also be seen that the fracture toughness was reduced when compared to the 0% RH environment.

5.2.6 Influence of water on the fracture envelope

Analysing the three fracture envelopes and considering the 0% RH environment as a reference, two changes can be identified (Figure 95). The first one is the change to the 100% RH environment, where the fracture toughness of the adhesive is reduced in all loading modes. This behaviour can be justified with the degradation of the adhesive. The second one is the increase of the fracture toughness in the 75% RH environment. Such change is justified by the plasticization of the adhesive.

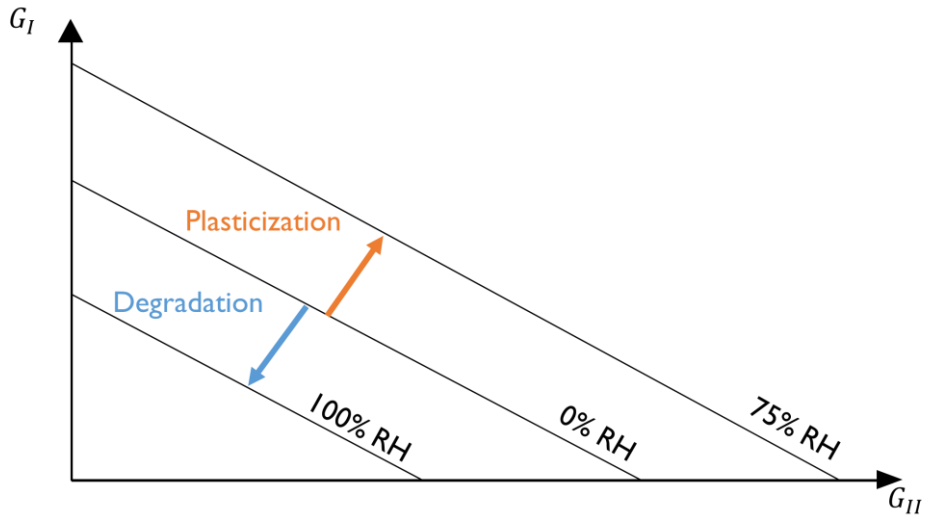

Figure 95: Schematic representation of the three envelopes and their interactions.

In both scenarios, the changes observed can be justified with the adhesive's water mass uptake in each environment (previously mentioned in Table 6), as well as the influence of the ageing environment on the T_g (Figure 96), which has been reported in the literature [40].

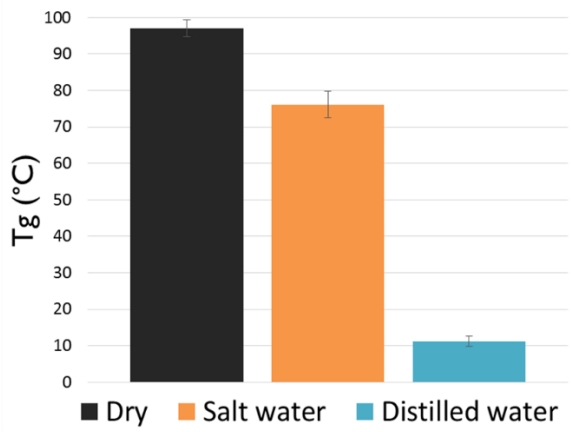

Figure 96: Glass transition temperature of SikaPower®-4720 as a function of the ageing environment [40].

Starting with the 100% RH environment, the degradation that occurs can easily be justified with the reduction of the T_g to a point below room temperature. As a consequence, any test done above 10 °C will prove a reduction in properties. Furthermore, the adhesive's mass uptake is equal to 35%, which leads to a huge concentration of water within the adhesive and explains why the properties were reduced so significantly within 4 days.

In the 75% RH environment, the increase of fracture toughness can be explained as the result of the interaction between two opposite factors. On one side, the water absorbed causes a slight degradation, which can be seen in the form of a reduction of T_g. However, the degradation that occurs is not enough to overcome the increase of ductility caused by the plasticization of the adhesive. This explanation becomes more acceptable once it is taken into account that in this environment the mass uptake is approximately 6 times lower (6.5%) than in the 100% RH environment.

6 Conclusions

The main objectives of this work were the characterization of the three fracture envelopes under 0%, 75% and 100% RH as well as determining the relation between them. The fracture envelope in a dry environment has been fully characterized. However, more tests need to be done to define the fracture toughness of the adhesive in the other two environments.

Nonetheless, it was possible to identify a trend between the three envelopes, where the 100% RH environment causes degradation of the mechanical properties and the 75% RH environment leads to a higher fracture toughness due to plasticization of the adhesive.

To determine the fracture toughness in the 75% and 100% RH environments, a modified specimen was used, allowing the adhesive to saturate in just 4 days. The analysis done in mode I shows that due to an increase of the adhesive layer's thickness, the fracture toughness is overestimated in approximately 0.2 N/mm. This increase is justified with the change of the FPZ's shape as well as the modification of the stress distribution in the adhesive. The inclusion of the secondary bond has proven to have no effect on the fracture toughness measured.

The numerical simulations developed in this research suggest that the validation of the ODCB specimens done for mode I can be extrapolated to other loading modes

A final validation of the new method adopted still needs to be done. Once the standard DCB specimens manufactured in this thesis reach saturation and are tested, the values of the fracture toughness should be compared with the ones reported in this work.

7 Future work

Besides the final validation mentioned previously some suggestions are made to continue the work developed in this thesis:

- Reproducing the validation of the ODCB specimens for other loading modes. The idea is to determine if the overestimation in fracture toughness observed for mode I is constant in other loading modes. If not, it is relevant to determine what the difference is.
- Reproducing the tests done in other ageing environments. It has been concluded that in one of the ageing environments there is degradation and in the other there is plasticization. By utilizing different saturated salt solutions it could be possible to identify a transitory environment, where the degradation caused by the water uptake is equal to the increase of ductility caused by plasticization. In this transitory environment, the fracture toughness should be equal to the one determined in the 0% RH environment.
- Determining the influence of the time of exposure on the fracture envelope. The application of ODCB specimens allow the saturation process to be finished within 4 days. This opens the possibility to do several tests, in the same environment, where the adhesive plates are aged for different periods. This would reveal if, for instance, the increase of ductility observed in the 75% RH environment is constant and, in case it is not, when does degradation start to occur.
- Including more mixed-mode tests. This would lead to a more defined fracture envelope.
- Using ODCB specimens to determine the influence of water uptake on the fatigue behavior of an adhesive joint. Similarly to this work, it is possible to apply the same specimens in order to determine how the water content in the adhesive affects its fatigue resistance.

References

[1] L.F.M. da Silva and C. Sato, *Design of Adhesive Joints Under Humid Conditions*: Springer, 2013.

[2] L.F.M. da Silva, A. Öchsner, and R. D. Adams, *Handbook of Adhesion Technology*: Springer-Verlag, 2011.

[3] L.F.M. da Silva, A.G. de Magalhães, and M. F. S. F. d. Moura, *Juntas adesivas estruturais*. Porto: Publindústria, Edições Técnicas, 2007.

[4] M.J. Davis and A. McGregor, "Assessing adhesive bond failures: mixed-mode bond failures explained," in *ISASI Australian Safety Seminar, Canberra*, 2010.

[5] D.O. Adams, K.L. DeVries, and C. Child, "Durability of Adhesively Bonded Joints for Aircraft Strutures," *Department of Mechanical Engineering, University of Utah*.

[6] X. Han, A. D. Crocombe, S. N. R. Anwar, P. Hu, and W. D. Li, "The Effect of a Hot-Wet Environment on Adhesively Bonded Joints Under a Sustained Load," *Journal of Adhesion,* vol. 90, pp. 420-436, 2014.

[7] F.J.P. Chaves, L.F.M. da Silva, M.F.S.F. de Moura, and D.A. Dillard, "Fracture mechanics tests in adhesively bonded joints: a literature review," *The Journal of Adhesion,* vol. 90, pp. 955-992, 2014.

[8] M.D. Banea and L. F. M. d. Silva, "Adhesively bonded joints in composite materials: an overview," *Proceedings of the Institution of Mechanical Engineers Part L-Journal of Materials-Design and Applications,* vol. 223, pp. 1-18, 2009.

[9] M. D. Banea, "High Temperature Adhesives for Aerospace Applications," Doctor of Philosophy, Departamento de Engenharia Mecânica, Faculdade de Engenharia da Universidade do Porto, Porto, 2011.

[10] F. J. P. Chaves, M. F. S. F. de Moura, L. F. M. da Silva, and D. A. Dillard, "Numerical validation of a crack equivalent method for mixed-mode I plus II fracture characterization of bonded joints," *Engineering Fracture Mechanics,* vol. 107, pp. 38-47, 2013.

[11] F. J. P. Chaves, "Fracture Mechanics Applied to the Design of Adhesively Bonded Joints," Doctor of Philosophy, Departamento de Engenharia Mecânica, Faculdade de Engenharia da Universidade do Porto, Porto, 2013.

[12] M.F.S.F. de Moura, R. D. S. G. Campilho, and J. P. M. Gonçalves, "Crack equivalent concept applied to the fracture characterization of bonded joints under pure mode I loading," *Composites Science and Technology,* vol. 68, pp. 2224-2230, 2008.

[13] S. Ito, M. Hashimoto, B. Wadgaonkar, N. Svizero, R. M. Carvalho, C. Yiu*, et al.*, "Effects of resin hydrophilicity on water sorption and changes in modulus of elasticity," *Biomaterials,* vol. 26, pp. 6449-6459, 2005.

[14] A. G. Evans, J. W. Hutchinson, and Y. Wei, "Interface adhesion: Effects of plasticity and segregation," *Acta Materialia,* vol. 47, pp. 4093-4113, 1999.

[15] G.Z. Xiao and M. E. R. Shanahan, "Swelling of DGEBA/DDA epoxy resin during hygrothermal ageing," *Polymer,* vol. 39, pp. 3253-3260, 1997.

[16] E. P. O'Brien, "Durability of Adhesive Joints Subjected To Environmental Stress," Doctor of Philosophy, Virginia Polytechnic Institute and State University, Blacksburg, Virginia, 2003.

[17] Sugiman, "Combined Environmental and Fatigue Degradation of Adhesively Bonded Metal Structures," Doctor of Philosophy, Faculty of Engineering and Physical Sciences, University of Surrey, Guildford, 2012.

[18] W. K. Loh, A. D. Crocombe, M. M. A. Wahab, and I. A. Ashcroft, "Environmental degradation of the interfacial fracture energy in an adhesively bonded joint," *Engineering Fracture Mechanics,* vol. 69, pp. 2113-2128, 2002.

[19] Y. Zhang, R. D. Adams, and L. F. M. d. Silva, "Absorption and glass transition temperature of adhesives exposed to water and toluene," *International Journal of Adhesion and Adhesives,* vol. 50, pp. 85-92, 2014.
[20] J. Crank, *The Mathematics of Diffusion*: Oxford university press, 1975.
[21] A. Fick, "On Liquid Diffusion," *Journal of Membrane Science,* vol. 100, pp. 33-38, 1995.
[22] C.H. Shen and G. S. Springer, "Moisture Absorption and Desorption of Composite-Materials," *Journal of Composite Materials,* vol. 10, pp. 2-20, 1976.
[23] A.Q. Barbosa, L.F.M. da Silva, and A. Öchsner, "Hygrothermal aging of an adhesive reinforced with microparticles of cork," *Journal of Adhesion Science and Technology,* vol. 29, pp. 1714-1732, 2015.
[24] E.H. Immergut and H. F. Mark, "Principles of Plasticization," *Advances in Chemistry,* vol. 48, pp. 1-26, 1965.
[25] A. Ameli, "Hygrothermal Degradation of Toughened Adhesive Joints: The Characterization and Prediction of Fracture Properties," Doctor of Philosophy, Graduate Department of Mechanical and Industrial Engineering, University of Toronto, 2011.
[26] J.W. Wylde and J. K. Spelt, "Measurement of adhesive joint fracture properties as a function of environmental degradation," *Adhesion & Adhesives,* vol. 18, pp. 237-246, 1997.
[27] Y. C. Lin and X. Chen, "Moisture sorption-desorption-resorption characteristics and its effect on the mechanical behavior of the epoxy system," *Polymer,* vol. 46, pp. 11994-12003, 2005.
[28] J. Bardis and K. Kedward, "Effects of Surface Preparation on the Long-Term Durability of Adhesively Bonded Composite Joints," U.S. Department of Transportation Federal Aviation Administration, University of California Santa Barbara, 2004.
[29] M. Davis and D. Bond, "Principles and practices of adhesive bonded structural joints and repairs," *International Journal of Adhesion and Adhesives,* vol. 19, pp. 91-105, 1999.
[30] S. A. P. Limited, "SikaPower®-4720," Sika®, Ed. 8, 2014.
[31] M. Costa, G. Viana, C. Canto, L. da Silva, M. Banea, F. Chaves*, et al.*, "Effect of the size reduction on the bulk tensile and double cantilever beam specimens used in cohesive zone models," *Proceedings of the Institution of Mechanical Engineers, Part L: Journal of Materials: Design and Applications,* 2015, DOI 10.1177/1464420715610248.
[32] J.P.R. Monteiro, R.D.S.G. Campilho, E.A.S. Marques, and L. F. M. d. Silva, "Experimental estimation of the mechanical and fracture properties of a new epoxy adhesive," *Applied Adhesion Science,* vol. 3, pp. 1-17, 2015.
[33] D.F.O. Braga, L.M.C. de Sousa, V. Infante, L.F.M. da Silva, and P. M. G. P. Moreira, "Aluminium Friction-stir Weld-bonded Joints," *Journal of Adhesion,* vol. 92, pp. 665-678, 2016.
[34] D.F.O. Braga, L.F.M. da Silva, and P. M. G. P. Moreira, "Single Lap Joints Numerical Modelling and Comparison with Experimental Testing," *Journal of Engineering,* vol. 2, pp. 11-20, 2016.
[35] L.F.M. da Silva and M. J. C. Q. Lopes, "Joint strength optimization by the mixed-adhesive technique," *International Journal of Adhesion & Adhesives,* vol. 29, pp. 509-514, 2009.
[36] R. Kottner, R. Hynek, and T. Kroupa, "Identification of parameters of cohesive elements for modeling of adhesively bonded joints of epoxy composites," *Applied and Computational Mechanics,* vol. 7, pp. 137-144, 2013.
[37] L.F.M. da Silva, G.W. Critchlow, and M. A. V. Figueiredo, "Parametric Study of Adhesively Bonded Single Lap Joints by the Taguchi Method," *Journal of Adhesion Science and Technology,* vol. 22, pp. 1477-1494, 2012.
[38] L. Greenspan, "Humidity Fixed-Points of Binary Saturated Aqueous-Solutions," *Journal of Research of the National Bureau of Standards Section a-Physics and Chemistry,* vol. 81, pp. 89-96, 1977.

[39] A. Wexler and S. Hasegawa, "Relative Humidity-Temperature Relationships of Some Saturated Salt Solutions in the Temperature Range 0-Degree to 50-Degrees-C," *Journal of Research of the National Bureau of Standards,* vol. 53, pp. 19-26, 1954.

[40] G. Viana, M. Costa, M.D. Banea, and L. F. M. d. Silva, "Behavior of environmentally degraded epoxy adhesives as a function of temperature," *The Journal of Adhesion,* 2016.

[41] J. A. B. P. Neto, R. D. S. G. Campilho, and L. F. M. d. Silva, "Parametric study of adhesive joints with composites," *International Journal of Adhesion and Adhesives,* vol. 37, pp. 96-101, 2012.

[42] W.K. Loh, A.D. Crocombe, M.M.A. Wahab, and I. A. Ashcroft, "Modelling anomalous moisture uptake, swelling and thermal characteristics of a rubber toughened epoxy adhesive," *International Journal of Adhesion and Adhesives,* vol. 25, pp. 1-12, 2005.

[43] M. Costa, G. Viana, L.F.M. da Silva, and R. D. S. G. Campilho, "Effect of humidity on the mechanical properties of adhesively bonded aluminium joints," *Proceedings of the Institution of Mechanical Engineers, Part L: Journal of Materials: Design and Applications,* 2016, DOI: 10.1177/1464420716645263.